JYVÄSKYLÄ STUDIES IN COMPUTING
120

Tuomas Airaksinen

Numerical Methods for Acoustics and Noise Control

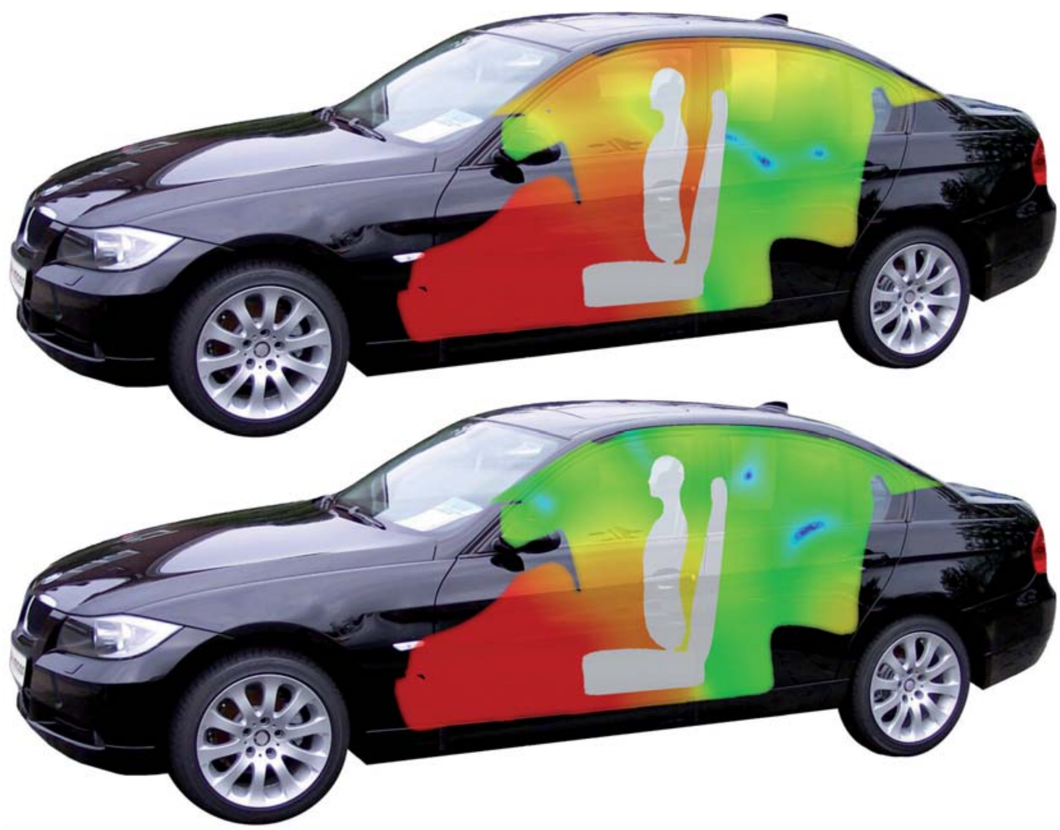

JYVÄSKYLÄN YLIOPISTO

ABSTRACT

Airaksinen, Tuomas
Numerical methods for acoustics and noise control
Jyväskylä: University of Jyväskylä, 2010, 58 p.(+included articles)
(Jyväskylä Studies in Computing
ISSN 1456-5390; 120)
ISBN 978-951-39-4031-7 (nid.), 978-951-39-4037-9 (PDF)
Finnish summary
Diss.

This dissertation considers numerical methods for wave propagation modelling and noise control. The first part of the dissertation discusses an efficient method for solving time-harmonic wave equations in acoustic (the Helmholtz equation) and elastic domains (the Navier equation). The solver is based on preconditioning a Krylov subspace method, such as GMRES, with approximations of damped variants of the corresponding wave equations. An algebraic multigrid method is used in approximating the inverse of damped operators. The method can be used in complex three-dimensional computational domains with varying material properties.

The second part of the dissertation considers noise control problems. Two different noise control problems are discussed in detail. First, a shape optimization of a duct system with respect to sound transmission loss is discussed. The sound transmission loss is maximized at multiple frequency ranges simultaneously, by adjusting the shape of a reactive muffler component. The noise reduction problem is formulated as a multiobjective optimization problem for the NSGA-II genetic algorithm. The discussed method provides an efficient approach to design muffler components. Second, a novel method is introduced for assessing the effectiveness of the optimal anti-noise for local sound control in a stochastic domain. A three-dimensional enclosed acoustic space, for example, a cabin with acoustic actuators in given locations, is modelled using the finite element method in the frequency domain. In a model problem, a significant noise reduction is demonstrated particularly at lower frequencies.

Keywords: acoustics, preconditioning, noise control, finite element method, optimization, stochastic domain, genetic algorithm, shape optimization, duct, reactive muffler

JYVÄSKYLÄ STUDIES IN COMPUTING 120

Tuomas Airaksinen

Numerical Methods for Acoustics and Noise Control

Esitetään Jyväskylän yliopiston informaatioteknologian tiedekunnan suostumuksella
julkisesti tarkastettavaksi yliopiston Agora-rakennuksen auditoriossa 2
lokakuun 9. päivänä 2010 kello 12.

Academic dissertation to be publicly discussed, by permission of
the Faculty of Information Technology of the University of Jyväskylä,
in the building Agora, Auditorium 2, on October 9, 2010 at 12 o'clock noon.

UNIVERSITY OF JYVÄSKYLÄ

JYVÄSKYLÄ 2010

Numerical Methods for Acoustics and Noise Control

JYVÄSKYLÄ STUDIES IN COMPUTING 120

Tuomas Airaksinen

Numerical Methods for Acoustics and Noise Control

UNIVERSITY OF JYVÄSKYLÄ

JYVÄSKYLÄ 2010

Editor
Timo Männikkö
Department of Mathematical Information Technology, University of Jyväskylä
Pekka Olsbo, Sini Rainivaara
Publishing Unit, University Library of Jyväskylä

URN:ISBN:978-951-39-4037-9
ISBN 978-951-39-4037-9 (PDF)

ISBN 978-951-39-4031-7 (nid.)
ISSN 1456-5390

Jyväskylä University Printing House, Jyväskylä 2010

Author Tuomas Airaksinen
tuomas.airaksinen@gmail.com
Department of Mathematical Information Technology,
University of Jyväskylä, Finland

Supervisors Dr. Jari Toivanen
Department of Mathematical Information Technology,
University of Jyväskylä, Finland

Dr. Erkki Heikkola
Numerola Ltd
Jyväskylä, Finland

Reviewers Prof. Oliver Ernst
Institut für Numerische Mathematik und Optimierung
Technische Universität Bergakademie
Freiberg, Germany

Dr. Radek Tezaur
Aeronautics and Astronautics
Stanford University, USA

Opponent Prof. Martin Berggren
Department of Computing Science
Umeå University, Sweden

ACKNOWLEDGMENTS

I would like to express very special thanks and praise to God for his undisputable guidance with respect to my studies and personal life and for the promise of eternal life (*John 6:47*). I also want to give heartful thanks to Dr. Jari Toivanen and Dr. Erkki Heikkola for their professional and devoted supervision through my Ph.D. project. Thanks to my workmate Jukka Räbinä for his good company – I will miss the lunch breaks and the pleasant atmosphere in our lab. Thanks to my parents, Harri and Eeva Airaksinen, for love and support. Finally, thanks to my friends for all the friendship, support, and prayers.

LIST OF FIGURES

LIST OF TABLES

CONTENTS

LIST OF INCLUDED ARTICLES

I Tuomas Airaksinen, Erkki Heikkola, Anssi Pennanen, Jari Toivanen. An algebraic multigrid based shifted-Laplacian preconditioner for the Helmholtz equation. *Journal of Computational Physics 226 (2007) 1196-1210*.

II Tuomas Airaksinen, Anssi Pennanen, Jari Toivanen. A damping preconditioner for time-harmonic wave equations in fluid and elastic material. *Journal of Computational Physics 228 (2009) 1466-1479*.

III Tuomas Airaksinen, Sanna Mönkölä. Comparison between shifted-Laplacian preconditioning and controllability method for computational acoustics. *Journal of Computational and Applied Mathematics 234 (2010) 1796-1802*.

IV Tuomas Airaksinen, Erkki Heikkola, Jari Toivanen. Active noise control in a stochastic domain based on a finite element model. *Reports of the Department of Mathematical Information Technology, Series B. Scientific Computing, B 1 / 2009*, Submitted to a journal.

V Tuomas Airaksinen, Erkki Heikkola. Multiobjective muffler shape optimization with hybrid acoustics modelling. *Reports of the Department of Mathematical Information Technology, Series B. Scientific Computing, B 6 / 2010*, Submitted to a journal.

The author set up and performed all of the numerical simulations for the study presented in article [I] and wrote the manuscript draft. The damped Helmholtz (shifted-Laplacian) preconditioner code for the Helmholtz equation was based on algebraic multigrid code contributed by Anssi Pennanen and Janne Martikainen. This code was further developed for the numerical experiments of the study by the author. In article [II], the author extended the idea of physical damping to elastic material. The author further designed and implemented related simulation code for the numerical experiments, based on Helmholtz code that was used in earlier study. The author planned and set up the numerical experiments and wrote the manuscript draft. In article [III], the author performed all the simulations related to the damped Helmholtz (shifted-Laplacian) preconditioner and wrote the related parts of the manuscript. In article [IV], the author was involved in planning of the method to investigate active noise control in stochastic domains, together with the co-authors of the article. The author wrote the related code, planned and set up the numerical experiments. The author also wrote the manuscript draft of the article. In article [V], the author was involved in planning the shape optimization method and implemented the code, together with the co-author of the article. The author planned and performed the numerical experiments and wrote the manuscript draft.

1 INTRODUCTION

Motivation for conducting research on sound-related phenomena can be found in everyday life. Indeed, noise is a significant inconvenience for everyone in today's society. It is encountered in city centers, factories, and various vehicles. Rotating parts such as wheels, engines, and cooler fans are typical noise sources. These devices need noise reduction in order to be safe and comfortable in use. Various noise control techniques for the reduction of noise levels are available.

Sound and vibration phenomena are also advantageous in many ways. They are exploited by many applications of modern technology. Particularly non-audible ultra- and infrasound are used in many applications. Echo sounding devices use infrasound, whereas ultrasound is used for various medical purposes such as ultrasound surgery, imaging, and tomography. Ultrasound is also used to catalyze certain chemical reactions, as well as for purification and disinfection purposes.

There are a number of different sound research methods and these are categorized in three main classes: experimental, analytical, and computational. Experimental techniques are commonly used in acoustical studies. These methods require special settings that are not always feasible due to technical or economic reasons. In some cases, it is possible to build an analytical acoustic model, but these are limited to rather simple problem types with respect to geometry, material, and boundary properties. Computational methods offer a novel approach to perform acoustical studies accurately and efficiently. All of these methods have their own advantages and complement each other. For example, computational models are often verified by analytical or experimental studies.

The field of computational acoustics is relatively new, as the computer technology allowing appropriate simulations has only existed for a few decades. During these decades, however, active research on numerical methods allowing efficient modelling for complicated problem types has been conducted. Recently, the technological development has made computational methods an affordable alternative to various acoustical studies. They are often very cost-effective, as prototypes and scale models are not needed. Computation also makes it possible to perform optimizations that typically require a large number of experiments.

The shape, topology, and material parameters can be optimized, for example, with respect to acoustic properties such as noise reduction.

The aims of this dissertation are to introduce an improved numerical method for acoustic and elastic wave propagation simulation and to propose advanced optimization methods for noise reduction. The dissertation comprises an introduction and five scientific articles. The introduction offers a review of the five articles included. The introduction is structured as follows: Chapter 1 indicates the motivation for the study and provides some introductory background information, as well as outlines the organization of the dissertation; Chapter 2 presents the physical and mathematical background to the acoustic problems addressed in the dissertation; Chapter 3 reviews both the numerical methods used in this study and some other major numerical methods used in studies of acoustics.

In Chapter 4, a preconditioning technique based on physical damping for time-harmonic acoustic and elastic wave equations is presented, summarizing articles [I, II, III]. An algebraic multigrid method is used to approximate the inverse of the discretized preconditioner. The technique was introduced for the two-dimensional Helmholtz problems in [I] and further generalized to three-dimensional problems and elastic problems in [II]. The results are compared to the MIC-based preconditioning and exact controllability method [21, III].

Chapter 5 reviews noteworthy sound or noise controlling methods and summarizes the studies carried out for the articles [IV, V]. Two different noise control methods are presented. Both methods involve optimization and acoustic simulations. The first method considers noise control in duct systems by optimizing the shape of a reactive muffler component, based on article [V]. The second method examines local noise control in a stochastic domain, based on article [IV].

Finally, Chapter 6 summarizes the results of the dissertation and offers some concluding remarks.

2 PHYSICS OF SOUND

As a physical quantity, sound is described as propagation of temporal density fluctuations, i.e. compressions and rarefactions of the medium. In fluids, these fluctuations are small pressure changes and in solid materials they are small displacements of material particles. The wave propagation problems addressed in this dissertation are described mathematically by linear wave equations. The sound modelling is considered in fluid (gas or liquid) and solid elastic material. A solid material is referred to as elastic if it reverts to its original shape after being deformed. Most metals are elastic with respect to small deformations.

In this chapter, the acoustic wave equation is derived. In many practical applications, sound is time-harmonic by nature. Moreover, time-dependent problems can be converted into time-harmonic problems through Fourier transformation. A time-harmonic assumption simplifies the mathematical formulation of wave propagation problems. The acoustic wave equation reduces to the Helmholtz equation, and, in elastic media, time-harmonic wave-propagation is governed by the Navier equation, correspondingly. In the later chapters, only time-harmonic problem types are considered.

Several books providing an introduction on acoustics and elasticity have been written; for example, [31, 35]. In the following section, the derivation of wave equation is based on [28].

2.1 Acoustic wave equation

A justified assumption for most fluids is that sound propagation (emergence and transmission) is an isentropic process, i.e. it is adiabatic and reversible. In an adiabatic process there is no thermal entry or loss, i.e. the amount of thermal energy is constant. Thus, it holds, that

$$p = -Bs, \tag{1}$$

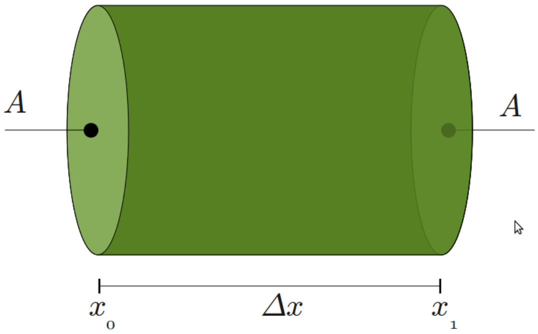

FIGURE 1 The one-dimensional fluid element.

where p is the pressure, $s = \Delta V / V$ is the condensation of the volume V and B is the bulk modulus determining the stiffness of the medium. The behavior of fluid with slow volume changes is analogous to the compression of a harmonic spring. The minus sign in Eq. (1) indicates that pressure increase leads to a decrease of volume and vice versa. In the one-dimensional case, the condensation depends on the displacement u as $s = du/dx$, so Eq. (1) for pressure reads

$$p = -B\frac{\partial u}{\partial x}. \tag{2}$$

To obtain the Euler equation, Newton's second law is applied to a small fluid interval Δx with ending points at x_0 and x_1 (see Figure 1). The compressive forces at the interval boundaries are at equilibrium with the volume force due to inertia:

$$-A\left(p\left(x_1\right) - p\left(x_0\right)\right) = \rho_0 A\left(x_1 - x_0\right)\frac{\partial v}{\partial t}, \tag{3}$$

where A is the area of the surface at the ends of the considered one-dimensional element, and v is the velocity of the fluid element and ρ_0 is the static, or time-averaged density of the material. When $\Delta x \to 0$, the Euler equation is obtained:

$$\frac{\partial p}{\partial x} = -\rho_0\frac{\partial v}{\partial t}. \tag{4}$$

To derive the wave equation, a spatial derivative is first taken on both sides of Eq. (4):

$$\frac{\partial^2 p}{\partial x^2} = -\frac{\partial}{\partial x}\left(\rho_0\frac{\partial v}{\partial t}\right). \tag{5}$$

It is assumed that the static density is constant, i.e. $\partial_x \rho_0 = 0$. Next, Eq. (2) is considered, i.e. $\partial_t v = u$ and $\partial_x u = -B^{-1}p$ are substituted in Eq. (5):

$$\frac{\partial^2 p}{\partial x^2} = \frac{\rho_0}{B}\frac{\partial^2 p}{\partial t^2}. \tag{6}$$

Now, it is enough to note that the speed of sound $c = \sqrt{B/\rho_0}$ can be substituted, and the wave equation is obtained:

$$\frac{\partial^2 p}{\partial x^2} - \frac{1}{c^2}\frac{\partial^2 p}{\partial t^2} = 0. \tag{7}$$

This generalizes to a three-dimensional wave equation, which reads

$$\boldsymbol{\nabla}^2 p - \frac{1}{c^2}\frac{\partial^2 p}{\partial t^2} = 0. \tag{8}$$

Time-harmonic acoustic wave equation (the Helmholtz equation)

By substituting a time-harmonic pressure of the form

$$p(\mathbf{x}, t) = \hat{p}(\mathbf{x})\, e^{-i\omega t} \tag{9}$$

in Eq. (8), with an angular frequency ω and imaginary unit $i = \sqrt{-1}$, the Helmholtz equation is obtained:

$$-\boldsymbol{\nabla}^2 \hat{p} - k^2 \hat{p} = 0, \tag{10}$$

where $k(\mathbf{x}) = \omega / c(\mathbf{x})$ is the wave number. In an inhomogeneous medium, the wave number k varies depending on location, as the sound speed c varies.

Impedance boundary condition

Absorbing and partially absorbing boundaries of the fluid domain are approximated by an impedance boundary condition that is modelled by

$$\mathbf{n} \cdot \boldsymbol{\nabla} \hat{p} = i\gamma k \hat{p}, \tag{11}$$

where $\mathbf{n}(\mathbf{x})$ is the outer unit normal vector [27]. Choosing the absorbency coefficient $\gamma = 0$ leads to the Neumann boundary condition that implies a perfect reflecting sound-hard boundary, and $\gamma = 1$ gives a low-order absorbing boundary condition.

Acoustic wave propagation in ducts

In uniform ducts, the solution to the Helmholtz equation Eq. (10) can be obtained by modal analysis [45]. In certain special cases, such as circular or rectangular ducts, the analytical form of the solution can be derived; whereas in the general shaped duct, eigenfunctions have to be solved numerically. The expansion of the acoustic pressure in the duct is represented in cylindrical coordinates as a sum over the eigenmodes

TABLE 1 First roots of Bessel derivative function, $J'_{m_j}(b_j) = 0$.

j	1	2	3	4	5
m_j	0	1	2	0	3
b_j	0.0	1.84	3.05	3.83	4.20

$$p(r,\theta,z) = \sum_{j=0}^{\infty} A_j \Phi_j(r,\theta) e^{-i\lambda_j z} + \sum_{j=0}^{\infty} F_j \Phi_j(r,\theta) e^{i\lambda_j z} \quad (12)$$

where $\Phi_j(r,\theta)$ are the transverse duct eigenfunctions corresponding to the cross-section of the pipe; A_j and F_j are the modal amplitudes corresponding to eigenfunctions Φ_j; and λ_j are axial wavenumbers along the z-axis.

In the circular duct, eigenfunctions $\Phi_j(r,\theta)$ are represented by modes

$$\Phi_j(r,\theta) = J_{m_j}(k_{rj} r) e^{i m_j \theta}, \quad (13)$$

where $J_{m_j}(x)$ is order m_j Bessel function of the first kind and k_{rj} is the radial wavenumber. The radial wavenumber k_{rj} is obtained by considering a sound-hard wall boundary condition $\mathbf{n} \cdot \boldsymbol{\nabla} p = 0$, which here implies that at $r = a$, where a is the radius of the duct wall,

$$J'_{m_j}(k_{rj} a) = 0. \quad (14)$$

Axial wavenumber k_{zj} is evaluated from the effective wavenumber k and the radial wavenumber k_{rj} by

$$k_{zj} = \sqrt{k^2 - k_{rj}^2}. \quad (15)$$

The axial wave propagation in Eq. (12) is determined by term $e^{ik_{zj}z}$, which implies that the imaginary axial wavenumber k_{zj} leads to exponential decaying of the wave mode. Thus, the evanescent modes with $k_{rj} > k$ can be neglected. The modes are denoted by an index j, which starts from zero and is ordered in accordance with the radial wavenumbers k_{rj}. The radial wavenumbers can be calculated from Bessel derivative roots $k_{rj} = b_j / a$ according to Eq. (14) (see Table 1), where b_j is the root of Bessel derivate of order m_j and a is the radius of the duct.

Reciprocity principle

The acoustical reciprocity principle is explained in the following: the sound emitted by the source at the location **a**, measured at the location **b**, has the same pressure amplitude as the sound emitted from the source at the location **b**, measured at the location **a**. In other words, the principle says that the observation stays the same when the locations of sound source and observer are exchanged. For more details about the priciple and its applications, see [16, 17, 31].

2.2 Time-harmonic elastic wave equation (Navier equation)

The theory of elasticity is covered in detail in [35]. Here, only the governing equation for time-harmonic propagation in linear elastic media is given.

For time-harmonic displacements $\mathbf{u}(\mathbf{x}, t) = e^{-i\omega t}\hat{\mathbf{u}}(\mathbf{x})$ in a domain consisting of elastic materials, the scattering of time-harmonic waves is described by the Navier equation

$$-\omega^2 \rho \hat{\mathbf{u}} - \nabla \cdot \sigma(\hat{\mathbf{u}}) = \mathbf{f}, \tag{16}$$

where σ is the stress tensor, $\mathbf{f}$ is a force term that is non-zero at sound sources, and ρ is the density of the material. Hooke's law gives a relation between displacements, and stress and strain forces, thus describing strain tensor ϵ and stress tensor σ:

$$\epsilon(\mathbf{u}) = \frac{1}{2}\left(\nabla \mathbf{u} + (\nabla \mathbf{u})^T\right), \quad \sigma(\mathbf{u}) = \lambda(\nabla \cdot \mathbf{u}) + 2\mu\epsilon(\mathbf{u}). \tag{17}$$

Here Lamé parameters λ and μ are defined as follows:

$$\lambda(\mathbf{x}) = \frac{E}{2(1+\nu)}, \quad \mu(\mathbf{x}) = \frac{E\nu}{(1+\nu)(1-2\nu)}. \tag{18}$$

These depend on the Young modulus $E(\mathbf{x})$ and Poisson's ratio $\nu(\mathbf{x})$ that characterize the elastic behavior of the material. The speeds of pressure wave, c_p, and shear wave, c_s, are to be expressed as functions of Lamé parameters:

$$c_p = \sqrt{\frac{\lambda + 2\mu}{\rho}}, \quad c_s = \sqrt{\frac{\mu}{\rho}}. \tag{19}$$

Impedance boundary condition

Absorbing and partially absorbing boundaries are approximated by an impedance boundary condition, which is modelled by the equation

$$i\gamma\omega\rho_s \mathbf{B}\hat{\mathbf{u}} + \sigma(\hat{\mathbf{u}})\,\mathbf{n} = 0, \tag{20}$$

where γ is the absorbency coefficient, and $\mathbf{B}$ is a 3×3 matrix for three-dimensional problems [11]. Choosing the absorbency coefficient $\gamma = 0$ leads to a natural boundary condition and $\gamma = 1$ gives an absorbing boundary condition. In component form, $\mathbf{B}$ has the expression

$$\mathbf{B}_{ij} = c_p n_i n_j + c_s t_i t_j + c_s s_i s_j \tag{21}$$

for three-dimensional problems, where c_p and c_s are the speeds of pressure and shear waves given by Eq. (19), $\mathbf{n}$ is the unit normal vector pointing out of the elastic domain, and $\mathbf{t}$ and $\mathbf{s}$ are tangential vectors on the boundary.

3 NUMERICAL METHODS FOR ACOUSTIC MODELLING

During recent decades, numerical methods for acoustic and elastic wave propagation problems have been actively researched. It has proven challenging, both mathematically and computationally, to develop robust, efficient, and universal methods for solving these problems. Due to the wide range of applications that exist in different disciplines, interest and motivation for good numerical methods are emphasized. Several recently studied numerical methods for acoustics are presented in detail in [40]. This chapter reviews briefly the numerical methods that are used in this dissertation and some others that are commonly used in acoustic modelling.

3.1 Discretization methods for PDEs

Finite element method

The finite element method (FEM) is a general framework for solving numerically integral and differential equations, particularly partial differential equations (PDEs). It has been successfully applied to structural mechanics, fluid dynamics, thermal transfer problems, quantum mechanics, electromagnetics, acoustics, and various combinations of these, to name a few. Finite element analysis, particularly in the context of acoustic scattering problems is addressed in [27]. The finite element approximation of the PDE solution is obtained either by eliminating the differential equation completely (steady state problems) or by turning the PDE into a system of ordinary differential equations that are integrated numerically (time-dependent problems). The procedure of Galerkin FEM is described briefly in the following.

A mesh consisting of small, non-overlapping elements is constructed for computation domain Ω. Triangles or quadrangles are usually used in two-dimensional problems as well as in three-dimensional domain surfaces, and tetrahedral

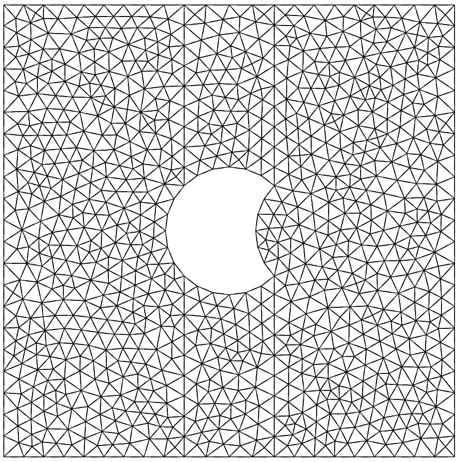

(a)

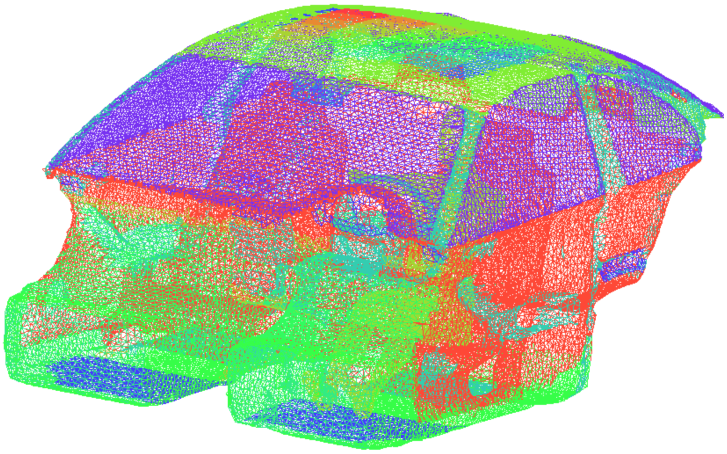

(b)

FIGURE 2 Finite element mesh examples.

or hexahedral elements are used to fill three-dimensional volumes. In Figure 2, two finite element mesh examples are shown. Curvilinear polygons can also be used to improve accuracy on curved boundaries and it is possible to use several different types of elements simultaneously in the same problem. The element sizes are adapted to the requirements of the problem and may vary over the domain. FEM is particularly efficient in regard to complicated domains in which the desired precision varies over the entire domain.

The problem is formulated in the weak form by multiplying the governing equation by a test function and integrating it over the computation domain. Higher order derivatives in resulting integral equation are integrated by parts. The examined quantity, such as acoustic pressure for example, is approximated by

$$p(x) = \sum_{j=1}^{n} N_j(x)\, p_j = [N_1(x), \ldots, N_n(x)] \begin{bmatrix} p_1 \\ \vdots \\ p_n \end{bmatrix} = \mathbf{N}(x)^T \mathbf{p}, \tag{22}$$

where $N_j(x)$ is the basis function of j^{th} node in the defined mesh, p_j is the nodal value of the examined quantity at node j, and n is the number of nodes in the computation domain. The Galerkin method proposes that $N_j(x)$ are used as test functions. There are many choices of basis functions, but piecewise linear or polynomial functions are typically used. The choice of piecewise basis functions has the advantage that the pressure on each individual node only depends on a few neighbouring nodes. This leads to a sparse linear system of equations, which allows the solution of large problems.

The resulting system of linear equations from the discretization of the Helmholtz or Navier equation is non-Hermitian and indefinite. For mid-frequency and high-frequency problems, the matrix equation can be extremely large. Particularly the finite element phase shift error (often referred to as the pollution er-

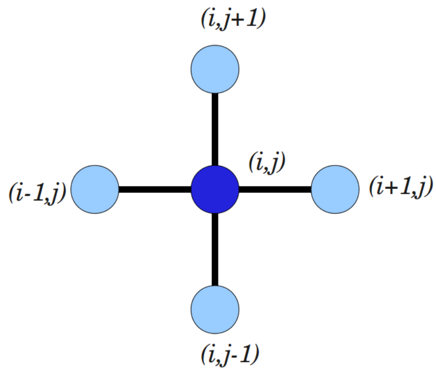

FIGURE 3 Five-point stencil.

ror) necessitates finer discretizations for high-frequency problems [27] and thus increases memory and computational requirements. Many three-dimensional problems are too large to be solved by direct methods with an affordable computing effort. Hence, it is necessary to use iterative methods such as the GMRES method [48] or the Bi-CGSTAB method [56]. However, these methods require a good preconditioner in order to converge in a reasonable time.

Finite difference method

The finite difference method (FDM) approximates PDEs by replacing the derivative expressions with approximating difference quotients [44]. Discretization of the problem's domain is usually done by dividing the subdomain into a uniform grid. In two- and three-dimensional domains, a stencil notation is useful in the discretization of partial differential equations. For example, if a square grid is used in two dimensions, the five-point stencil of a point is made up of the point itself and four neighboring nodes (see Figure 3). The five-point stencil for the two-dimensional Helmholtz operator $Ap = -\partial_x^2 p - \partial_y^2 p - k^2 p$ is given by the following notation:

$$A = \frac{1}{h^2}\begin{bmatrix} & -1 & \\ -1 & 4-(kh)^2 & -1 \\ & -1 & \end{bmatrix}. \tag{23}$$

The system of linear equations is assembled simply from the linear equations that are constructed for each computation node in a discretization grid. The coefficient matrix $\mathbf{A}$ is a banded, sparse matrix.

The finite difference method is very popular due to its simplicity and straightforward implementation. However, it is limited to staircase approximations of the domain, which makes it inefficient for complex problems.

3.2 Solution methods for PDEs

Preconditioned iterations

The convergence of Krylov subspace methods for the discretized Helmholtz or Navier equation is very slow for medium- and large-scale scattering problems, due to the ill conditioning of coefficient matrix $\mathbf{A}$. The speed of the convergence can be significantly improved by choosing a suitable preconditioner $\mathbf{B}$. This leads to the right preconditioned system

$$\mathbf{A}\mathbf{B}^{-1}\tilde{\mathbf{u}} = \mathbf{f}. \tag{24}$$

Once $\tilde{\mathbf{u}}$ is solved from this system, the solution $\mathbf{u}$ is obtained as $\mathbf{u} = \mathbf{B}^{-1}\tilde{\mathbf{u}}$. The goal is to find a preconditioner $\mathbf{B}$ such that the matrix $\mathbf{A}\mathbf{B}^{-1}$ is well conditioned and that vectors can be multiplied by $\mathbf{B}^{-1}$, i.e. solve systems with $\mathbf{B}$ with little computational effort. These properties would lead to a fast convergence of the iterative method and to a small overall computational cost. Several preconditioners and iterative solution techniques have been proposed for the discrete Helmholtz and Navier equations.

So-called natural preconditioning techniques are applicable for many acoustic problems, including time-harmonic wave equations [55]. An example of this approach is the class of preconditioners based on damped operators discussed in Chapter 4. A shifted-Laplacian preconditioner with a complex shift, which is here referred to as the damped Helmholtz preconditioner, was first reported in [13] for the Helmholtz equation. This was a development over the shifted-Laplacian preconditioner with a real shift, previously described in [34].

The damped Helmholtz preconditioner with geometric multigrid was studied in [12]. This approach was extended in [I] to general shaped two-dimensional domains using finite element discretizations. The algebraic multigrid method (AMG) was applied instead of the geometric multigrid in order to approximate the inversion of the damped Helmholtz operator. In [II], this method was further extended to three-dimensional problems and also time-harmonic wave propagation problems in elastic media, i.e. the Navier equation. The technique and some results and comparison are discussed particularly in Chapter 4, based on articles [I, II, III].

An incomplete factorization preconditioner has been considered in [39]. The preconditioning is based on adding small perturbations to the diagonal entries of the real part of the preconditioner matrix, assembled from the discretization of the Helmholtz equation. The perturbed preconditioner matrix equation is then solved with standard incomplete factorization methods such as incomplete LU or incomplete Cholesky (see e.g., [47]). Significant savings of GMRES iterations are reported. In Section 4.2, this technique is compared to the damped Helmholtz and Navier preconditioners.

Multigrid methods

Multigrid methods [54] are techniques for solving partial differential equations by using a hierarchy of discretizations. Accelerated convergence of an iterative method is achieved by a global correction obtained by solving a set of coarse problems. The coarse problems are formed either geometrically (geometric multigrid method, GMG) or algebraically (algebraic multigrid method, AMG).

The multigrid method proceeds as follows. The residual of the matrix equation is first restricted to coarse levels. A correction is obtained by approximately solving the error equation $\mathbf{Ae} = \mathbf{r}$ at a coarse level, where $\mathbf{A}$ is the matrix at the coarse level, $\mathbf{e}$ is the error vector, and $\mathbf{r}$ is the current residual. This is done in a recursive manner at several coarse levels. Corrections from different coarse levels reduce the residual at different frequency ranges: particularly low frequency error components are reduced at the coarsest levels. This makes the method efficient, as low frequency error components deteriorate the convergence speed of iterative solvers. The error equation is solved by a solver that reduces high-frequency error components effectively, and is thus referred to as a smoother. For example, the Jacobi or Gauss-Seidel methods [47] are commonly used as smoothers.

The multigrid method alone has been successfully applied to various types of problems, but has proven to be ineffective for wave propagation problems. In [9], it has been used for the Helmholtz problems as a preconditioner to the outer GMRES iteration. There, GMRES has been used as a smoother on the coarsest grids. The resulting method is robust and significantly more effective than the standard multigrid method alone.

Domain imbedding / Fictitious domain method

Domain imbedding/fictitious domain methods are special techniques for constructing efficient preconditioners for elliptic equations. These methods are based on imbedding the original domain into another one with a simple geometrical form, which permits the application of fast direct solvers. An algebraic fictitious domain method is proposed as a preconditioning method for the Helmholtz equation in [22, 26]. Due to the structure of the preconditioner, GMRES iterations are reduced in a low-dimensional subspace. The method is scalable and offers fast convergence, but it is more difficult to implement for complicated problems. The finite element capacitance matrix method [14] is an approach that is similar to domain imbedding / fictitious domain methods.

Domain decomposition methods

The idea of domain decomposition methods [53] is to split the partial differential equation into coupled problems on smaller subdomains such that they form a partition of the original domain and then iterate the interactions between adjacent subdomains. A coarse problem with relatively few unknowns per subdomain is used to synchronize the solution globally. The subdomain problems are independent, which makes the method suitable for parallel computing. Domain decomposition methods have been proposed for the Helmholtz problems in [18, 29], and for elastic problems in [5, 15], for example.

Exact controllability method

Exact controllability [4, 25] is an approach that is suitable for solving the Helmholtz equation via the time-dependent wave equation. The basic idea is to find a time-harmonic solution to the associated time-dependent wave equations by using a controllability method. The solution is obtained by minimizing the difference between initial conditions and the corresponding variables after time period $T = 2\pi/\omega$. By proceeding in this way, the problem of time-harmonic wave scattering is then cast as a least-squares problem

$$\min_{e_0, e_1} \left(\frac{1}{2} \int_\Omega \left| \frac{\partial p\left(T\right)}{\partial t} - e_1 \right|^2 dx + \frac{1}{2} \int_\Omega \left| \nabla \left(p\left(T\right) - e_0 \right) \right|^2 dx \right), \tag{25}$$

where the initial conditions are contained in a vector $(e_0, e_1)^T = (p(0), \partial_t p(0))^T$, and $p(t) = \mathrm{Re}(e^{-ikt}\hat{p})$ satisfies the time-dependent equations associated with the system. The least-squares problem can be solved by a conjugate gradient method. The method leads to preconditioned conjugate gradient iterations for the initial data.

In article [III], the exact controllability approach was compared to the damped preconditioner method described in Chapter 4. The damped preconditioner method was revealed to be considerably faster when the performance was compared with respect to CPU time. Some results are reviewed in Section 4.2.

3.3 Other acoustic simulation methods

Boundary element method

The boundary element method [33] is a robust and commonly used method in computational acoustics, and it is particularly popular in acoustic scattering because it produces smaller matrices than FEM or FDM.

Instead of solving the governing PDE in entire volume, the boundary element method attempts to use the given boundary conditions in order to fit the boundary values into the integral equation. The radiation problem is arranged into the Helmholtz-Kirchhoff integral equation

$$p\left(r\right) = \int_{\partial\Omega} \left(g\left(r|r_0\right) \mathbf{n} \cdot \boldsymbol{\nabla} p\left(r_0\right) - p\left(r_0\right) \mathbf{n} \cdot \boldsymbol{\nabla} g\left(r|r_0\right) \right) dx, \tag{26}$$

where

$$g\left(r|r_0\right) = e^{-\mathbf{i}k|r-r_0|}/4\pi\left|r-r_0\right| \tag{27}$$

is Green's function and $\partial\Omega$ is the boundary surface of the domain. The problem boundary is then discretized into surface elements; the problem can also be seen as a finite element discretization of the boundary integral equation Eq. (26). The Green function Eq. (27) fulfills the far-field radiation condition (Sommerfeld condition) of vanishing sound pressure when $r \to \infty$. In the post-processing stage, the integral equation can be used again to numerically calculate the solution in any interior point of the solution domain.

BEM is often computationally more efficient than FEM/FDM for problems that have a small surface-to-volume ratio. Therefore, BEM is often used for acoustic scattering problems. One of the benefits is that the number of degrees of freedom in BEM is relatively small due to the integration only occurring over the boundary. In turn, the resulting matrix of the problem is full, i.e. all nodes are connected to each other. Thus, the memory consumption and CPU time used for the inversion tends to grow in accordance with the square of the problem size, whereas the FEM/FDM typically only has corresponding linear growth. A considerable restriction to the boundary element method is the fact that it can only be used on problems that have homogeneous media.

Statistical energy analysis

Statistical energy analysis (SEA) is an acoustic simulation approach that is completely different from the other methods reviewed in this section. It is still worth mentioning here, as it provides an alternative for many large, high-frequency acoustic problems that would be too difficult to solve by current finite element methods.

The SEA method aims at predicting vibration transmission in a system that consists of coupled acoustic cavities and structures. The vibrational behavior in a system is described in terms of energy. A problem is solved with SEA by partitioning a system into regions in which the energy is equally shared among the vibrational modes.

SEA was originally introduced in the 1960s by Lyon and Maidanik [38, 37]. It has become particularly popular in the aerospace and automotive industries. A technique for coupling SEA with FEM or BEM has subsequently been developed in [49].

3.4 Duct acoustics modelling

Sound propagation in waveguides is a fundamentally interesting topic. Ventilation ducts are an example of a waveguide in which noise reduction is of a special interest. Often, the acoustic influence of a non-uniform obstruction is essential in

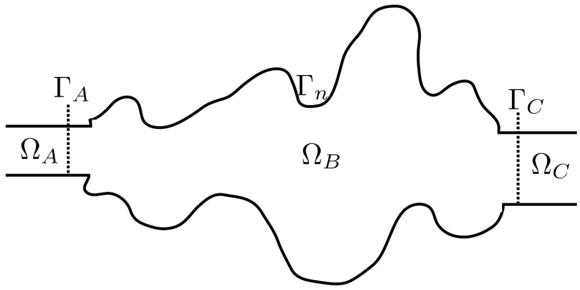

FIGURE 4 The cross-cut illustration of a duct system in a general case: inlet pipe Ω_A, muffler component of arbitrary shape Ω_B and outlet pipe Ω_C.

an otherwise uniform duct.

Duct acoustics can be modelled by several different means. There is an introduction to one dimensional duct acoustic modelling in [45]. The four-pole transfer matrix method, based on plane wave theory, offers an approximative way to make a one-dimensional model of muffler acoustics. This approach has been used for transmission loss optimization in the duct system [61]. However, the method is limited to simple geometries and boundary conditions. In [42], a mapped infinite partition of unity method is presented for axisymmetrical problems, which is applicable for duct acoustic problems.

The hybrid numerical method of [32] provides realistic modelling of acoustics in a muffler component, which is located between the uniform inlet and outlet ducts. In the uniform parts, an acoustic solution can be obtained by modal analysis, in which individual propagating modes are solved numerically, or, in special cases, analytically. The finite element method is used to solve the Helmholtz equation in the non-uniform muffler part of the ductwork. Mode matching [1] is used to couple the different solutions in the muffler and inlet/outlet ducts. The generality of the finite element method is thus provided to the acoustics simulation and complicated shapes and configurations can be treated accurately.

Hybrid numerical method

In the following, the hybrid numerical method of [32] is presented. The solution of the Helmholtz equation (Eq. (10) on page 13) in the muffler component domain Ω_B (see Figure 4) is obtained by using the finite element method. In duct domains Ω_A and Ω_C, the Helmholtz solution can be obtained by modal analysis. In certain special cases such as in a circular or rectangular duct, the analytical form of the solution can be derived; whereas in a general shaped duct, eigenfunctions have to be solved numerically. For example, in circular ducts, the solution of the Helmholtz equation can be represented in terms of Bessel functions, see Section 2.1. The acoustic pressure amplitudes in duct domains Ω_A and Ω_C are represented in cylindrical coordinates as expansions over the eigenmodes:

$$\begin{aligned}\hat{p}_A(r,\theta,z) &= \sum_{j=0}^{m_A} A_j \Phi_j(r,\theta) e^{-i\lambda_j z} + \sum_{j=0}^{m_A} F_j \Phi_j(r,\theta) e^{i\lambda_j z} \qquad \text{and} \\ \hat{p}_C(r,\theta,z) &= \sum_{j=0}^{m_C} B_j \Psi_j(r,\theta) e^{-i\gamma_j z} + \sum_{j=0}^{m_C} C_j \Psi_j(r,\theta) e^{i\gamma_j z},\end{aligned} \tag{28}$$

where hat symbols are used to denote the pressure amplitude of a time-harmonic wave (see Eq. (9) on page 13); $\Phi_j(r,\theta)$ and $\Psi_j(r,\theta)$ are transverse duct eigenfunctions corresponding to the cross-section of the pipe; A_j, F_j, B_j and C_j are the modal amplitudes corresponding to eigenfunctions Ψ_j, Φ_j; and λ_j, γ_j are axial wavenumbers along the z-axis. As the evanescent modes can be truncated, the sums in Eq. (28) only have a finite number of propagating modes, denoted by m_A, m_C. Coordinate systems in uniform ducts are chosen in such a way that the z-coordinate gives the axial direction of the duct with a positive direction away from the non-uniform domain Ω_B. The origin of the coordinate system in domain Ω_A is located on the interface Γ_A, and the origin of Ω_C is located on Γ_C.

Coefficients F_j determine the incoming sound from the inlet pipe. Modal amplitude coefficients A_j correspond to the sound that is reflected back from the muffler, B_j correspond to the sound propagating to the outlet pipe, and C_j correspond to the sound that is reflected back from the outlet pipe. By setting $C_j = 0$ for all j, a perfectly non-reflecting boundary is imposed on Γ_C.

The modal representations in Ω_A and Ω_C are coupled to the finite element representation in Ω_B by mode matching. The weak formulation of the Helmholtz equation (Eq. (10) on page 13) is the following: find $\hat{p}_B \in H^1(\Omega_B)$ such that

$$\int_{\Omega_B} \frac{1}{\rho} \left(\nabla \hat{p}_B \cdot \nabla \hat{q} - k^2 \hat{p}_B \hat{q} \right) dx - \int_{\partial\Omega_B} \frac{1}{\rho} \mathbf{n} \cdot \nabla \hat{p}_B \hat{q} \, dx = 0 \tag{29}$$

for any $\hat{q} \in H^1(\Omega_B)$, $\mathbf{n}$ is outward normal vector. Solutions $\hat{p}_A$ and $\hat{p}_C$ are coupled to $\hat{p}_B$ by the boundary conditions:

$$\mathbf{n} \cdot \nabla \hat{p}_B = \mathbf{n} \cdot \nabla \hat{p}_A \qquad \text{on } \Gamma_A, \tag{30}$$
$$\mathbf{n} \cdot \nabla \hat{p}_B = \mathbf{n} \cdot \nabla \hat{p}_C \qquad \text{on } \Gamma_C, \tag{31}$$
$$\hat{p}_B = \hat{p}_A \qquad \text{on } \Gamma_A, \tag{32}$$
$$\hat{p}_B = \hat{p}_C \qquad \text{on } \Gamma_C. \tag{33}$$

The first two conditions Eqs. (30) and (31) and the Neumann condition $\mathbf{n} \cdot \nabla p = 0$ on Γ_n can be incorporated in the weak form Eq. (44), leading to the equation

$$\int_{\Omega_B} \frac{1}{\rho} \left(\nabla \hat{p}_B \cdot \nabla \hat{q} - k^2 \hat{p}_B \hat{q} \right) dx - \int_{\Gamma_A} \frac{1}{\rho} \mathbf{n} \cdot \nabla \hat{p}_A \hat{q} \, dx - \int_{\Gamma_C} \frac{1}{\rho} \mathbf{n} \cdot \nabla \hat{p}_C \hat{q} \, dx = 0. \tag{34}$$

In mode matching, the two other conditions Eqs. (32) and (33) are imposed in weak forms: find $\hat{p}_A \in Z_A$, $\hat{p}_B \in H^1(\Omega_B)$ and $\hat{p}_C \in Z_C$ such that

$$\begin{aligned} \int_{\Gamma_A} (\hat{p}_B - \hat{p}_A)\,\bar{\Phi}_i dx &= 0 \text{ and} \\ \int_{\Gamma_C} (\hat{p}_B - \hat{p}_C)\,\bar{\Psi}_i dx &= 0 \end{aligned} \tag{35}$$

for any $\bar{\Phi}_i \in Z_A$ and $\bar{\Psi}_i \in Z_C$, where test function spaces are defined as $Z_A = \text{span}_{j=0,\dots,m_A}\{\Phi_j(r,\theta)\}$ and $Z_C = \text{span}_{j=0,\dots,m_C}\{\Psi_j(r,\theta)\}$. In summary, the hybrid formulation of the acoustic problem in the waveguide is given by the Eqs. (34) and (35).

Finite element discretization proceeds by approximating the acoustic pressure amplitude in Ω_B by Eq. (22), which is replaced in Eq. (34) to form a matrix equation

$$\int_{\Omega_B} \frac{1}{\rho}\left(\boldsymbol{\nabla}\mathbf{N}\cdot\boldsymbol{\nabla}\mathbf{N}^T - k^2\mathbf{N}\mathbf{N}^T\right) dx\,\hat{\mathbf{p}} - \int_{\Gamma_A}\frac{1}{\rho}\mathbf{N}\,\mathbf{n}\cdot\boldsymbol{\nabla}\hat{p}_A\,dx - \int_{\Gamma_C}\frac{1}{\rho}\mathbf{N}\,\mathbf{n}\cdot\boldsymbol{\nabla}\hat{p}_C\,dx = 0. \tag{36}$$

The modal representations of the solutions $\hat{p}_A$ and $\hat{p}_C$ in Eq. (12) are replaced in Eq. (36), which then is written in component form

$$\begin{aligned} \sum_{j=0}^{n_A}\int_{\Omega_B}\frac{1}{\rho}\left(\boldsymbol{\nabla}N_i\cdot\boldsymbol{\nabla}N_j - k^2N_iN_j\right)dx\,\hat{p}_j + i\sum_{j=0}^{m_A}\lambda_j\int_{\Gamma_A}\frac{1}{\rho}N_i\Phi_j\,dx\,A_j \\ -i\sum_{j=0}^{m_A}\lambda_j\int_{\Gamma_A}\frac{1}{\rho}N_i\Phi_j\,dx\,F_j + i\sum_{j=0}^{m_C}\gamma_j\int_{\Gamma_C}\frac{1}{\rho}N_i\Psi_j\,dx\,B_j = 0. \end{aligned} \tag{37}$$

By using matrix notations

$$\begin{aligned} \hat{H}_{ij} &= i\lambda_j\int_{\Gamma_A}\tfrac{1}{\rho}N_i\Phi_j\,dx, & \hat{K}_{ij} &= i\gamma_j\int_{\Gamma_C}\tfrac{1}{\rho}N_i\Psi_j\,dx, \\ \tilde{f}_i &= i\sum_{j=0}^{m_A}\lambda_j\int_{\Gamma_A}\tfrac{1}{\rho}N_i\Phi_j\,dx\,F_j, & G_{ij} &= \int_{\Omega_B}\tfrac{1}{\rho}\left(\boldsymbol{\nabla}N_i\cdot\boldsymbol{\nabla}N_j - k^2N_iN_j\right)dx, \end{aligned} \tag{38}$$

Eq. (37) can be presented compactly in matrix form

$$\hat{\mathbf{H}}\mathbf{a} + \mathbf{G}\hat{\mathbf{p}} + \hat{\mathbf{K}}\mathbf{b} = \tilde{\mathbf{f}}, \tag{39}$$

where $\mathbf{a}$ contains m_A complex modal amplitudes of interface Γ_A, $\mathbf{b}$ contains m_B complex modal amplitudes of interface Γ_B. Eqs. (12) and (22) are next replaced in

Eq. (35), which is written in component form

$$\begin{aligned}\sum_{j=0}^{n}\int_{\Gamma_A}\bar{\Phi}_i N_j\,dx\,\hat{p}_j &= \sum_{j=0}^{m_A}\int_{\Gamma_A}\Phi_j\bar{\Phi}_i\,dx\,A_j+\sum_{j=0}^{m_A}\int_{\Gamma_A}\Phi_j\bar{\Phi}_i\,dx\,F_j,\\ \sum_{j=0}^{n}\int_{\Gamma_B}\bar{\Psi}_i N_j\,dx\,\hat{p}_j &= \sum_{j=0}^{m_C}\int_{\Gamma_A}\Psi_j\bar{\Psi}_i\,dx\,B_j.\end{aligned} \tag{40}$$

By using matrix notations

$$\begin{aligned} H_{ij} &= \textstyle\int_{\Gamma_A}\Phi_j\bar{\Phi}_i\,dx, & K_{ij} &= \textstyle\int_{\Gamma_C}\Psi_j\bar{\Psi}_i\,dx,\\ \tilde{H}_{ij} &= -\textstyle\int_{\Gamma_A}\bar{\Phi}_i N_j\,dx, & \tilde{K}_{ij} &= -\textstyle\int_{\Gamma_C}\bar{\Psi}_i N_j\,dx,\\ f_i &= -\textstyle\sum_{j=0}^{m_A}\int_{\Gamma_A}\Phi_j\bar{\Phi}_i\,dx\,F_i, \end{aligned} \tag{41}$$

Eq. (40) can be presented in compact matrix form

$$\begin{aligned}\mathbf{Ha}+\tilde{\mathbf{H}}\hat{\mathbf{p}} &= \mathbf{f}\\ \mathbf{Kb}+\tilde{\mathbf{K}}\hat{\mathbf{p}} &= \mathbf{0}.\end{aligned} \tag{42}$$

The Eqs. (39) and (42) can now be written as a single block matrix equation

$$\begin{bmatrix}\mathbf{H} & \tilde{\mathbf{H}} & 0\\ \hat{\mathbf{H}} & \mathbf{G} & \hat{\mathbf{K}}\\ 0 & \tilde{\mathbf{K}} & \mathbf{K}\end{bmatrix}\begin{bmatrix}\mathbf{a}\\ \hat{\mathbf{p}}\\ \mathbf{b}\end{bmatrix}=\begin{bmatrix}\mathbf{f}\\ \tilde{\mathbf{f}}\\ 0\end{bmatrix}. \tag{43}$$

In Section 5.2, the hybrid numerical method is used with an optimization method to obtain shape optimization of the muffler component, based on the article [V].

4 DAMPED PRECONDITIONER METHOD

In Section 3.2, the principle of preconditioning and some preconditioner methods for the Helmholtz and Navier equations were discussed. In this chapter, an efficient preconditioning technique based on physical damping is studied. The chapter reviews articles [I, II, III].

The damped Helmholtz preconditioner was first considered in [12]. There, the scattering problems were posed in a rectangular domain that was discretized using low-order finite differences. The geometric multigrid method method was used to approximate the inversion of the damped Helmholtz preconditioner operator. In [I], this approach was extended to general shaped domains using linear, quadratic, and cubic finite element discretizations. An algebraic multigrid method (AMG) was used instead of the geometric multigrid. In [II], a further generalization was proposed by extending the method to three-dimensional problems and a similar technique was proposed for scattering problems in elastic media (the Navier problems).

For the Helmholtz equation, the preconditioning operator is called damped a Helmholtz preconditioner, or shifted-Laplacian (as in [12] and [I, III]) due to a complex shifting coefficient applied to the Laplacian operator. For the Navier equation, the preconditioning is called the damped Navier preconditioner. In [I, II], simulations were carried out in two-dimensional and three-dimensional computational domains, including complicated geometries for both the Helmholtz and Navier problems. The method was compared to the MIC-based preconditioning method in [II] and exact controllability method in [III]. Some of the results from comparison and performance measurements are given in Section 4.2.

In [57], the mathematical results were obtained that could be used in examining the eigenvalue spectrum of the preconditioned Helmholtz equation. These results can be used to estimate the convergence of an iterative method such as GMRES for the Helmholtz problems. Some of the results were generalized to the Navier equation in [II]. These are reviewed in Section 4.3.

4.1 Problem formulation

The finite element method (see Section 3.1) is used to give an approximate solution to the acoustic and elastic wave propagation problems. For the FEM, weak formulation of the corresponding problem is needed. The weak form of the Helmholtz problem (Eq. (10) on page 13) reads: Find $\hat{p} \in H^1\left(\Omega^f\right)$ such that

$$\int_{\Omega^f}\left(\boldsymbol{\nabla}\hat{p}\cdot\boldsymbol{\nabla}\bar{\hat{q}} - k^2\hat{p}\bar{\hat{q}}\right)dx - \int_{\Gamma_i^f} i\gamma k\hat{p}\bar{\hat{q}}ds = \int_{\Omega^f} f_f\bar{\hat{q}}dx \tag{44}$$

for all $\hat{q} \in H^1\left(\Omega^f\right)$. Here, Ω^f is the fluid domain and Γ_i^f is the partially absorbing boundary, where the impedance boundary condition (Eq. (11) on page 13) with the absorption coefficient γ is applied. For three-dimensional problems, the Navier equation (Eq. (16) on page 15) in weak form reads: Find $\hat{\mathbf{u}} \in \left[H^1\left(\Omega^s\right)\right]^3$ such that

$$\int_{\Omega^s}\left(-\rho_s\omega^2\hat{\mathbf{u}}\cdot\bar{\hat{\mathbf{v}}} + \sigma\left(\hat{\mathbf{u}}\right):\epsilon\left(\bar{\hat{\mathbf{v}}}\right)\right)dx - \int_{\Gamma_i^s} i\gamma\omega\rho_s\mathbf{B}\hat{\mathbf{u}}\cdot\bar{\hat{\mathbf{v}}}ds = \int_{\Omega^s}\mathbf{f}_s\cdot\bar{\hat{\mathbf{v}}}dx \tag{45}$$

for all $\hat{\mathbf{v}} \in \left[H^1\left(\Omega^s\right)\right]^3$. Here, Ω^s is the elastic domain and Γ_i^s is the partially absorbing boundary, where impedance boundary condition (Eq. (20) on page 15) with absorption coefficient γ is applied.

The finite element mesh consisting of triangles in two-dimensional and tetrahedra in three-dimensional problems is used. The discretized domain is denoted by $\Omega_h^{f,s}$; here h denotes the diameter of the largest triangle or tetrahedron. Discrete counterparts for test function spaces are denoted by V_h^f and V_h^s for fluid and elastic domains, correspondingly. For these spaces, Lagrangian polynomials of order $m = 1, 2, 3$ are used as basis functions.

Now, let the vector $\mathbf{w}$ contain the nodal values of $\hat{p}$ or $\hat{\mathbf{u}}$, so that for the Helmholtz problem it has the form $\mathbf{w} = \left[\hat{p}_1, \cdots, \hat{p}_n\right]^T$, and for the three-dimensional Navier problem it has the form $\mathbf{w} = \left[\hat{u}_1^x, \hat{u}_1^y, \hat{u}_1^z, \cdots, \hat{u}_n^x, \hat{u}_n^y, \hat{u}_n^z\right]^T$. By replacing the spaces, domains, and boundaries with their discrete counterparts, the following matrices based on integrals in Eqs. (44) and (45) are defined as follows:

$$\begin{array}{rlrl}
\mathbf{M}^f = & \int_{\Omega_h^f} k^2\hat{p}_h\bar{\hat{q}}_h dx, & \mathbf{M}^s = & \int_{\Omega_h^s}\rho_s\omega^2\hat{\mathbf{u}}_h\cdot\bar{\hat{\mathbf{v}}}_h dx,\\
\mathbf{L}^f = & \int_{\Omega_h^f}\boldsymbol{\nabla}\hat{p}_h\cdot\boldsymbol{\nabla}\bar{\hat{q}}_h dx, & \mathbf{L}^s = & \int_{\Omega_h^s}\sigma\left(\hat{\mathbf{u}}_h\right):\epsilon\left(\bar{\hat{\mathbf{v}}}_h\right)dx,\\
\mathbf{C}^f = & -\int_{\Gamma_{i,h}^f}\gamma k\hat{p}_h\bar{\hat{q}}_h ds, & \mathbf{C}^s = & -\int_{\Gamma_{i,h}^s}\gamma\omega\rho_s\mathbf{B}_s\hat{\mathbf{u}}_h\cdot\bar{\hat{\mathbf{v}}}_h ds,
\end{array} \tag{46}$$

where $\hat{p}_h, \hat{q}_h \in V_h^f$, $\hat{\mathbf{u}}_h, \hat{\mathbf{v}}_h \in V_h^s$. The system of linear equations of form $\mathbf{Aw} = \mathbf{f}$ is obtained. Denoting $z_1 = \alpha_1 + \beta_1 i$, the discretized Helmholtz and Navier operators have matrix forms

$$\mathbf{F} = \mathbf{L}^f + i\mathbf{C}^f - z_1\mathbf{M}^f \quad \text{and} \quad \mathbf{S} = z_1\mathbf{L}^s + \sqrt{z_1}i\mathbf{C}^s - \mathbf{M}^s, \tag{47}$$

respectively. The complex-valued sparse matrix $\mathbf{A}$ is now given by $\mathbf{F}$ or $\mathbf{S}$ and $\mathbf{f}$ is a vector resulting from a non-zero f_f in Eq. (44) or $\mathbf{f}_s$ in Eq. (45).

Preconditioner

A shifted-Laplacian operator

$$\mathcal{F}_d = -\boldsymbol{\nabla} \cdot \frac{1}{\rho} \boldsymbol{\nabla} - z_2 \frac{k^2}{\rho}, \tag{48}$$

with a complex shift $z_2 = \alpha_2 + \beta_2 i$ was suggested in [13] as a preconditioner for the Helmholtz equation. By choosing $\alpha_2 = 1$ and β_2 to be negative, $\mathcal{F}_d$ is the Helmholtz operator (Eq. (10) on page 13) with additional damping. Hence, it is also called the damped Helmholtz operator. Using the matrices defined in Eq. (46), the discretization of $\mathcal{F}_d$ leads to a matrix

$$\mathbf{F}_d = \mathbf{L}^f + i\mathbf{C}^f - z_2 \mathbf{M}^f. \tag{49}$$

With moderate damping, it is much easier to solve systems with $\mathbf{F}_d$ than those with $\mathbf{F}$ and the conditioning of $\mathbf{F}\mathbf{F}_d^{-1}$ is good. Here, an algebraic multigrid approximation is considered for $\mathbf{F}_d^{-1}$.

Similar physical damping can also be employed to construct an efficient preconditioner for the Navier equations, as suggested in [II]. Damping in elastic materials can be modelled by a complex Young modulus. Multiplying the original Young modulus $E(x)$ by a complex z_2 leads to a preconditioning operator

$$\mathcal{S}_d = -\omega^2 \rho_s \hat{\mathbf{u}} - z_2 \boldsymbol{\nabla} \cdot \sigma\left(\hat{\mathbf{u}}\right). \tag{50}$$

The coefficient z_2 also appears in the impedance boundary condition (Eq. (20) on page 15) as follows

$$i\gamma\omega\rho_s \sqrt{z_2} \mathbf{B}\hat{\mathbf{u}} + z_2 \sigma\left(\hat{\mathbf{u}}\right) \mathbf{n}_s = 0 \quad \text{on } \Gamma_i^s. \tag{51}$$

Using the matrices in Eq. (46), the discretization of $\mathcal{S}_d$ leads to the damped Navier preconditioner

$$\mathbf{S}_d = z_2 \mathbf{L}^s + \sqrt{z_2} i \mathbf{C}^s - \mathbf{M}^s. \tag{52}$$

Algebraic multigrid method in damped preconditioning

The multigrid method (see Section 3.2) is not used here to solve the entire problem, but, rather, only to approximate the inverse of the damped operator $\mathbf{B}^{-1}$. The approximation given by one cycle of a multigrid method is denoted by $\mathbf{B}_{MG}^{-1}$. An algebraic multigrid method (AMG) based on [30] is utilized, with modifications that make it suitable for vector valued problems, such as the Navier equation.

The employed AMG method uses a graph to construct coarse spaces in or-

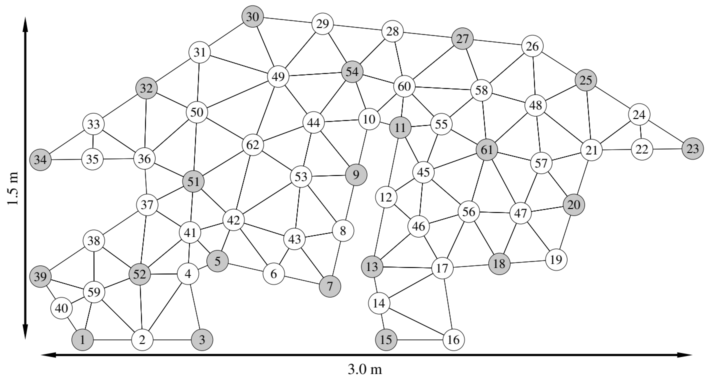

FIGURE 5 A mesh for a two-dimensional cross-section of a car cabin. Grey nodes are selected to next coarse level in the algebraic multigrid method.

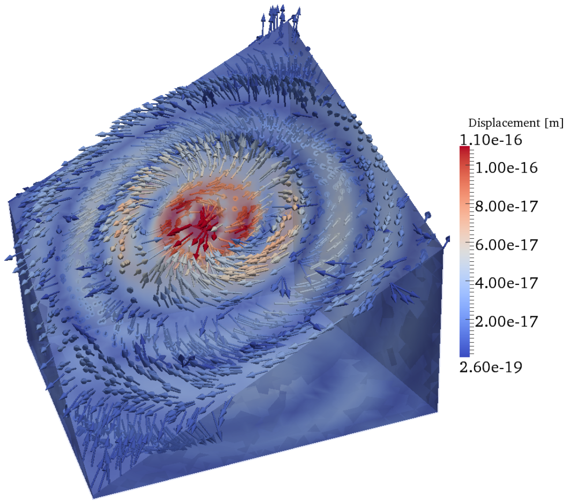

FIGURE 6 A cross-section of an example solution of the Navier equation for cube problem at frequency $f = 40\,\text{kHz}$. Arrows illustrate the displacement on the cross-section surface. The magnitude of displacement is depicted by the color.

der to solve the error equation. Here, the graph is based on the discretization mesh. An example of the coarsening procedure is shown in Figure 5. For vector-valued elasticity problems, the graph is formed without connections between displacement components. The graph for these problems consists of separate disconnected graphs, one for each displacement component.

4.2 Numerical measurements and comparison of performance

In the following, the performance of the damped preconditioner is demonstrated with some numerical results. First, the method is compared to modified incomplete Cholesky (MIC) factorization-based preconditioner [39], see Section 3.2. A three-dimensional cube problem $(0.3\,\text{m})^3$ with a point source in the middle is

TABLE 2 The iteration counts for the cube problem for the Helmholtz and Navier equations.

Helmholtz							
f [kHz]↓	AMG			MIC(0)		MIC(1)	
order→	1	2	3	1	2	1	2
0.5	10	13	16	13	17	8	11
1.0	12	15	18	18	41	11	17
2.0	19	21	24	31	126	16	28
4.0	35	42	55	50		29	
Navier							
order→	1	2		1	2	1	2
5	20	5		24	70	11	16
10	22	10		38	196	15	25
20	33	20		67		24	48
40	66			107		40	

used as an example problem. In Figure 6, a cross section of an example solution at frequency $f = 40\,\text{kHz}$ is shown for the Navier equation. The algorithm presented in [21] is used for the MIC(l) approximation of A^{-1}, where the parameter l describes the level of fill-in in the factorization. The performance is measured by the number of GMRES iterations and the total number of floating point operations (FLOPs) required by the preconditioning. The number of FLOPs is a fair measure of the performance, as it includes the initialization process in addition to the GMRES iteration.

The results are presented in Tables 2 and 3. MIC(1) requires fewer iterations than AMG, whereas MIC(0) requires more iterations. Particularly with linear finite elements, the convergence with MIC(1) is faster than with AMG and MIC(0), as can be seen in Table 2. However, Table 3 shows that the number of FLOPs with the MIC(1) preconditioner is about twice the number with AMG. This is mainly due to the expensive factorization process before the iteration. With quadratic elements, the MIC preconditioner seems to perform much worse than AMG, both in terms of iteration counts and in FLOPs. This is true for both the Helmholtz and Navier problems. MIC(1) also uses more memory than AMG, although the difference is not substantial.

In summary, the AMG-based damped preconditioner is more efficient, as its initialization requires much fewer computations than the expensive incomplete factorization procedure. Especially with quadratic finite elements, the AMG preconditioner is clearly faster.

As another example, the method is compared to the exact controllability method (see Section 3.2). The comparison for the Helmholtz problem is made in a two-dimensional square domain with a crescent-shaped scatterer, that is illustrated in Figure 7; mesh is depicted in Figure 2a. Angular frequencies $\omega = 12\pi, 24\pi, 48\pi, 96\pi, 192\pi$ are used for element orders $r = 1, 3$. The scattering problems are solved by using the constant ωh, implying approximately 10 space discretization points per wave length. For tests in the homogeneous domain, the

TABLE 3 The number of millions of floating point operations (MFLOPs) for the Helmholtz and Navier equations.

Helmholtz							
f [kHz]↓	AMG			MIC(0)		MIC(1)	
order→	1	2	3	1	2	1	2
0.5	0.5	7.4	43	0.4	13	0.5	35
1.0	2.1	31	170	2.2	110	2.9	270
2.0	17	210	1100	24	1800	32	3600
4.0	170	2000	12000	260		390	
Navier							
order→	1	2		1	2	1	2
5	6.8	130		7.1	390	8.9	870
10	29	490		47	3700	63	7000
20	230	3500		530	88000	760	93000
40	2400			5900		9400	

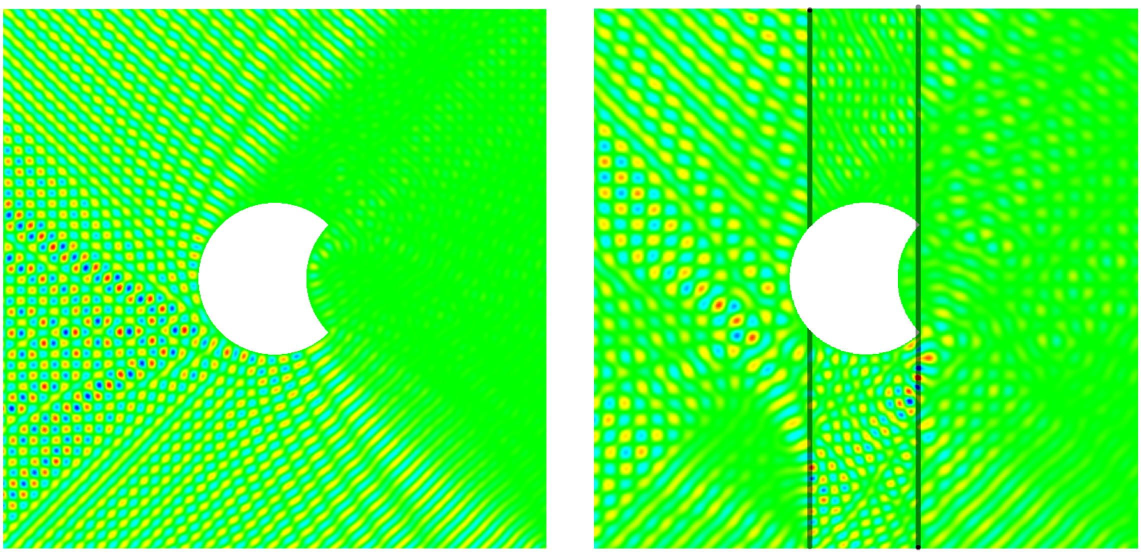

(a) Homogeneous (b) Heterogeneous

FIGURE 7 Solution of the scattering problem in homogeneous and heterogeneous domains at angular frequency $\omega = 48\pi$.

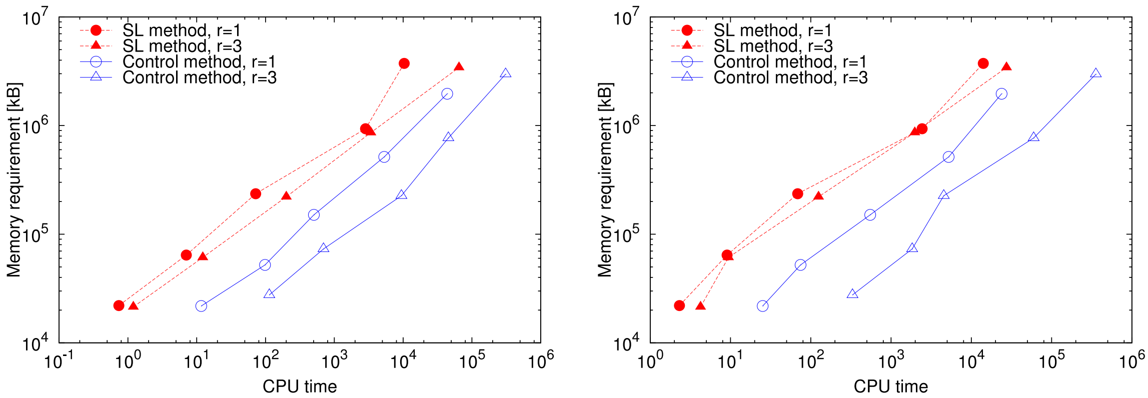

(a) Homogeneous (b) Heterogeneous

FIGURE 8 Memory usage with respect to CPU time (in seconds); comparison between the damped preconditioner method (SL method) and the exact controllability (control method). On each line, there are points for angular frequencies $\omega = 12\pi, 24\pi, 48\pi, 96\pi, 192\pi$ when ωh is a constant, giving approximately 10 discretization points per wavelength.

value $c = 1$ is used. In the heterogeneous test case, the parameters are the same, except $c = 1.5$ in narrow region in the middle, as seen in Figure 7.

The CPU times and maximum memory usage is shown in Figure 8. The damped Helmholtz preconditioning method is can be seen to be substantially faster than the exact controllability on all of the tested frequencies, with respect to CPU time. It can also be seen that, at higher frequencies, the damped Helmholtz preconditioner method uses more memory, which is due to the Krylov subspace stored by the GMRES method.

4.3 Spectral analysis and numerical study of eigenvalues

The eigenvalue spectrum of the preconditioned matrix $\mathbf{AB}^{-1}$ can be used to estimate the convergence of an iterative method such as GMRES, see [57]. Using the formulations in Eq. (46), the discretized matrices of the Helmholtz and Navier equations and their damped equivalents are

$$\mathbf{F} = \mathbf{L}^f + i\mathbf{C}^f - z_1\mathbf{M}^f, \tag{53}$$
$$\mathbf{F}_d = \mathbf{L}^f + i\mathbf{C}^f - z_2\mathbf{M}^f, \tag{54}$$
$$\mathbf{S} = z_1\mathbf{L}^s + \sqrt{z_1}i\mathbf{C}^s - \mathbf{M}^s, \tag{55}$$
$$\mathbf{S}_d = z_2\mathbf{L}^s + \sqrt{z_2}i\mathbf{C}^s - \mathbf{M}^s. \tag{56}$$

Here, matrices $\mathbf{L}^{f,s}$ and $\mathbf{C}^{f,s}$ are symmetric positive semi-definite and $\mathbf{M}^{f,s}$ are symmetric positive definite, and $z_1 = \alpha_1 + \beta_1 i$, $z_2 = \alpha_2 + \beta_2 i$ are complex numbers.

Problems without absorption

When there are only natural boundary conditions and the material is not absorbing, it holds that $\mathbf{C}^{f,s} = 0$. With this assumption matrices $\mathbf{F}$, $\mathbf{S}$ simplifies to

$$\mathbf{F} = \mathbf{L}^f - z_1 \mathbf{M}^f, \tag{57}$$

$$\mathbf{S} = z_1 \mathbf{L}^s - \mathbf{M}^s. \tag{58}$$

For the Helmholtz equation, the preconditioned eigenvalue problem $\mathbf{A}\mathbf{B}^{-1}\tilde{\boldsymbol{y}} = \tau\tilde{\boldsymbol{y}}$ is equivalent to $\mathbf{A}\boldsymbol{y} = \tau\mathbf{B}\boldsymbol{y}$, where $\boldsymbol{y} = \mathbf{B}^{-1}\tilde{\boldsymbol{y}}$, so

$$\left(\mathbf{L}^f - z_1 \mathbf{M}^f\right) \boldsymbol{y} = \tau \left(\mathbf{L}^f - z_2 \mathbf{M}^f\right) \boldsymbol{y}. \tag{59}$$

By moving terms and substituting $\lambda = \frac{z_1 - \tau z_2}{1-\tau}$, the eigenvalue problem can be written as

$$\mathbf{L}^f \boldsymbol{y} = \lambda \mathbf{M}^f \boldsymbol{y}. \tag{60}$$

As the matrix $\mathbf{L}^f$ is positive semi-definite and $\mathbf{M}^f$ is symmetric positive definite, the eigenvalues λ are real. The eigenvalue τ is a function of λ given by

$$\tau = \frac{\lambda - z_1}{\lambda - z_2}. \tag{61}$$

For the Navier equation, the preconditioned eigenvalue problem similarly reads

$$\left(z_1 \mathbf{L}^s - \mathbf{M}^s\right) \boldsymbol{y} = \tau \left(z_2 \mathbf{L}^s - \mathbf{M}^s\right) \boldsymbol{y}. \tag{62}$$

By moving terms and replacing $\lambda' = \frac{1-\tau}{z_1 - \tau z_2}$, the eigenvalue problem can be written as

$$\mathbf{L}^s \boldsymbol{y} = \lambda \mathbf{M}^s \boldsymbol{y}. \tag{63}$$

In addition, the matrix $\mathbf{L}^s$ is positive semi-definite and $\mathbf{M}^s$ is symmetric positive definite, and thus the eigenvalues λ are real. The eigenvalue τ is a function of λ given by

$$\tau = \frac{z_1}{z_2} \frac{\lambda - z_1^{-1}}{\lambda - z_2^{-1}}. \tag{64}$$

With the change of variable $\lambda' = \lambda^{-1}$, an identical relation to Eq. (61) is obtained.

The eigenvalues λ can be regarded as a real parameterization of curves in Eq. (61) on the complex plane where the eigenvalues τ of the preconditioned system are located. These curves are determined by substituting $\tau = \tau_r + i\tau_i$ into Eq. (61), treating the real and imaginary parts separately and then substituting the relation for λ from either one to another. Finally, the following relation is obtained:

$$\beta_2\tau_r^2 - (\beta_1+\beta_2)\,\tau_r + \beta_2\tau_i^2 + (\alpha_1-\alpha_2)\,\tau_i \;=\; -\beta_1. \tag{65}$$

The following theorems hold for the preconditioned Helmholtz eigenvalue problem. The theorems are introduced in [57]. A corollary for the preconditioned Navier eigenvalue problems, for one, is presented in [II].

Theorem 1. *Let $\beta_2 = 0$ and let $\mathbf{L}$ be symmetric positive semi-definite and $\mathbf{M}$ be symmetric positive definite real matrices. Then the eigenvalues $\tau = \tau_r + i\tau_i$ of*

$$(\mathbf{L}–z_1\mathbf{M})x \;=\; \tau(\mathbf{L}–z_2\mathbf{M})x \tag{66}$$

are located on the straight line in the complex plane given by

$$-\beta_1\tau_r + (\alpha_1–\alpha_2)\tau_i + \beta_1 \;=\; 0. \tag{67}$$

Proof. This follows from substituting $\beta_2 = 0$ in Eq. (61). □

Theorem 2. *Let $\beta_2 \neq 0$ and let $\mathbf{L}$ be symmetric positive semi-definite and $\mathbf{M}$ be symmetric positive definite real matrices. Then the eigenvalues $\tau = \tau_r + i\tau_i$ of Eq. (66) are located on the circle given by*

$$\left(\tau_r - \frac{\beta_2+\beta_1}{2\beta_2}\right)^2 + \left(\tau_i - \frac{\alpha_2-\alpha_1}{2\beta_2}\right)^2 = \frac{(\beta_2-\beta_1)^2 + (\alpha_2-\alpha_1)^2}{(2\beta_2)^2}. \tag{68}$$

The center of the circle is at $c = \frac{z_1-\overline{z_2}}{z_2-\overline{z_2}}$ and the radius is $R = \left|\frac{z_2-z_1}{z_2-\overline{z_2}}\right|$.

Proof. Divide Eq. (61) by $2\beta_2$ and complete the square. □

Theorem 3. *If $\beta_1\beta_2 > 0$, the origin is not enclosed by the circle defined by Eq. (68).*

Proof. The origin is not enclosed by the circle if the distance from the center to the origin is larger than the radius. This is true, as

$$\frac{(\beta_2+\beta_1)^2 + (\alpha_2-\alpha_1)^2}{(2\beta_2)^2} \;>\; \frac{(\beta_2-\beta_1)^2}{(2\beta_2)^2} + \frac{(\alpha_2-\alpha_1)^2}{(2\beta_2)^2} \tag{69}$$

□

Corollary 4. *Theorems 1-3 also hold for the eigenvalues $\tau = \tau_r + i\tau_i$ of the generalized eigenvalue problem*

$$(z_1\mathbf{L}–\mathbf{M})x \;=\; \tau(z_2\mathbf{L}–\mathbf{M})x. \tag{70}$$

This is clear, as the relation Eq. (61) also holds for this eigenvalue problem. The results can hence be applied to the damped Navier preconditioner.

The problems with absorption

The eigenvalue problems of the preconditioned Helmholtz and Navier operators, with impedance boundary conditions when absorption coefficient $\gamma \neq 0$, i.e. $\mathbf{C}^{f,s} \neq 0$, are discussed next. Due to the complex eigenvalues arising from $\mathbf{C}^{f,s}$, it is not possible to locate eigenvalues on a straight line or on a circle of the complex plane, as earlier, but useful theorems are still established in the following. The theorems are introduced in [57], in which proofs are also given, and the conjecture for the preconditioned Navier eigenvalue problems is presented in [II].

Theorem 5. *Let $\beta_2 = 0$, and let $\mathbf{L}$ and $\mathbf{C}$ be symmetric positive semi-definite and $\mathbf{M}$ be symmetric positive definite real matrices. Then the eigenvalues $\tau = \tau_r + i\tau_i$ of generalized eigenvalue problem*

$$(\mathbf{L} + i\mathbf{C} – z_1\mathbf{M})x \quad = \quad \tau(\mathbf{L} + i\mathbf{C} – z_2\mathbf{M})x \tag{71}$$

are located in the half-plane

$$-\beta_1\tau_r + (\alpha_1 - \alpha_2)\,\tau_i + \beta_1 \geq 0. \tag{72}$$

Theorem 6. *Let $\beta_2 < 0$ and let $\mathbf{L}$ and $\mathbf{C}$ be symmetric positive semi-definite and $\mathbf{M}$ be symmetric positive definite real matrices. Then the eigenvalues $\tau = \tau^r + i\tau^i$ of Eq. (71) are inside or on the circle with the center at $c = \frac{z_1 - \overline{z_2}}{z_2 - \overline{z_2}}$ and the radius $R = \left|\frac{z_2 - z_1}{z_2 - \overline{z_2}}\right|$. If $\beta_2 > 0$, the eigenvalues $\tau = \tau^r + i\tau^i$ of Eq. (71) are outside or on the same circle.*

It is not evident that Theorems 5 and 6 are applicable for the Navier equation. However, the numerical experiments reported in [II] suggest that similar behavior also holds here. This is stated in the form of the following conjecture.

Conjecture 7. *Let $\mathbf{L}$, $\mathbf{C}$ and $\mathbf{M}$ be matrices that are constructed for the Navier problem as in Eq. (46). For the eigenvalues $\tau = \tau^r + i\tau^i$ of the generalized eigenvalue problem*

$$(z_1\mathbf{L}^s + \sqrt{z_1}i\mathbf{C}^s – \mathbf{M}^s)x \quad = \quad \tau(z_2\mathbf{L}^s + \sqrt{z_2}i\mathbf{C}^s – \mathbf{M}^s)x \tag{73}$$

the following statements hold. If $\beta_2 = 0$, the eigenvalues are located in the half-plane

$$-\beta_1\tau^r + (\alpha_1 - \alpha_2)\,\tau^i + \beta_1 \geq 0. \tag{74}$$

If $\beta_2 > 0$ the eigenvalues are inside or on the circle with the center at $c = \frac{z_1 - \overline{z_2}}{z_2 - \overline{z_2}}$ and the radius $R = \left|\frac{z_2 - z_1}{z_2 - \overline{z_2}}\right|$. If $\beta_2 < 0$, the eigenvalues are outside or on the same circle.

Numerical experiment

As an example of the above results for the eigenvalue spectrum of the damped Helmholtz and Navier problems, results of an example problem are presented

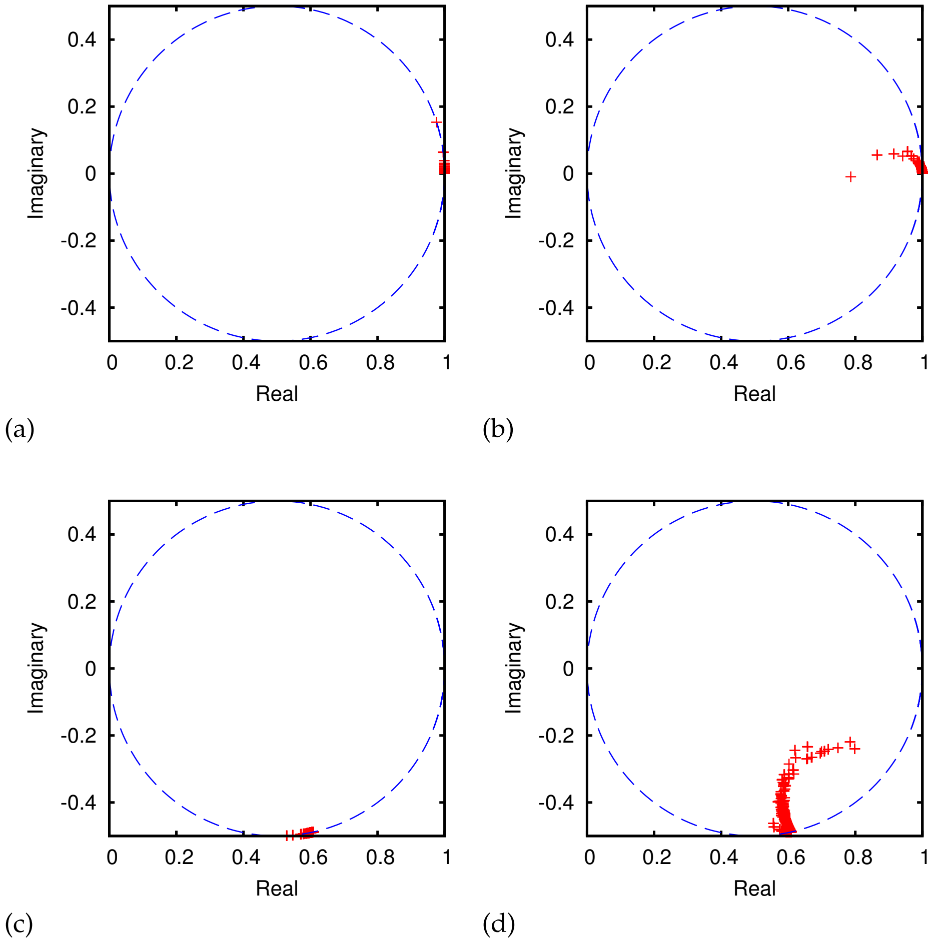

FIGURE 9 The eigenvalues of $\mathbf{AB}^{-1}$ for the three-dimensional cube problem. The upper plots are for the Helmholtz problems and the lower ones are for the Navier problems. The left plots are without absorption and the right ones are for problems with absorbing boundary conditions.

next. The three-dimensional cube of size $(0.3\,\mathrm{m})^3$ is discretized by using linear finite elements for both the Helmholtz and Navier problems. For the Navier problem, the frequency f is 5 kHz and for the Helmholtz problem, the frequency f is 500 Hz. In Figure 9, the eigenvalues of $\mathbf{AB}^{-1}$ are plotted. The circle of Eq. (68) is drawn in these figures. In Figures 9a, 9b, 9c, and 9d, the numerical results are consistent with Theorem 2, Theorem 6, Corollary 4, and Conjecture 7, respectively.

5 SOUND CONTROL PROBLEMS

Machine generated noise is an increasing problem in many modern environments. Rotating and constantly moving parts such as wheels, engines, and cooler fans are typical noise sources. It is often possible to achieve a significant reduction in noise levels by implementing different noise control methods. Noise reduction is important in factories, engineering vehicles, and passenger cars. Moreover, reducing transmitted noise in ductworks, such as exhaust mufflers or ventilation systems, is often desirable.

Generally, the most effective technique for noise reduction is to remove or reduce important noise source mechanisms with suitable design choices. A design may have resonant modes at critical frequencies, which further amplify the noise. Optimization can be performed, with respect to shape or materials in order to remove these resonances and reduce noise. However, there are circumstances in which it is not possible to alter a design or in which a design is influenced by factors more significant than noise.

Two basic approaches for noise attenuation are passive and active noise control methods. Passive noise control methods fall into two categories: dissipative and reactive methods. Dissipative noise control employs noise absorbing and insulating material and it is best suited for high frequency noise. It is less effective for low frequency noise, as long waves require large elements. Reactive noise control exploits the shape of a passive element in order to obtain useful wave reflections that reduce noise. These methods are better suited at low frequencies and are mainly used in reactive mufflers, as in Section 5.2.

Active noise control (ANC) [46] is an approach that is suitable particularly for low frequency noise reduction. Active attenuation is based on generating antisound with actuators, such that the original noise is canceled. The antisound must have the same amplitude as the noise to be canceled, but the opposite phase such that destructive interference occurs. The idea of this technology was presented in a patent by Paul Lueg [36] in 1936, but there have not been many successful applications until recent times. Due to the development and decrease in cost of digital signal processing audio circuits, more and more active noise control applications have appeared in recent years. This has promoted the research

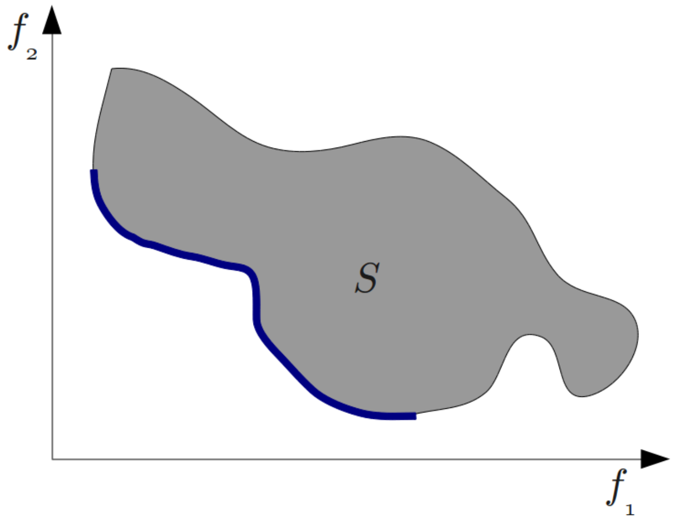

FIGURE 10 A front of Pareto optimal solutions (thick blue line) in a feasible region S (grey area).

interest on the field.

This chapter is organized as follows: In Section 5.1, an introduction to solving optimization problems is given; In Section 5.2, the noise control in duct systems by optimizing the shape of the reactive muffler component is discussed, on the basis of article [V]; In Section 5.3, a selection of other shape optimization articles that deal with Helmholtz problems are reviewed; In Section 5.4, a computational method utilizing a stochastic domain to estimate the effectiveness of an active noise control method is described, on the basis of article [IV].

5.1 Solving an optimization problem

The purpose of optimization is to find the best solution to a problem within all possible solutions. Optimization is performed with respect to a specified objective. If there are many objectives, the problem is called a multiobjective optimization problem. The general formulation of a multiobjective optimization problem reads as follows:

$$\begin{aligned} &\min_{\mathbf{x}\in S} f_1(\mathbf{x}) \\ &\quad\vdots \\ &\min_{\mathbf{x}\in S} f_m(\mathbf{x}), \end{aligned} \tag{75}$$

where $f_i : \mathbb{R}^n \to \mathbb{R}$ are objective functions that depend (often indirectly) on $\mathbf{x} \in S$, a vector consisting of design variables x_i that are optimized in a feasible region S of design space $\mathbb{R}^n$. For example, when shape optimization is considered, the vector $\mathbf{x}$ defines the shape of the optimized design.

In a single-objective optimization problem, the optimal solutions have obvious definition. When there are many objective functions, the optimal solution is more ambiguous and the concept of Pareto optimality is needed. A solution is called Pareto optimal if no other solution exists that is better with respect to all of the objective functions.An illustration of Pareto optimality is presented in Figure 10. Similarly, a solution is called non-dominated, if no other solution within a group of (possibly non-optimal) solutions exists that is better with respect to all of the objective functions.

There are various different approaches in solving optimization problems. Genetic algorithms [50] are stochastic evolutionary optimization algorithms [6] that mimic genetic drift and the Darvinian struggle for survival. The methods are based on evolving a population of solutions that are applied with operators originating from a natural evolutionary process: selection, crossover and mutation. Unlike traditional gradient-based optimizers [51] that need the derivatives and a good starting point, genetic algorithms have a good opportunity to locate the global optimum in a near-optimal manner. However, the optimality is not guaranteed with these methods. The non-dominated sorting genetic algorithm, NSGA-II [7], is a popular multiobjective genetic algorithm and it is used as an optimization method in Section 5.2. Other techniques for multiobjective optimization are discussed in [43], for example.

5.2 Shape optimization of a reactive muffler

A method for improving the attenuation properties of reactive mufflers by shape optimization is considered. The objective is to simultaneously minimize transmission of acoustic waves at multiple frequency ranges simultaneously. This task is formulated as a multiobjective optimization problem.

The sound transmission loss function is defined as the ratio of the transmitted to incident sound powers

$$TL\left(\mathbf{x}, f\right) \quad = \quad -10\,\log_{10}\frac{\rho_A \sum_{m=0}^{n_B}\gamma_m H_m \left|B_m\right|^2}{\rho_C \sum_{m=0}^{n_B}\lambda_m I_m \left|F_m\right|^2}, \tag{76}$$

where $I_n = \int_{\Gamma_A} \left|\Phi_n\right|^2 dx$ and $H_m = \int_{\Gamma_B} \left|\Psi_m\right|^2 dx$, using the notations introduced in Section 3.4. The function $\tau\left(\mathbf{x}, f\right)$ is defined as

$$\tau\left(\mathbf{x}, f\right) \quad = \quad \min\left(TL\left(\mathbf{x}, f\right), TL_{max}\right). \tag{77}$$

Here, parameter TL_{max} is a limiting value for transmission loss, which is necessary due to the possible narrow infinite peaks in transmission loss function that inhibit good convergence of the optimizer.

The multiobjective optimization problem is defined as a minimization of objective functions

$$f_1(\mathbf{x}) = -\frac{1}{n_1}\sum_{i=1}^{n_\omega}\tau(\mathbf{x},\omega_i) \qquad \text{and} \qquad f_2(\mathbf{x}) = -\frac{1}{n_2}\sum_{i=1}^{n_\iota}\tau(\mathbf{x},\iota_i), \tag{78}$$

where the shape vector $\mathbf{x} = [x_1, \ldots, x_{n_{vars}}]$ contains design variables that are used to alter the shape of the muffler component, $\boldsymbol{\omega} = [\omega_1, \ldots, \omega_{n_\omega}]$ and $\boldsymbol{\iota} = [\iota_1, \ldots, \iota_{n_\iota}]$ are vectors of frequencies in which sound transmission loss is maximized. The optimization is made with the non-dominated sorting genetic algorithm, NSGA-II [7], which is an optimizer well suited for multiobjective problems. The acoustics of the muffler component is evaluated with the hybrid numerical method that is described in Section 3.4.

Numerical experiment

As a numerical example problem, the shape optimization of a muffler component consisting of five variable-radius cylinders is investigated. In Figure 11a, a schematic illustration of the problem is presented. In addition to the radius of each cylinder, the length of inlet and outlet ducts are optimization variables as well. The length of the muffler component is $L = 1000$ mm and the diameters of inlet and outlet ducts are $d = 100$ mm. The length of inlet and outlet ducts x_1, x_2 can vary between $[20, 900]$ mm and the diameter of each cylinder $x_{3\ldots7}$ is between $[120, 240]$ mm. Transmission loss is optimized in two frequency ranges: between 200-300 Hz and 500-600 Hz.

In Figure 12, there are four non-dominated fronts of objective functions in Eq. (78) that are obtained by NSGA-II after 120 generations. The fronts can be seen to converge at the same line. Before optimization, the average fitness functions values of the randomly generated initial population were $f_1 = -13$ dB and $f_2 = -15$ dB. In Figure 13, the transmission loss as a function of frequency is plotted for an optimal solution, which is chosen from the non-dominated front at $f_1 = -43.16$ dB, $f_2 = -42.97$ dB. The optimal parameters are used in example solution, Figure 11b. In Figure 13, it can be seen that the transmission loss level improved significantly at both frequency ranges.

5.3 Other shape optimization problems

The optimization of an acoustic horn has been discussed in [2, 58, 59]. The objective of the study is to implement a general method for designing acoustic horns with a prescribed set of properties. In [2], the shape of the horn is optimized to improve impedance matching between the horn and the surrounding air at specified frequencies, implying efficient sound radiation from horn to the surroundings. This work is extended to include topology optimization in [58]. In [59], both shape and topology optimization techniques are performed simultaneously

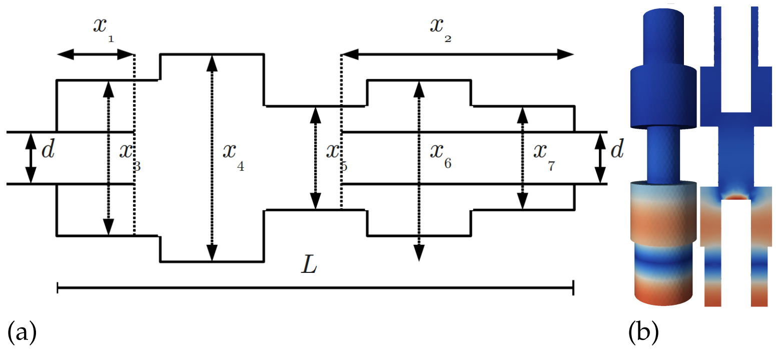

FIGURE 11 In the left figure, there is a diagram of the muffler component used. In the right figure, the pressure time average of optimal solution is plotted at frequency $f = 600$ Hz.

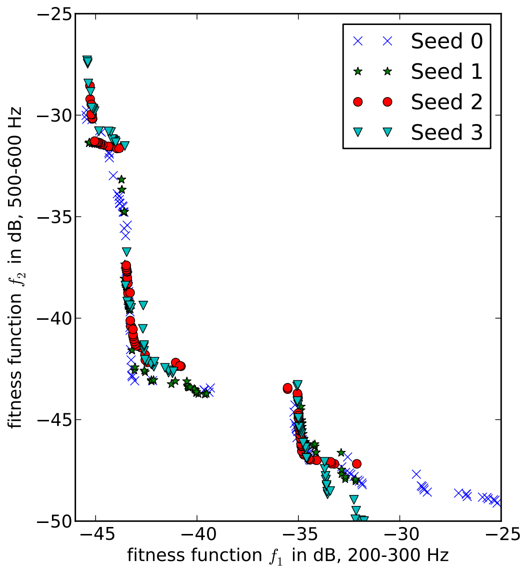

FIGURE 12 The non-dominated fronts of the optimization of the muffler component are plotted, four different random seeds.

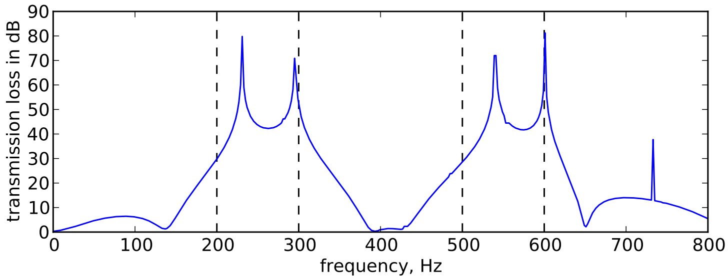

FIGURE 13 The transmission loss as a function of frequency. The transmission loss is maximized at frequency ranges 200-300 Hz and 500-600 Hz.

in order to construct an optimal acoustic horn-lens combination with optimized transmission efficiency and directivity properties. A significant performance improvement of the acoustic horn is reported in these studies.

Multidisciplinary shape optimization of an airfoil, with respect to drag and electromagnetic backscatter, is studied in [41]. The drag coefficient is calculated by CFD analysis and the electromagnetic backscatter calculation requires the solution of the two-dimensional Helmholtz equation. Optimization is performed with a multiobjective genetic algorithm.

The shape optimization of an ultrasonic transducers have been considered in [23, 24]. The transducers are of the Langevin type, which is a standard component in high-power ultrasonics, used to perform, e.g. ultrasonic cleaning and chemical processing. In both articles, a two-dimensional axisymmetrical finite element discretization of piezoelectric equations is used to model the transducer. In [24], the piezoelectric equations were coupled to the Helmholtz equation in order to model the transmission of acoustic vibrations to water. In [23], a single-objective shape optimization is performed using the SQP method, with respect to three objective functions separately. In [24], a multiobjective NIMBUS method is used to optimize all three objective functions simultaneously. Significantly improved transducer designs are reported in the study.

5.4 Active noise control estimation in a stochastic domain

Since there are several low-frequency noise sources in a car cabin environment, an active noise control (ANC) [46] system could provide significant noise reduction. There are several ways of implementing a three-dimensional ANC system, but they are not very effective or universally applicable yet. Numerical simulation and optimization can be used to study and improve ANC systems. Examples on the use of finite element modelling are presented in articles [3, 52]. In [52], the resonance modes for a mining vehicle are studied by modal coupling analysis and anti-noise is optimized by using an FEM model in order to obtain global noise control in the cabin. In [3], a local active noise control method based on the finite element method is described, which minimizes noise locally in the microphone locations. A method for determining the optimal locations for anti-noise actuators is also presented. In [60], an optimal active noise control implementation based on quadratic programming and boundary element method (BEM) is presented.

In ordinary finite element analysis, it is assumed that the model geometry and boundary conditions are accurately known. In reality, this is rarely the case and there is considerable uncertainty in the specification of models. This motivates stochastic treatment of the problem, i.e. letting inaccurate measures be random variables. Stochastic finite element methods [19, 8, 20] can be used to address this issue in modelling. In [10], for example, the solution of stochastic PDE is represented in an outer product form, which allows a generation of various statistical quantities with moderate computation.

In this section, a novel modelling method for the local control of sound by anti-noise actuators is introduced in a stochastic domain, based on article [IV]. The method can be used to assess the possibilities of active noise control in enclosed acoustic spaces such as vehicle cabins. The anti-noise is optimized by minimizing the expected value of the noise computed using the finite element method. By including the stochasticity of the cavity domain in the model, the optimal performance of a local sound control can be determined more accurately and reliably than with the earlier methods.

Optimal actuator signal evaluation in a stochastic domain

An acoustic model in an enclosed stochastic domain $\Omega(\mathbf{r})$ is considered, where $\mathbf{r} = (r_1, r_2, \cdots, r_n)^T$ is a random variable that conforms to a known probability distribution $F(\mathbf{r})$. The complex pressure amplitude $\hat{p}(\mathbf{x}, \mathbf{r}, \gamma)$ (see Eq. (9) on page 13) is the sum of the sound pressures caused by noise and n anti-noise sources:

$$\hat{p}(\mathbf{x}, \mathbf{r}, \gamma) = \hat{p}_0(\mathbf{x}, \mathbf{r}) + \sum_{j=1}^{n} \gamma_j \hat{p}_j(\mathbf{x}, \mathbf{r}), \tag{79}$$

where the pressure amplitude $\hat{p}_0$ is due to the noise source, $\hat{p}_j$ is due to the jth anti-noise source, and γ_j is a complex coefficient defining the amplitude and phase of the jth anti-noise source. The noise and anti-noise sources are located on the boundary surfaces of Ω. The anti-noise defined by the coefficients γ_j is optimized so that the noise is minimized in a subdomain denoted by $\Xi(\mathbf{r}) \subset \Omega(\mathbf{r})$. For this, a noise measure is defined as

$$\begin{aligned} N(\mathbf{r}, \gamma) &= \int\limits_{\Xi(\mathbf{r})} |\hat{p}(\mathbf{x}, \mathbf{r}, \gamma)|^2 g(\mathbf{x})\, d\mathbf{x} \\ &= \int\limits_{\Xi(\mathbf{r})} \hat{p}(\mathbf{x}, \mathbf{r}, \gamma)\, \bar{\hat{p}}(\mathbf{x}, \mathbf{r}, \gamma)\, g(\mathbf{x})\, d\mathbf{x}, \end{aligned} \tag{80}$$

where $g(\mathbf{x})$ is a weighting function and $\bar{\hat{p}}$ is the complex conjugate of $\hat{p}$.

As the domain Ω is stochastic, the expected value of the noise measure is given by

$$E(N(\mathbf{r}, \gamma)) = \int N(\mathbf{r}, \gamma)\, F(\mathbf{r})\, d\mathbf{r}, \tag{81}$$

where $F(\mathbf{r})$ is the probability distribution of $\mathbf{r}$. The objective function J for optimization is chosen to be an approximation of the integral Eq. (81) and it is given by the numerical quadrature

$$J(\gamma) = \sum_{j=1}^{m} w_j N\left(\mathbf{r}_j, \gamma\right) F\left(\mathbf{r}_j\right), \tag{82}$$

where the pairs $\left(\mathbf{r}_j, w_j\right)$ give the quadrature points and weights. The optimization problem is defined as

$$\min_{\gamma} J(\gamma). \tag{83}$$

In order to formulate the objective function in a compact form, the following notations are introduced:

$$\begin{aligned}
\hat{\mathbf{p}}(\mathbf{x},\mathbf{r}) &= \left(\hat{p}_1(\mathbf{x},\mathbf{r}), \hat{p}_2(\mathbf{x},\mathbf{r}), \cdots, \hat{p}_n(\mathbf{x},\mathbf{r})\right)^T, \\
a &= \sum_{j=1}^{m} w_j F\left(\mathbf{r}_j\right) \int\limits_{\Xi(\mathbf{r}_j)} \hat{p}_0\left(\mathbf{x},\mathbf{r}_j\right)^2 g(\mathbf{x})\, d\mathbf{x}, \\
\mathbf{b} &= \sum_{j=1}^{m} w_j F\left(\mathbf{r}_j\right) \int\limits_{\Xi(\mathbf{r}_j)} \hat{p}_0\left(\mathbf{x},\mathbf{r}_j\right) \bar{\hat{\mathbf{p}}}\left(\mathbf{x},\mathbf{r}_j\right) g(\mathbf{x})\, d\mathbf{x}, \quad \text{and} \\
\mathbf{A} &= \sum_{j=1}^{m} w_j F\left(\mathbf{r}_j\right) \int\limits_{\Xi(\mathbf{r}_j)} \hat{\mathbf{p}}^T\left(\mathbf{x},\mathbf{r}_j\right) \bar{\hat{p}}\left(\mathbf{x},\mathbf{r}_j\right) g(\mathbf{x})\, d\mathbf{x},
\end{aligned} \tag{84}$$

where $\bar{\hat{\mathbf{p}}}$ is the elementwise complex conjugate of the vector $\hat{\mathbf{p}}$ and the superscript ^{T} denotes the transpose. By expanding the terms and by using the notations in Eq. (84), the objective function in Eq. (82) can be expressed in the form

$$J(\gamma) = \gamma^H \mathbf{A} \gamma + \gamma^H \mathbf{b} + \mathbf{b}^H \gamma + a, \tag{85}$$

where superscript ^{H} stands for the Hermitian conjugate. Optimal complex coefficients γ_i that give phases and amplitudes for anti-noise actuators, are now given by the optimality condition $\nabla_\gamma J = \mathbf{0}$. This leads to a system of linear equations $\mathbf{A}\gamma = -\mathbf{b}$, which has the solution

$$\gamma = -\mathbf{A}^{-1}\mathbf{b}. \tag{86}$$

Local noise control inside the car cabin

As a numerical example application, the local noise control inside a BMW 330i car cabin is studied, see Figure 14. The domain $\Omega(\mathbf{r})$ is the interior of the car, excluding the driver. The objective of the noise control is to minimize noise in the

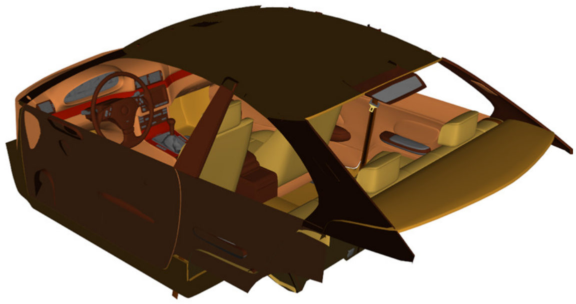

FIGURE 14 A three-dimensional model of the car cabin of a BMW 330i.

driver's ears. Thus, Ξ is defined as a set

$$\Xi(\mathbf{r}) = \{\mathbf{e}_l, \mathbf{e}_r\} \subset \Omega(\mathbf{r}), \tag{87}$$

where $\mathbf{e}_l(\mathbf{r})$ and $\mathbf{e}_r(\mathbf{r})$ are the coordinates of the left and right ear, respectively. The noise measure in Eq. (80) has now the expression

$$N(\mathbf{r},\gamma) = |\hat{p}(\mathbf{e}_l,\mathbf{r},\gamma)|^2 + |\hat{p}(\mathbf{e}_r,\mathbf{r},\gamma)|^2 .$$

It is assumed that there is only the driver and no other passengers or significant objects in the car that would influence the sound propagation. The driver's variable properties, such as shape and posture, have an impact on the reflections and propagation of sound, and must therefore be taken into account. The posture and position of the driver's head particularly affect the sound audible to the driver. As the posture varies to some extent, it is better to minimize the expected value of the sound level in the driver's ears. This leads to a stochastic domain in the computation.

Three parameters are considered here: r_1 is the driver's sideways bending angle, r_2 is the forward bending angle, and r_3 is the driver's head rotation angle to left/right. These parameters are illustrated in Figure 15. The random variable $\mathbf{r} = (r_1, r_2, r_3)^T$ determines the posture of the driver, where the value of each parameter is limited by condition $L_i < r_i < H_i$, $i \in \{1,2,3\}$. The expected value in Eq. (81) reads now

$$E(N(\mathbf{r},\gamma)) = \int\limits_{r_1=L_1}^{H_1} \int\limits_{r_2=L_2}^{H_2} \int\limits_{r_3=L_3}^{H_3} N(\mathbf{r},\gamma)\, F(\mathbf{r})\, dr_3 dr_2 dr_1. \tag{88}$$

The numerical integration gives the objective function

$$J(\gamma) = E(N(\mathbf{r},\gamma)) = \sum_{i=1}^{m} w_i N(\mathbf{r}_j,\gamma)\, F(\mathbf{r}_j), \tag{89}$$

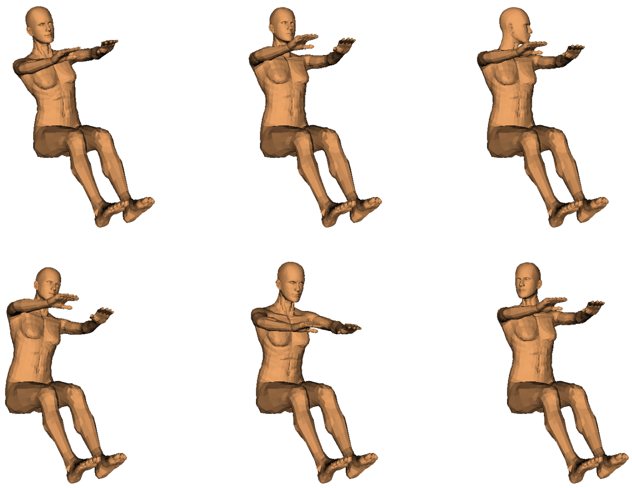

(a) r_1 (b) r_2 (c) r_3

FIGURE 15 Driver's posture parameters: (a) r_1 is the driver's sideways bending angle, (b) r_2 is the forward bending angle, (c) r_3 is the head rotation angle to left/right. The upper figures correspond to the lowest value of the parameter and the lower figures correspond to the highest value of the parameter.

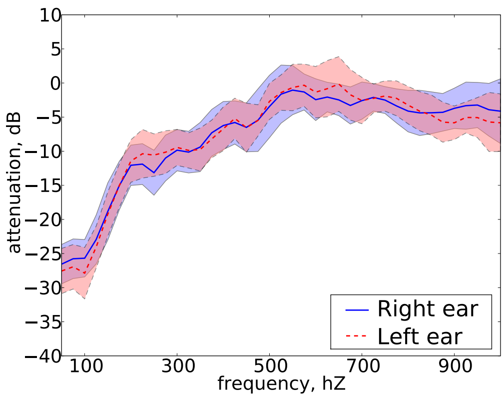

FIGURE 16 The expected value of attenuation in the left and right ears and standard deviation σ (shaded region).

where w_i is a weight coefficient from the numerical integration rule of the probability distribution function F and $\mathbf{r}_i$ is the coordinate triplet of the ith quadrature point.

To evaluate the objective function in Eq. (89), the pressure amplitude – caused by each noise and anti-noise source – in the driver's ears is needed for each driver sample $\mathbf{r}_i$. Here, the acoustic reciprocity principle (Section 2.1) allows a significant computational saving, since it is sufficient to solve acoustic problems using only sound sources from the driver's ears.

Numerical experiment results

In Figure 16, the expected value of the noise attenuation and its weighted standard deviation have been plotted at each of the driver's ears. Two door loud-

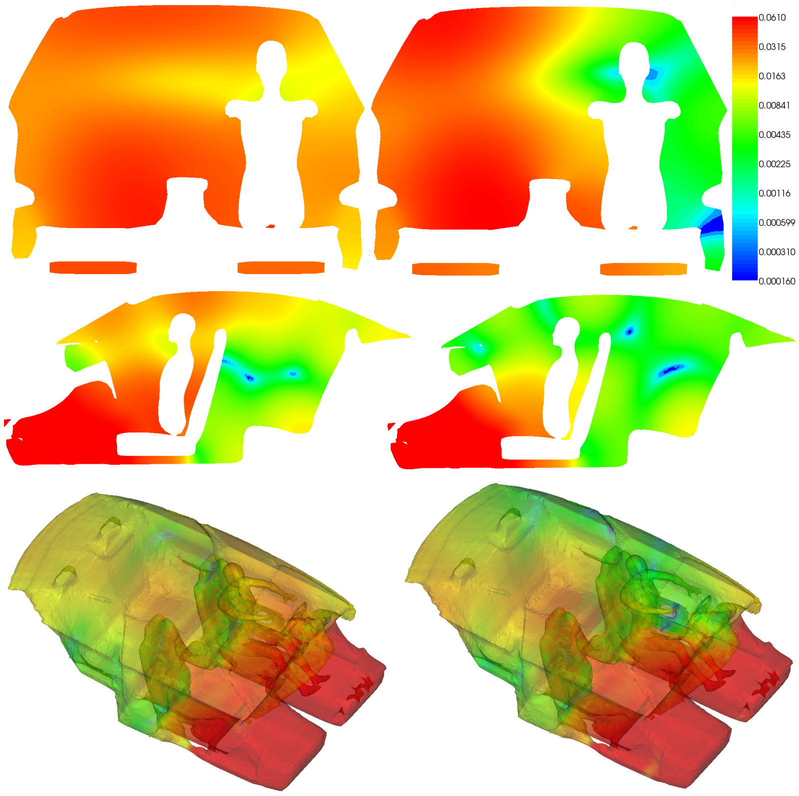

FIGURE 17 The noise control at frequency $f = 300\,\text{Hz}$ for the basic driver's parameters $r_1 = r_2 = r_3 = 0$. The modulus of pressure amplitude $|p|$ is plotted on the logarithmic color scale. In the left plots, the acoustic field is depicted without noise control. In the right plots, the noise control is enabled. The attenuation at both ears in this case is approx. $-30\,\text{dB}$. The front door loudspeakers are used in the noise control.

speakers are used as anti-noise actuators. A good noise control is obtained within the engine noise frequency range, below 500 Hz. By this choice of anti-noise actuators, however, the noise reduction result is not good at higher frequencies, although the expected value of the attenuation stays negative; i.e. the noise is reduced. By adding more anti-noise actuators, the noise reduction is improved at higher frequencies, as reported in [IV].

Figure 17 demonstrates the effect of active noise control with two actuators at a single frequency $f = 300\,\text{Hz}$. The method can be seen to effectively reduce noise near the ears and also in a wider region around the ears. At higher frequencies, the silent area is smaller and the noise is increased in other parts of the car.

6 CONCLUSIONS

The dissertation discussed numerical methods for sound and vibration simulation and simulation-based optimization and control. The first part of the dissertation introduced an effective method for computational modelling of acoustic and elastic wave propagation. The second part investigated two methods for designing efficient noise control systems: a method for designing optimal reactive muffler components by shape optimization and a numerical method for optimizing the local control of sound in a stochastic domain.

The first part of the dissertation was based on articles [I, II, III]. The focus was on introducing an efficient numerical solver for time-harmonic acoustic and elastic wave equations – the Helmholtz and Navier equations. The solver was based on preconditioning the discrete wave equation with a damped variant of the equation. This approach was a generalization of a shifted-Laplacian preconditioner for the Helmholtz equation that was introduced in [12], where finite difference discretizations were used on rectangular domains and a geometric multigrid was used to solve the preconditioner equation. The method that was introduced here used finite element discretizations and an algebraic multigrid method to invert the preconditioner operator, which gave two major advantages: complicated three-dimensional problems could be solved and higher-order finite elements could be used to provide higher accuracy. The method appeared to be particularly efficient for both the Helmholtz and Navier problems at low-frequency and mid-frequency scales.

The second part of the dissertation concentrated on two different noise control problems, based on articles [IV, V]. First, multiobjective shape optimization with respect to sound transmission loss was examined in a reactive muffler component of a duct system. A hybrid numerical method was used to solve the acoustic field in a ductwork with a non-uniform muffler component. This method matches modal representations of the solution with a finite element approximation in the muffler. Because of the mode matching, the hybrid method provided accurate and realistic modelling of acoustics in the muffler component. The transmission loss was maximized simultaneously at multiple frequencies and a multiobjective genetic algorithm was used as an optimizer. The method offered an advanced, generic and robust approach to complicated three-dimensional muffler shape optimization problems.

Second, a method to assess the effectiveness of optimal anti-noise was introduced for local sound control in stochastic three-dimensional enclosures. The acoustic modelling was performed in the frequency domain using a sequence of finite element discretizations of the Helmholtz equation. The optimization of anti-noise was performed by minimizing the expected value of the noise at each frequency. This led to a robust and accurate noise control in varying domains. The method was demonstrated on a three-dimensional car cabin (BMW 330i) and significant noise reduction was obtained, particularly at low frequencies.

The numerical methods presented herein offer useful tools for many practical acoustic applications. Efficient solvers are required for modelling large-scale acoustic fields, and ever more difficult acoustic optimization problems are becoming solvable by efficient numerical methods and the increasing performance of modern computer technology. The solver and noise control techniques presented in this dissertation offer a competitive tool in many acoustical simulation and noise control design applications.

YHTEENVETO (FINNISH SUMMARY)

Väitöskirjan suomenkielinen otsikko on "Laskennallisia menetelmiä akustisiin ongelmiin ja melunvaimennukseen". Väitöstyö käsittelee tietokonemallinnukseen perustuvia laskennallisia menetelmiä, joiden avulla voidaan ratkaista akustisten ja elastisten ääniaaltojen etenemiseen liittyviä ongelmia ja suunnitella tehokkaita melunhallintajärjestelmiä.

Väitöskirjan ensimmäisessä osassa esitellään tehokas ratkaisumenetelmä, jonka avulla voidaan ratkaista aikaharmonisia aaltoyhtälöitä akustisissa ja elastisissa alueissa. Äänivärähtelyn etenemistä mallinnetaan matemaattisesti osittaisdifferentiaaliyhtälöiden avulla: akustisessa materiaalissa Helmholtzin yhtälöllä ja elastisessa alueessa Navierin yhtälöllä. Yhtälöt ratkaistaan likimääräisesti äärellisten elementtien menetelmällä, joka johtaa lineaariseen yhtälöryhmään. Esitellyssä menetelmässä alkuperäiselle yhtälölle muodostetaan pohjustin, joka vastaa aaltoyhtälöä sopivalla vaimennuksella. Tätä pohjustinta käytetään tehtävän ratkaisemisessa Krylovin aliavaruusmenetelmillä (kuten esimerkiksi GMRES). Vaimennettua aaltoyhtälöä vastaavan kerroinmatriisin käänteismatriisia voidaan tehokkaasti arvioida algebrallisella monihilamenetelmällä. Tutkimuksessa osoittautui, että menetelmä on tehokas erityisesti matala- ja keskitaajuusalueilla. Menetelmä soveltuu monimutkaisiin kolmiulotteisiin tehtäviin, joissa materiaalin ominaisuudet vaihtelevat laskenta-alueessa.

Väitöskirjan toinen osa käsittelee melunvaimennukseen soveltuvia menetelmiä. Melunhallintamenetelmät jakautuvat kahteen pääryhmään: aktiivisiin ja passiivisiin menetelmiin. Aktiiviset melunhallintamenetelmät pyrkivät kumoamaan alkuperäisen melun lähettämällä vastakkaisvaiheista vastamelua, ottaen aktiivisesti sensorien avulla huomioon tilassa vallitsevan melun. Passiiviset melunhallintamenetelmät toimivat vallitsevan melun suhteen passiivisesti ja perustuvat yleensä erilaisiin äänenvaimennuselementteihin. Passiivisiin menetelmiin lukeutuvat putkijärjestelmissä käytettävät äänenvaimentimet, kuten esimerkiksi auton pakoputki. Nämä toimivat joko dissipatiivisesti, eli vaimentamalla melua sopivalla ääntä absorboivalla materiaalilla, tai reaktiivisesti, eli kumoamalla melua sopivien muotojen avulla saatavien heijastusten avulla. Väitöstyössä tarkastellaan yksityiskohtaisesti kahta erilaista melunhallintamenetelmää: reaktiiviseen passiiviseen melunhallintaan perustuvaa menetelmää ja aktiiviseen melunhallintaan perustuvaa menetelmää.

Ensimmäiseksi tarkastellaan menetelmää, jolla voidaan suunnitella optimaalisia reaktiivisia melunvaimennuskomponentteja putkirakenteisiin. Äänen eteneminen putkijärjestelmässä mallinnetaan hybridimenetelmällä, jossa vaimennuskomponentissa käytetään äärellisten elementtien menetelmää ja säännöllisessä putkiosassa hyödynnetään tunnettua analyyttistä aaltomuotoa. Hybridimenetelmän ansiosta vaimennuskomponentin akustiikka mallinnetaan tarkasti ja realistisesti. Vaimenninkomponentin muotoa optimoidaan sen aikaansaaman melunvaimennuksen suhteen. Vaimennus maksimoidaan samanaikaisesti usealla taajuudella säätämällä reaktiivisen äänenvaimenninkomponentin muotoa. Melunvaimennuksen optimointiongelma on muotoiltu monitavoiteoptimointiongelmana ja se ratkaistaan monitavoitteisella geneettisellä algoritmilla (NSGA-II). Menetelmä osoittautuu soveltuvaksi monimutkaisten kolmiulotteisten vaimenninkomponenttien muodonoptimointiin.

Toiseksi tarkastellaan menetelmää, jolla voidaan arvioida aktiivisen melunhallinnan tehokkuutta satunnaisessa laskenta-alueessa. Menetelmää käytettäessä kolmiulotteisen suljetun tilan akustiikka mallinnetaan taajuusavaruudessa käyttäen äärellisten elementtien menetelmällä saatavaa sarjaa Helmholtzin yhtälön ratkaisuista. Vastamelu optimoidaan minimoimalla melun odotusarvoa halutussa taajuusalueessa. Esimerkkitehtävänä työssä on esitelty melunvaimennus auton (BMW 330i) sisätilassa. Sisätilaan on sijoitettu akustisia vastameluaktuaattoreita määrättyihin paikkoihin. Esimerkissä laskenta-alueen satunnaisuus johtuu kuljettajan asennosta, jonka oletetaan muuttuvan satunnaisesti noudattaen tunnettua satunnaisjakaumaa. Menetelmällä saadaan aikaan merkittävä äänenvaimennus erityisesti matalilla taajuuksilla.

Esitellyt laskennalliset menetelmät tarjoavat käyttökelpoisia työkaluja moniin käytännöllisiin akustiikkasovelluksiin. Tehokkaita ratkaisijoita tarvitaan suuren mittaluokan akustisten kenttien numeeriseen ratkaisemiseen. Tulevaisuudessa yhä vaikeampia akustisia optimointiongelmia voidaan ratkaista tehokkaiden ratkaisijamenetelmien sekä yhä tehokkaampien tietokoneiden ansioista. Väitöskirjassa esitellyt ratkaisija- ja melunhallintamenetelmät tarjoavat kilpailukykyisen työkalun useissa akustiikkasimuloinnin sekä melunvaimennuksen suunnittelun sovelluksissa.

REFERENCES

[1] R. J. Astley, FE mode-matching schemes for the exterior Helmholtz problem and their relationship to the FE-DtN approach, Commun. Numer. Meth. En. 12 (4) (1996) 257–267.

[2] E. Bängtsson, D. Noreland, M. Berggren, Shape optimization of an acoustic horn, Comput. Method. Appl. M. 192 (11-12) (2003) 1533–1571.

[3] A. Bermúdez, P. Gamallo, R. Rodríguez, Finite element methods in local active control of sound, SIAM J. Control Optim. 43 (2) (2004) 437–465.

[4] M. O. Bristeau, R. Glowinski, J. Périaux, Controllability methods for the computation of time-periodic solutions; application to scattering, J. Comput. Phys. 147 (2) (1998) 265–292.

[5] F. Collino, S. Ghanemi, P. Joly, Domain decomposition method for harmonic wave propagation: a general presentation, Comput. Methods Appl. Mech. Engrg. 184 (2-4) (2000) 171–211.

[6] K. Deb, Multi-objective optimization using evolutionary algorithms, John Wiley & Sons, Ltd., 2001.

[7] K. Deb, A. Pratap, S. Agarwal, T. Meyarivan, A fast elitist multi-objective genetic algorithm: NSGA-II, IEEE T. Evolut. Comput. 6 (2000) 182–197.

[8] M. K. Deb, I. M. Babuška, J. T. Oden, Solution of stochastic partial differential equations using galerkin finite element techniques, Comput. Method. Appl. M. 190 (48) (2001) 6359–6372.

[9] H. C. Elman, O. G. Ernst, D. P. O'Leary, A multigrid method enhanced by Krylov subspace iteration for discrete Helmholtz equations, SIAM J. Sci. Comput. 23 (4) (2001) 1291–1315.

[10] H. C. Elman, O. G. Ernst, D. P. O'Leary, M. Stewart, Efficient iterative algorithms for the stochastic finite element method with application to acoustic scattering, Comput. Method. Appl. M. 194 (9-11) (2005) 1037–1055.

[11] B. Engquist, A. Majda, Radiation boundary conditions for acoustic and elastic wave calculations, Commun. Pur. Appl. Math. 32 (1979) 313–357.

[12] Y. A. Erlangga, C. W. Oosterlee, C. Vuik, A novel multigrid based preconditioner for heterogeneous Helmholtz problems, SIAM J. Sci. Comput. 27 (4) (2006) 1471–1492.

[13] Y. A. Erlangga, C. Vuik, C. W. Oosterlee, On a class of preconditioners for solving the Helmholtz equation, Appl. Numer. Math. 50 (3-4) (2004) 409–425.

[14] O. G. Ernst, A finite-element capacitance matrix method for exterior Helmholtz problems, Numer. Math. 75 (2) (1996) 175–204.

[15] E. Faccioli, F. Maggio, A. Quarteroni, A. Tagliani, Spectral-domain decomposition methods for the solution of acoustic and elastic wave equations, Geophysics 61 (4) (1996) 1160–1174.

[16] F. Fahy, Some applications of the reciprocity principle in experimental vibroacoustics, Acoust. Phys. 49 (2) (2003) 217–229.

[17] F. Fahy, P. Gardonio, Sound and Structural Vibration.

[18] C. Farhat, P. Avery, R. Tezaur, J. Li, FETI-DPH: a dual-primal domain decomposition method for acoustic scattering, J. Comput. Acoust. 13 (3) (2005) 499–524.

[19] R. Ghanem, Ingredients for a general purpose stochastic finite elements implementation, Comput. Method. Appl. M. 168 (1-4) (1999) 19–34.

[20] R. Ghanem, P. Spanos, Stochastic finite elements: A spectral approach, Springer-Verlag, New York, 1991.

[21] I. Gustafsson, Modified incomplete Cholesky (MIC) methods, in: Preconditioning methods: analysis and applications, vol. 1 of Topics in Comput. Math., Gordon & Breach, New York, 1983, pp. 265–293.

[22] E. Heikkola, Y. A. Kuznetsov, P. Neittaanmäki, J. Toivanen, Fictitious domain methods for the numerical solution of two-dimensional scattering problems, J. Comput. Phys. 145 (1) (1998) 89–109.

[23] E. Heikkola, M. Laitinen, Model-based optimization of ultrasonic transducers, Ultrason. Sonochem. 12 (2005) 53–57.

[24] E. Heikkola, K. Miettinen, P. Nieminen, Multiobjective optimization of ultrasonic transducers using NIMBUS, Ultrasonics 44 (4) (2006) 368–380.

[25] E. Heikkola, S. Mönkölä, A. Pennanen, T. Rossi, Controllability method for acoustic scattering with spectral elements, J. Comput. Appl. Math. 204 (2) (2007) 344–355.

[26] E. Heikkola, T. Rossi, J. Toivanen, A parallel fictitious domain method for the three-dimensional Helmholtz equation, SIAM J. Sci. Comput. 24 (5) (2003) 1567–1588.

[27] F. Ihlenburg, Finite element analysis of acoustic scattering, vol. 132 of Applied Mathematical Sciences, Springer-Verlag, New York, 1998.

[28] F. Ihlenburg, Computational Aspects of Structural Acoustics and Vibration, chap. Sound in Vibrating Cabins: Physical Effects, Mathematical Formulation, Computational Simulation with FEM, No. 505 in CISM International Centre for Mechanical Sciences, Springer, Vienna, 2009, pp. 103–170.

[29] K. Ito, Z. Qiao, J. Toivanen, A domain decomposition solver for acoustic scattering by elastic objects in layered media, J. Comput. Phys. 227 (19) (2008) 8685–8698.

[30] F. Kickinger, Algebraic multi-grid for discrete elliptic second-order problems, in: Multigrid methods V (Stuttgart, 1996), Springer, Berlin, 1998, pp. 157–172.

[31] L. E. Kinsler, A. R. Frey, A. B. Coppens, J. V. Sanders, Fundamentals of acoustics, John Wiley, New York, 1982.

[32] R. Kirby, Modeling sound propagation in acoustic waveguides using a hybrid numerical method, J. Acoust. Soc. Am. 124 (4) (2008) 1930–1940.

[33] V. Kupradze, An introduction to boundary element methods, CRC Press, 1995.

[34] A. L. Laird, M. B. Giles, Preconditioned iterative solution of the 2D Helmholtz equation, Tech. Rep. 02/12, Oxford Computer Laboratory, Oxford, UK (2002).

[35] L. Landau, Theory of elasticity, Pergamon Press, Oxford, 1975.

[36] P. Lueg, Process of silencing sound oscillations, U.S. Patent #2,043,416 issued Jun 1936 (filed 1933).

[37] R. H. Lyon, Statistical energy analysis of dynamical systems, M.I.T. Press, 1975.

[38] R. H. Lyon, R. H. Maidanik, Power flow between linearly coupled oscillators, J. Acoust. Soc. Am. (34) (1962) 623–639.

[39] M. Magolu monga Made, Incomplete factorization-based preconditionings for solving the Helmholtz equation, Internat. J. Numer. Methods Engrg. 50 (2001) 1077–1101.

[40] F. Magoulès (ed.), Computational methods for acoustics problems, Saxe-Coburg Publications, 2008.

[41] R. A. E. Mäkinen, J. Périaux, J. Toivanen, Multidisciplinary shape optimization in aerodynamics and electromagnetics using genetic algorithms, Int. J. Numer. Meth. Fl. 30 (2) (1999) 149–159.

[42] T. Mertens, A new mapped infinite partition of unity method for convected acoustical radiation in infinite domains, Ph.D. thesis, Université Libre de Bruxelles (2009).

[43] K. Miettinen, Nonlinear multiobjective optimization, International Series in Operations Research & Managemenent Science, Springer, 1998.

[44] K. W. Morton, D. Mayers, Numerical solution of partial differential equations, Cambridge university press, 1994.

[45] M. L. Munjal, Acoustics of ducts and mufflers, Chichester: John Wiley, 1987.

[46] P. A. Nelson, S. J. Elliot, Active control of sound, Academic Press, London, 1999.

[47] Y. Saad, Iterative methods for sparse linear systems, 2nd ed., Society for Industrial and Applied Mathematics (SIAM), Philadelphia, PA, 2003.

[48] Y. Saad, M. H. Schultz, GMRES: a generalized minimal residual algorithm for solving nonsymmetric linear systems, SIAM J. Sci. Statist. Comput. 7 (3) (1986) 856–869.

[49] P. Shorter, R. Langley, Vibro-acoustic analysis of complex systems, J. Sound Vib. 288 (3) (2005) 669–699, uncertainty in structural dynamics.

[50] S. N. Sivanandam, S. N. Deepa, Introduction to genetic algorithms, Springer, 2009.

[51] J. Snyman, Practical mathematical optimization: An introduction to basic optimization theory and classical and new gradient-based algorithms, Applied Optimization, Springer, 2005.

[52] D. A. Stanef, C. H. Hansen, R. C. Morgans, Active control analysis of mining vehicle cabin noise using finite element modelling, J. Sound Vib. 277 (1-2) (2004) 277–297.

[53] A. Toselli, O. Widlund, Domain decomposition methods - algorithms and theory, Springer-Verlag, Berlin, 2005.

[54] U. Trottenberg, C. W. Oosterlee, A. Schüller, Multigrid, Academic Press, 2001.

[55] E. Turkel, Numerical methods and nature, J. Sci. Comput. 28 (2-3) (2006) 549–570.

[56] H. A. van der Vorst, Bi-CGSTAB: a fast and smoothly converging variant of Bi-CG for the solution of nonsymmetric linear systems, SIAM J. Sci. Statist. Comput. 13 (2) (1992) 631–644.

[57] M. van Gijzen, Y. Erlangga, C. Vuik, Spectral analysis of the discrete Helmholtz operator preconditioned with a shifted Laplacian, SIAM J. Sci. Comput. 29 (5) (2007) 1942–1958.

[58] E. Wadbro, M. Berggren, Topology optimization of an acoustic horn, Comput. Method. Appl. M. 196 (1-3) (2006) 420–436.

[59] E. Wadbro, R. Udawalpola, M. Berggren, Shape and topology optimization of an acoustic horn-lens combination, J. Comput. Appl. Math. 234 (6) (2010) 1781–1787.

[60] T. C. Yang, C. H. Tseng, Effective optimization-based approach for designing active noise control systems in enclosures, Finite Elem. Anal. Des. 15 (4) (1994) 303–316.

[61] L.-J. Yeh, Y.-C. Chang, M.-C. Chiu, Shape optimal design on double-chamber mufflers using simulated annealing and a genetic algorithm, Turkish J. Eng. Env. Sci. 29 (2005) 207–224.

ORIGINAL ARTICLES

I

AN ALGEBRAIC MULTIGRID BASED SHIFTED-LAPLACIAN PRECONDITIONER FOR THE HELMHOLTZ EQUATION

by

Tuomas Airaksinen, Erkki Heikkola, Anssi Pennanen, Jari Toivanen

Journal of Computational Physics 226 (2007) 1196-1210

Available online at www.sciencedirect.com
ScienceDirect
Journal of Computational Physics 226 (2007) 1196–1210
JOURNAL OF COMPUTATIONAL PHYSICS
www.elsevier.com/locate/jcp

An algebraic multigrid based shifted-Laplacian preconditioner for the Helmholtz equation

Tuomas Airaksinen [a,*], Erkki Heikkola [b], Anssi Pennanen [a], Jari Toivanen [c]

[a] *Department of Mathematical Information Technology, University of Jyväskylä, P.O. Box 35 (Agora), FI-40014 University of Jyväskylä, Finland*
[b] *Numerola Oy, P.O. Box 126, FI-40101 Jyväskylä, Finland*
[c] *Institute for Computational and Mathematical Engineering, Building 500, Stanford University, Stanford, CA 94305, USA*

Received 26 January 2007; received in revised form 11 May 2007; accepted 14 May 2007
Available online 26 May 2007

Abstract

A preconditioner defined by an algebraic multigrid cycle for a damped Helmholtz operator is proposed for the Helmholtz equation. This approach is well suited for acoustic scattering problems in complicated computational domains and with varying material properties. The spectral properties of the preconditioned systems and the convergence of the GMRES method are studied with linear, quadratic, and cubic finite element discretizations. Numerical experiments are performed with two-dimensional problems describing acoustic scattering in a cross-section of a car cabin and in a layered medium. Asymptotically the number of iterations grows linearly with respect to the frequency while for lower frequencies the growth is milder. The proposed preconditioner is particularly effective for low-frequency and mid-frequency problems.

Keywords: Algebraic multigrid method; Finite element method; GMRES; Helmholtz equation; Preconditioner

1. Introduction

Acoustic scattering problems have applications in many disciplines. These problems can be typically modeled using wave equation and often it is sufficient to consider only time-harmonic solutions which are described by the Helmholtz equation (reduced wave equation). For numerical simulation the equations can be discretized using the finite difference method or the finite element method, for example. The solution of resulting systems of linear equations can be a computationally challenging problem.

During the past few decades, numerical methods for acoustics have been under active research. Finite element method has emerged as a generic tool for discretizing the Helmholtz equation in complex geometries. A recent review [1] offers a glance at research efforts in this field. The efficiency of these methods still often limits the feasible size of scattering problems in mid-frequency and high-frequency regime. Particularly the phase shift (pollution)

* Corresponding author. Tel.: +358 14 260 2743; fax: +358 14 260 2771.
E-mail address: tuomas.airaksinen@jyu.fi (T. Airaksinen).

0021-9991/$ - see front matter
doi:10.1016/j.jcp.2007.05.013

error in discretizations necessitates finer meshes for high-frequency problems [2]. The finite element method have been used successfully for interior problems like scattering in a car cabin [3] as well as for exterior problems. Since the paper [4] the research on the construction of absorbing boundary conditions and absorbing layers at the truncation boundary of the exterior domain has been active; see [1] and references therein.

The resulting systems of linear equations from the discretization of the Helmholtz equation are non-Hermitian and indefinite. Furthermore, for mid-frequency and high-frequency problems, the systems can be extremely large. These reasons make them a challenge for the current solvers. Often it is feasible to use direct methods for solving these systems for two-dimensional problems, but three-dimensional problems lead to systems which cannot be solved by these methods with affordable computing effort. Hence, it is necessity to use iterative methods such as the GMRES method [5] or the BICGSTAB method [6]. However, these methods require a good preconditioner for the discretized Helmholtz equations in order to have reasonably fast convergence.

Various preconditioners and iterative solution techniques have been proposed for the discrete Helmholtz equation. Several domain decomposition methods have been proposed; see [7–11], for example. Multigrid methods have been considered in [12–14]. With multigrid methods, it is difficult to define a stable and sufficiently accurate coarse grid problems and smoothers for them. For problems in homogenous medium, domain imbedding/fictitious domain methods in [15–17] have been fairly effective. An incomplete factorization preconditioner has been considered in [18], for example, and in [19] a tensor product preconditioner is used. An alternative iterative approach for solving the Helmholtz equation has been proposed in [20] and further studied in [21]. The basic idea is to find a time-periodic solution to the wave equations using a controllability method, which leads to preconditioned conjugate gradient iterations for initial data.

In this paper, we consider shifted-Laplacian preconditioners which are obtained from the Helmholtz operator by adding damping. A recent review [22] gives a glance at this class of preconditioners utilizing the properties of the differential equation rather than the algebraic form of the discretized problem. The Laplace operator was proposed as a preconditioner for the Helmholtz equation in [23]. A shifted-Laplacian preconditioner obtained by changing the sign of the zeroth-order term in the Helmholtz operator was described in [24]. As a generalization the Laplacian with a complex shift was studied in [25]. Following this approach a multigrid preconditioner based on a damped Helmholtz operator was considered in [14]. There, the scattering problems were posed in a rectangular domain, they were discretized using low-order finite differences, and a geometric multigrid method was used. In [26], this preconditioner was used with a finite element discretization and in [27] with an absorbing perfectly matched layer. This paper extends this approach for general shaped domains using linear, quadratic, and cubic finite element discretizations. Particularly quadratic and cubic finite elements help to reduce the number of unknowns in order to reach prescribed accuracy, as they have much smaller interpolation and phase shift errors than linear basis functions [2]. Our preconditioner is based on an algebraic multigrid method which can be constructed fully algebraically when the matrix for the zeroth-order terms is also available.

There is a wide range of applications for acoustic scattering in the industry and sciences. In many applications the aim is to reduce the noise level. As an example of such a problem we consider the noise in a car cabin; see also [3]. Geophysical surveys employ acoustic/elastic backscattering from different layers to reconstruct a model for the subsurface. These problems lead to very large-scale scattering problems. We consider a three layer wedge model [19,14] in our numerical experiments. Acoustic scattering simulations have also many applications in medicine, sonar, and sound preproduction, for example.

This paper is organized as follows. In Section 2 we describe the Helmholtz model problem and its discretization. The iterative solution and preconditioning based on shifted-Laplacian preconditioners are discussed in Section 3. The algebraic multigrid method employed in the preconditioning is described in Section 4. Then numerical results are presented in Section 5 and finally, conclusions are given in Section 6.

2. Scattering problem and finite element discretization

Under suitable assumptions on medium, acoustic scattering can be described by the wave equation

$$c^2\nabla\cdot\frac{1}{\rho}\nabla p-\frac{1}{\rho}\frac{\partial^2 p}{\partial t^2}=0, \tag{1}$$

where $p(\mathbf{x},t)$ is pressure field, $\rho(\mathbf{x})$ is the density of the material, $c(\mathbf{x})$ is the speed of sound and t is time. For a time-harmonic pressure $p(\mathbf{x},t) = u(\mathbf{x})\mathrm{e}^{-\mathrm{i}\omega t}$, where ω is angular velocity and $\mathrm{i} = \sqrt{-1}$, (1) leads to the Helmholtz equation

$$-\nabla \cdot \frac{1}{\rho}\nabla u - \frac{k^2}{\rho}u = 0, \tag{2}$$

where $k(\mathbf{x}) = \omega/c(\mathbf{x})$ is the wave number. In inhomogeneous medium the wave number k varies depending on location as the sound speed c varies.

We consider three types of boundary conditions. In order to describe them, we decompose the boundary $\Gamma = \partial\Omega$ into three non-overlapping parts Γ_d, Γ_s, and Γ_a such that $\Gamma = \Gamma_d \cup \Gamma_s \cup \Gamma_a$. Some of these boundary sets can be empty. The first type of boundary is sound-soft which is described by the Dirichlet boundary condition

$$u = g(\mathbf{x}) \quad \text{on } \Gamma_d, \tag{3}$$

where g describes the sound source, for example, an incident field. The second type is the impedance boundary condition

$$\frac{\partial u}{\partial \mathbf{n}} = \mathrm{i}\gamma k u \quad \text{on } \Gamma_a, \tag{4}$$

where $\gamma(\mathbf{x})$ is an absorbency coefficient in the range $[0,1]$ describing the amount of absorption on the boundary Γ_a. The specific case $\gamma = 0$, leading to a Neumann boundary condition, corresponds to a sound-hard boundary without any absorption.

Exterior problems are truncated into a bounded domain Ω with Γ_s as the truncation boundary. The boundary condition on Γ_s should let outgoing waves propagate out of the domain without any reflection, as the Sommerfeld radiation condition describes. Such a perfect absorbing boundary condition is a non-local operator which is computationally difficult. Instead, it is usual to approximate it by a local operator [28,29,4]. Here we use an absorbing boundary condition

$$\frac{\partial u}{\partial \mathbf{n}} = \mathrm{i}k u \quad \text{on } \Gamma_s. \tag{5}$$

The methods studied here can be also used with higher-order absorbing boundary conditions.

For the weak formulation of the Helmholtz equation, we define the test function space

$$V = \{v \in H^1(\Omega) : v = 0 \text{ on } \Gamma_d\} \tag{6}$$

and the solution space

$$V_g = \{v \in H^1(\Omega) : v = g(\mathbf{x}) \text{ on } \Gamma_d\}. \tag{7}$$

Now the weak form of (2) reads: Find $u \in V_g$ such that

$$\int_\Omega \frac{1}{\rho}(\nabla u \cdot \nabla v - k^2 uv)\mathrm{d}x - \int_{\Gamma_a} \frac{1}{\rho}(\mathrm{i}\gamma k uv)\,\mathrm{d}s - \int_{\Gamma_s} \frac{1}{\rho}(\mathrm{i}k uv)\,\mathrm{d}s = 0 \tag{8}$$

for all $v \in V$.

For a finite element discretization, we define a triangulation given by a set of non-overlapping triangles K_h, such that $\Omega_h = \bigcup_{\tau \in K_h} \tau$. Here h denotes the diameter of the largest triangle and Ω_h is an approximation of Ω. An example of a coarse triangulation (also called mesh) for a cross-section of a car cabin is shown in Fig. 1. For the finite elements of order m a discrete test function space is

$$V_h = \{v_h \in H^1(\Omega_h) : v_h|_\tau \in P^m, \forall \tau \in K_h, v = 0 \text{ on } \Gamma_{d,h}\}, \tag{9}$$

where P^m denotes polynomials of order m. A discrete solution space $V_{g,h}$ is obtained similarly by approximating g on $\Gamma_{d,h}$ instead of zero. In this paper, we employ linear, quadratic, and cubic finite elements, that is, $m = 1$, 2, or 3.

In the following, we discuss briefly the errors in the finite element solutions and the influence of order of finite elements. The best approximation u_h^{opt} on V_h for u is given by

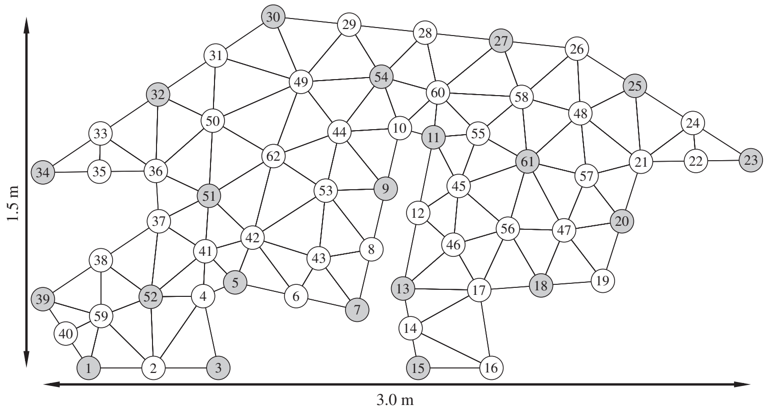

Fig. 1. A mesh for a cross-section of a car cabin. Gray nodes are selected to next coarse level.

$$u_h^{\mathrm{opt}} = \operatorname*{argmin}_{v_h \in V_h} \|v_h - u\|. \tag{10}$$

Here and in the following, we use the L^2-norm. According to error estimates [30,31,2] for the finite element solution u_h and the best approximation u_h^{opt}, we have

$$e_h = \|u_h - u\| \leqslant Ck(kh)^{2m} \quad \text{and} \quad \|u_h^{\mathrm{opt}} - u\| \leqslant C(kh)^{2m}, \tag{11}$$

where C is a constant. The additional k in the right-hand side for the finite element error e_h is caused by the pollution error. In order to have the error e_h below some given $E < C$, the mesh step size h must satisfy

$$h \leqslant (C/E)^{2m} k^{-1} k^{-1/(2m)}. \tag{12}$$

The last term $k^{-1/(2m)}$ is due to the pollution error. Based on this inequality higher orders of the finite elements allow us to attain the same level of accuracy with larger mesh steps. Furthermore, it shows that the pollution error has reduced influence on the maximum mesh step size for larger m, that is, higher-order elements help to decrease the pollution error.

We use Lagrangian basis functions for the spaces V_h and $V_{g,h}$. Let the vector $\mathbf{u}$ contain the nodal values of u. Then using the discrete spaces instead of V and V_g in (8) and integrating over the discrete counterparts of the domain and boundaries, we obtain a system of linear equations

$$\mathbf{Au} = \mathbf{f}, \tag{13}$$

where $\mathbf{A}$ is a sparse matrix and $\mathbf{f}$ is a non-zero vector due to the inhomogenous Dirichlet boundary condition. The approximation properties of such finite element discretizations for the Helmholtz equation have been studied in [2]. For an algebraic definition of the preconditioner described in Section 3, we define a mass matrix like $\mathbf{M}$ which includes the term k^2/ρ, that is, it corresponds to the integral

$$\int_{\Omega_h} \frac{k^2}{\rho} u_h v_h \, \mathrm{d}x, \tag{14}$$

where $u_h \in V_{g,h}$ and $v_h \in V_h$. Furthermore, we define the matrix $\mathbf{K} = \mathbf{A} + \mathbf{M}$ which contains the rest of the terms in the weak form.

3. Iterative solution and shifted-Laplacian preconditioner

The matrix $\mathbf{A}$ in (13) is indefinite and symmetric, but not Hermitian. Hence, the generalized minimal residual (GMRES) method [5] and the BICGSTAB method [6] are suitable iterative methods for the solution of the system (13). For these and other applicable iterative methods, see [32], for example. At each iteration, the GMRES method minimizes the norm of the residual vector on a Krylov subspace associated to the iteration. This is a desirable property leading to a monotonic reduction of residual norm over iterations, but a disadvantage is that a basis for the Krylov subspace needs to be formed and stored. Due to this the computational cost of the GMRES methods grows quadratically with iterations and the memory requirement grows linearly. With the BICGSTAB method the computational cost grows linearly and the memory requirement is independent of number of iterations, but convergence can be erratic and slower than with the GMRES method. In the numerical experiments we use the full GMRES method without restarts.

For medium- and large-scale scattering problems, the system (13) is badly conditioned, which leads to a very slow convergence of Krylov subspace methods when applied directly to the system (13). In order to improve the conditioning and the speed of convergence, we use a right preconditioner denoted by $\mathbf{B}$. This leads to a preconditioned system

$$\mathbf{AB}^{-1}\tilde{\mathbf{u}} = \mathbf{f}. \tag{15}$$

Once $\tilde{\mathbf{u}}$ is solved from this system, the solution $\mathbf{u}$ is obtained as $\mathbf{u} = \mathbf{B}^{-1}\tilde{\mathbf{u}}$. Our aim is to find such a preconditioner $\mathbf{B}$ that the matrix $\mathbf{AB}^{-1}$ is well conditioned and that vectors can be multiplied by $\mathbf{B}^{-1}$, that is, solve systems with $\mathbf{B}$, with a small computational effort. These properties would lead to a fast convergence of the iterative method and to a small overall computational cost.

In 2004, Erlangga et al. suggested in [25] to construct a preconditioner $\mathbf{B}_{\mathrm{SL}}$ by discretizing a shifted-Laplace operator

$$\mathscr{B}_{\mathrm{SL}} = -\nabla \cdot \frac{1}{\rho}\nabla - (\beta_1 + \beta_2 \mathrm{i})\frac{k^2}{\rho}, \tag{16}$$

where we have added the density $\rho(\mathbf{x})$ in the operator. Using the notations defined in Section 2, the preconditioner can be defined algebraically as

$$\mathbf{B}_{\mathrm{SL}} = \mathbf{K} - (\beta_1 + \beta_2 \mathrm{i})\mathbf{M} \tag{17}$$

which includes boundary term in $\mathbf{K}$.

By choosing $\beta_1 = 1$ and β_2 to be positive, $\mathscr{B}_{\mathrm{SL}}$ is the original Helmholtz operator with some additional damping. Such damping leads to good conditioning of $\mathbf{AB}_{\mathrm{SL}}^{-1}$ and it is easier to solve systems with $\mathbf{B}_{\mathrm{SL}}$ than with $\mathbf{A}$ [25]. In [14], Erlangga et al. approximated the inverse of the shifted-Laplacian preconditioner $\mathbf{B}_{\mathrm{SL}}$ using one cycle of a geometric multigrid method; see [33], for example. We denote such multigrid based preconditioners by $\mathbf{B}_{\mathrm{MG}}$. This leads to a good conditioning of $\mathbf{AB}_{\mathrm{MG}}^{-1}$ for low-frequency problems, while the number of BICGSTAB iterations appeared to grow linearly with frequency for high-frequency problems. They also showed that this preconditioner is well suited for problems with a highly varying speed of sound. In this paper, we replace the geometric multigrid method with a more generic algebraic multigrid method described in Section 4.

For the GMRES method, convergence estimates can be derived based on the spectrum of a matrix and its non-normality [5,32]. Similarly to [25,14], we study numerically the spectrum of the preconditioned matrices. For small problems, it is possible to compute the spectrum, while for larger problems we can only approximate it. The GMRES method forms the basis for a Krylov subspace using the Arnoldi iteration. After m iterations it has generated an $m \times m$ upper Hessenberg matrix which is usually denoted by $\mathbf{H}_m$. The eigenvalues of $\mathbf{H}_m$ approximate the eigenvalues of the system matrix.

4. Algebraic multigrid method

The preconditioner $\mathbf{B}_{\mathrm{MG}}$ is based on an algebraic multigrid (AMG) method which approximates the multiplication by the inverse of $\mathbf{B}_{\mathrm{SL}}$. We use an AMG method introduced by Kickinger in [34] with modifications proposed in [35]. This method uses a graph based on the system matrix to construct coarse spaces. Furthermore, it eliminates the degrees of freedom associated to the Dirichlet boundaries after forming the matrices for the coarse spaces. Under these choices, the AMG method can be constructed in such a way that the coarse problems coincide with the ones obtained using a geometric multigrid method on a hierarchical linear finite element mesh.

The AMG initialization procedure is described by Algorithm 1. For linear finite elements, the initial graph G_0 is the graph defined by the sparse matrix $\mathbf{B}_{\mathrm{SL}}$. Alternatively it can be seen as the graph defined by the triangulation. For quadratic and cubic elements, the graph is defined by a refined triangulation in which quadratic elements are divided into four triangles, and cubic elements are divided into nine triangles. The reason not to use directly the graph defined by $\mathbf{B}_{\mathrm{SL}}$ for higher-order elements is that the coarsening procedure would coarsen the graph too much, leading to a slower convergence, that is, to not so well conditioned $\mathbf{AB}_{\mathrm{SL}}^{-1}$. The nodes (vertices) in the graph G_0 associated with the Dirichlet boundaries are marked. On the coarser graphs also the nodes which were marked as Dirichlet nodes on the finer graphs are marked.

The nodes onto a coarser graph G_{k+1} are chosen from the nodes of G_k as follows. Find the node in G_k which has the smallest degree, that is, the smallest number of edges associated to it. If there are several such nodes, choose the first one according to the used node numbering. This node is included onto the graph G_{k+1}. Eliminate this node and all its neighbors from the graph G_k. There is one exception to this: if the node has a Dirichlet marked neighbor then the neighbor is not eliminated from G_k. This increases the stability of the procedure by making sure that there are sufficiently many Dirichlet nodes selected to the coarse levels. Repeat this procedure until there are no nodes left in G_k. Fig. 1 shows an example of this coarsening strategy when all boundaries are of Dirichlet type.

After choosing the nodes on G_{k+1}, they are numbered following their order on G_k. Then the restriction matrix $\mathbf{R}_k$ is defined by

$$(\mathbf{R}_k)_{ij} = \begin{cases} 1 & \text{for a fine node } j \text{ which is a coarse node } i, \\ \frac{1}{k} & \text{for a fine node } j \text{ which is a neighbor of coarse,} \\ & \text{node } i \text{ and has } k \text{ neighboring coarse nodes,} \\ 0 & \text{otherwise,} \end{cases}$$

where fine and coarse refers to the graphs G_k and G_{k+1}, respectively. The edges of the coarse graph G_{k+1} are formed using the restriction matrix $\mathbf{R}_k$. Each coarse graph node corresponds to a row in the restriction matrix and there is an edge between two nodes if and only if the corresponding rows of the restriction matrix have a non-zero element in the same column.

The prolongation matrix is the transpose of the restriction matrix, and a coarser grid system matrix is constructed by Galerkin method, that is, the fine grid matrix is multiplied by R_k from the left side and by R_k^{T} from the right side. The AMG cycle described by Algorithm 2 is a usual multigrid cycle given here in the general μ-cycle form. The choices $\mu = 1$ and $\mu = 2$ correspond to V-cycle and W-cycle, respectively. When the algorithm is used in preconditioning it is called with the approximate solution $\mathbf{x}_0$ being zero.

Algorithm 1. AMG initialization

Input: Matrix $\mathbf{B}_0$, initial graph G_0, the maximum size of the coarsest system n_c
1. $k = 0$
2. **Do while** the size of $\mathbf{B}_k$ is greater than n_c
3. Select the set of coarse nodes from the graph G_k
4. Form the restriction matrix $\mathbf{R}_k$
5. Create the graph G_{k+1}
6. Calculate the next system matrix $\mathbf{B}_{k+1} = \mathbf{R}_k\mathbf{B}_k\mathbf{R}_k^T$
7. Eliminate the rows and columns of $\mathbf{B}_k$ marked in the graph G_k
8. Eliminate the columns of $\mathbf{R}_k$ marked in the graph G_k
9. Eliminate the rows of $\mathbf{R}_k$ marked in the graph G_{k+1}
10. k=k+1
11. **End do**
12. Eliminate the rows and columns of $\mathbf{B}_k$ marked in the graph G_k
13. Factorize $\mathbf{B}_k$

Algorithm 2. Recursive algorithm for the AMG cycle

Input: Matrix $\mathbf{B}_l$, approximate solution $\mathbf{x}_l$, right-hand side vector $\mathbf{f}_l$
Output: Improved approximate solution $\mathbf{x}_l$
1. **If** on the coarsest level, that is, $l = k$
2. Solve $\mathbf{x}_l$ from $\mathbf{B}_l\mathbf{x}_l = \mathbf{f}_l$
3. **Else**
4. Presmooth $\mathbf{x}_l = \mathbf{x}_l + \mathbf{S}_l(\mathbf{x}_l,\mathbf{f}_l)$
5. Restrict the residual $\mathbf{f}_{l+1} = \mathbf{R}_l(\mathbf{f}_l - \mathbf{B}_l\mathbf{x}_l)$
6. Set $\mathbf{x}_{l+1} = 0$ and call μ times the cycle for the next level $l + 1$
7. Prolong the correction $\mathbf{x}_l = \mathbf{x}_l + \mathbf{R}_l^{\mathrm{T}}\mathbf{x}_{l+1}$
8. Post-smooth $\mathbf{x}_l = \mathbf{x}_l + \mathbf{S}_l(\mathbf{x}_l,\mathbf{f}_l)$
9. **End if**

5. Numerical results

5.1. Model problems with homogenous medium

We use two different model geometries with homogenous medium: the unit square and a cross-section of a car cabin. Fig. 2 shows typical solutions for these geometries. The same problem in the unit square was considered also in [14]. It has a point source at the middle and the absorbing boundary condition (5) is posed on all boundaries. The car cabin problem with a non-convex geometry resembles more real-world applications. The height of the car cabin is 1.5 m and its width is 3 m. The noise source is modeled using the Dirichlet boundary condition (3) with $g = 1$ on the wall behind pedals and on other boundaries the impedance boundary condition (4) with $\gamma = 0.2$ is used. The meshes for the car cabin problem were generated using Netgen [36] by refining a coarse mesh depicted in Fig. 1.

5.1.1. Eigenvalue study

We study the eigenvalues for both problems by computing both the full spectrum and Arnoldi approximations discussed in the end of Section 3. First we consider the Helmholtz problem with $k = 20$ in the unit square domain discretized on a 31×31 structured mesh. Figs. 3 and 4 demonstrate the influence of β_2, that is, the amount of damping to the spectrum of $\mathbf{AB}_{\mathrm{SL}}^{-1}$. We use the values $\beta_2 = 0.5$ and $\beta_2 = 1.0$. In these and all following results we have $\beta_1 = 1$. Fig. 3 shows that with the Neumann boundary condition the real parts of the eigenvalues are between zero and one with both β_2s, while the density of eigenvalues near zero is higher with $\beta_2 = 1.0$. The differences are more pronounced with the absorbing boundary condition. With a smaller β_2, the matrix $\mathbf{AB}_{\mathrm{SL}}^{-1}$ is closer to identity and this is seen as tighter clustering around

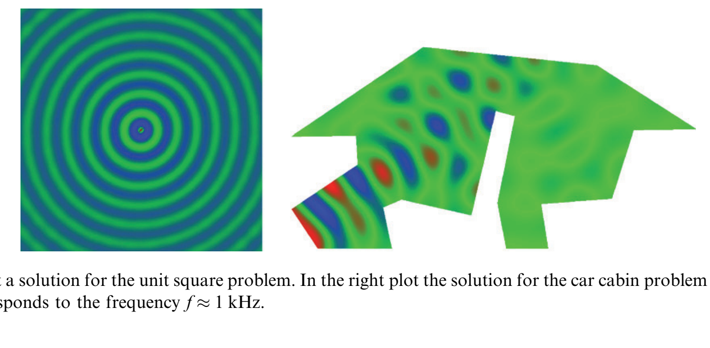

Fig. 2. In the left plot a solution for the unit square problem. In the right plot the solution for the car cabin problem with the wave number $k = 18.3$ which corresponds to the frequency $f \approx 1$ kHz.

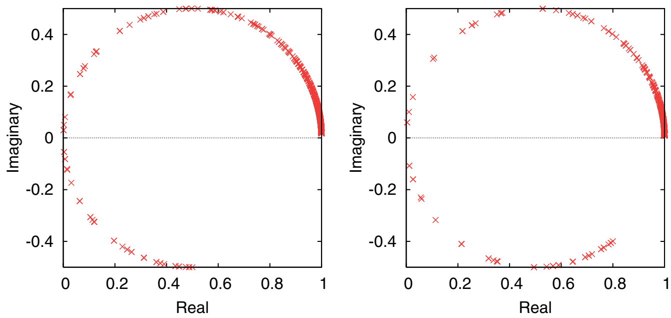

Fig. 3. The eigenvalues of $\mathbf{AB}_{\mathrm{SL}}^{-1}$ with $\beta_2 = 1.0$ in the left plot and $\beta_2 = 0.5$ in the right plot for the unit square with the Neumann boundary condition discretized using linear finite elements.

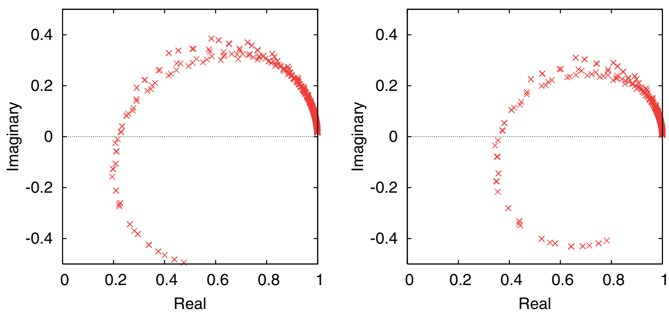

Fig. 4. The eigenvalues of $\mathbf{AB}_{\mathrm{SL}}^{-1}$ with $\beta_2 = 1.0$ in the left plot and $\beta_2 = 0.5$ in the right plot for the unit square with the absorbing boundary condition discretized using linear finite elements.

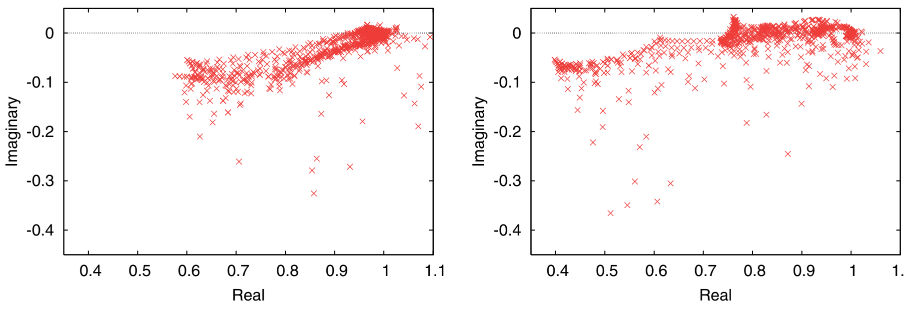

Fig. 5. The eigenvalues of $\mathbf{B}_{\mathrm{SL}}\mathbf{B}_{\mathrm{MG}}^{-1}$ for the unit square problem with the absorbing boundary condition. The left and right plots are computed using linear and quadratic elements, respectively.

one in Fig. 4. The spectrum of $\mathbf{AB}_{\mathrm{SL}}^{-1}$ is very similar with quadratic and cubic elements to one with linear elements shown in these figures.

Next we study the AMG approximations of the inverse of the discrete shifted-Laplacians. We consider the quality of these approximations and the influence of order of finite elements. For this, we use one W-cycle

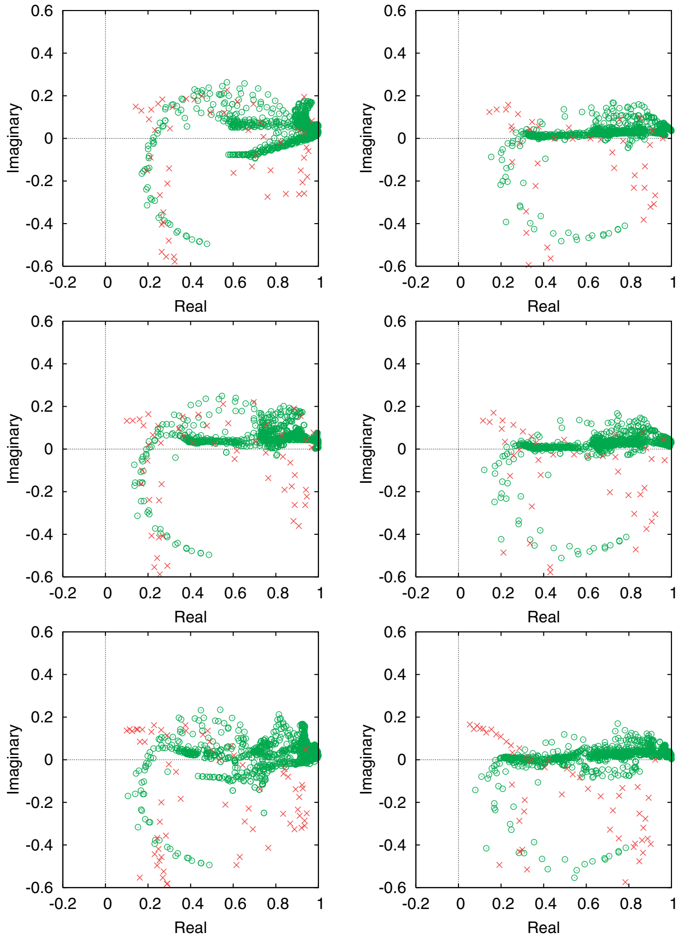

Fig. 6. For the unit square problem with the absorbing boundary conditions, the eigenvalues of $\mathbf{AB}_{\mathrm{MG}}^{-1}$ are marked with $\circ$ and their Arnoldi approximations with $\times$. The left and right plots are based on $\beta_2 = 1.0$ and $\beta_2 = 0.5$, respectively. The discretizations have been performed using linear (plots on the top), quadratic (plots in the middle), and cubic (plots on the bottom) finite elements.

based on one presmoothing and postsmoothing iteration performed by the underrelaxed Jacobi with the relaxation parameter chosen according to Table 2. Fig. 5 plots the spectrums of $\mathbf{B}_{\mathrm{SL}}\mathbf{B}_{\mathrm{MG}}^{-1}$ for linear and quadratic finite elements with $\beta_2 = 1.0$. With linear elements these eigenvalues are more clustered around one than with quadratic elements which indicates that the AMG approximation of the inverse is better with linear elements.

Fig. 6 depicts the eigenvalues of $\mathbf{AB}_{\mathrm{MG}}^{-1}$ with the absorbing boundary conditions for linear, quadratic and cubic finite elements when the parameter $\beta_2 = 0.5$ and 1.0. The eigenvalues are fairly similar for different elements and with $\beta_2 = 0.5$ some of them are closer to the real axis than with $\beta_2 = 1.0$. For the car cabin problem with $k = 15$, similar plots of eigenvalues are given in Fig. 7. The figures show that the spectrums are fairly similar for the unit square and car cabin problems. This suggest that the quality of the AMG preconditioner is not particularly sensitive to the geometry.

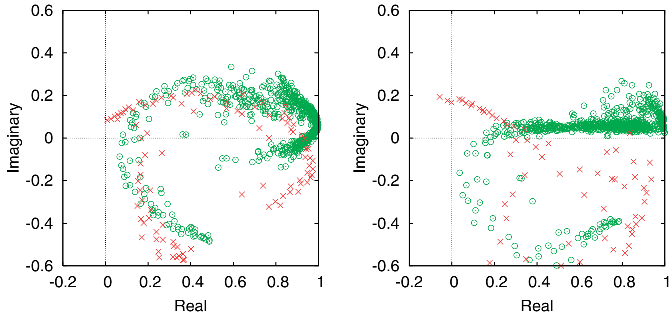

Fig. 7. For the car cabin problem discretized with linear elements the eigenvalues of $\mathbf{AB}_{\mathrm{MG}}^{-1}$ marked with $\circ$ and their Arnoldi approximations marked with $\times$. The left and right plots are based on $\beta_2 = 1.0$ and $\beta_2 = 0.5$, respectively.

5.1.2. Performance analysis

We mainly use the car cabin problem to study the performance of the iterative solver while we also report some results for the unit square problem. Fig. 2 shows usual time-harmonic scattering patterns for these problems. Table 1 describes the different meshes used with the car cabin problem.

The preconditioner $\mathbf{B}_{\mathrm{MG}}^{-1}$ is defined by one algebraic multigrid cycle described in Section 3. Our aim is to choose the parameters defining the preconditioner in such a way that the overall performance is optimal. We use the value $\beta_1 = 1$ while for β_2 we examine the values 0.5 and 1.0. There are several choices related to the AMG method. Our smoother is the underrelaxed Jacobi iteration with the relaxation parameter ω chosen according to Table 2. These relaxation parameters minimize the overall solution time in numerical tests. We use the W-cycle in the AMG method as it leads to shorter solution times than the V-cycle and F-cycle in experiments. The V-cycle led to five times and the F-cycle to slightly less than two times greater overall CPU consumption in our tests.

In Table 3, the number of iterations are reported for the unit square problem. We have chosen the wave numbers k and the mesh step sizes h to be the same as in [14]. With higher-order elements we could have used larger h without reducing accuracy. Their discretization was performed using a finite difference method and they employed a tuned geometric multigrid method instead of the AMG method used here. Furthermore, they used the BICGSTAB method with a slightly more strict stopping criterion. The number of iterations required here are higher. We need up to 1.5 times more iterations with $k = 40$ while the difference grows with k. Nevertheless the results in here and in [14] suggest that for higher frequencies the number of iterations roughly doubles when the frequency is doubled. The AMG preconditioner leads to particularly good results with cubic finite elements.

The convergence results for the car cabin problem are presented in Tables 4 and 5. In these tables, the wave number doubles from a row to the next and the mesh step size h is halved from a column to the next. Thus, the columns correspond to refined meshes in which the mesh step h is 2^{-n_r} times smaller than in the coarsest mesh. This leads to constant khs on diagonals. Along them, we can again observe that for higher frequencies the number of iterations roughly doubles when the wave number is doubled. The lower triangles of the tables cor-

Table 1
The number of elements and nodes in the car cabin meshes

	No. of refinements, n_r						
	0	1	2	3	4	5	6
Elements	82	328	1312	5248	20,992	83,962	335,872
Nodes, linear	62	205	737	2785	10,817	42,625	169,217
Nodes, quadratic	205	737	2785	10,817	42,625	169,217	674,305
Nodes, cubic	430	1597	6145	24,097	95,425	379,777	1,515,265

Table 2
The optimal choice of the Jacobi relaxation parameter ω for different finite elements and different values of β_2 found by extensive numerical experiments

β_2	ω		
	Linear	Quadratic	Cubic
0.5	0.4	0.4	0.4
1.0	0.8	0.7	0.7

Table 3
The number of iterations for the unit square problem for different element types when the iterations are terminated once the norm of the residual is reduced by the factor 10^{-6}

Element type	β_2	$k=40$	$k=50$	$k=80$	$k=100$	$k=150$
Linear	1.0	43	51	76	93	137
	0.5	37	47	82	111	210
Quadratic	1.0	44	53	79	97	140
	0.5	32	41	70	95	177
Cubic	1.0	45	56	83	103	149
	0.5	31	37	59	77	126

Table 4
For the car cabin problem discretized with linear elements, the number of GMRES iterations required to reduce the norm of the residual by the factor 10^{-6} as a function of the number of refinements n_r and the wave number k

k	$\beta_2=1.0$							$\beta_2=0.5$						
	$n_r=0$	$n_r=1$	$n_r=2$	$n_r=3$	$n_r=4$	$n_r=5$	$n_r=6$	$n_r=0$	$n_r=1$	$n_r=2$	$n_r=3$	$n_r=4$	$n_r=5$	$n_r=6$
2	**11**	11	11	11	11	10	10	**8**	12	13	13	13	12	12
4	19	**19**	18	18	17	16	15	13	**14**	15	15	15	14	14
8	32	35	**34**	34	34	32	30	20	25	**22**	21	21	21	20
16	40	84	65	**63**	65	64	59	32	58	52	**43**	35	34	35
32	8	125	184	130	**127**	133	127	7	144	172	124	**91**	75	73
64	4	9	366	409	264	**262**	270	4	13	433	408	279	**194**	148

Table 5
For the car cabin problem discretized with quadratic (left table) and cubic elements (right table), the number of GMRES iterations required to reduce the norm of the residual by the factor 10^{-6} as a function of the number of refinements n_r and the wave number k

k	Quadratic elements							Cubic elements						
	$n_r=0$	$n_r=1$	$n_r=2$	$n_r=3$	$n_r=4$	$n_r=5$	$n_r=6$	$n_r=0$	$n_r=1$	$n_r=2$	$n_r=3$	$n_r=4$	$n_r=5$	$n_r=6$
2	**12**	13	13	14	13	12	12	**16**	15	15	15	15	15	15
4	15	**15**	15	15	14	14	13	20	**17**	17	16	16	16	16
8	27	23	**21**	21	21	20	19	33	25	**23**	22	22	21	21
16	61	59	45	**35**	34	35	33	77	56	46	**37**	36	38	34
32	172	190	141	95	**75**	71	66	193	195	123	87	**70**	70	69
64	17	496	464	315	199	**148**	149	250	> 500	459	234	161	**149**	137

In both tables, $\beta_2=0.5$.

respond to discretizations which do not have sufficiently high number of nodes per wavelength to capture the oscillatory behavior of solutions. This shows up as unusually high number of iterations. Based on these results, the value $\beta_2=0.5$ leads to much faster convergence on higher wave numbers.

With a large number of iterations, the time spent in forming the basis vectors in the GMRES method takes a larger part of the CPU time. This effect is seen in Table 6 which reports the time spent in different parts of the

Table 6
The time spent in the solver with the car cabin problem discretized using quadratic elements on the $n_r = 5$ mesh

Wave number k	GMRES iterations	CPU time in seconds	% of time spent in AMG
2	10	8	93.9
8	29	23	87.4
32	126	129	64.6

The AMG uses W-cycle and $\beta_2 = 1.0$.

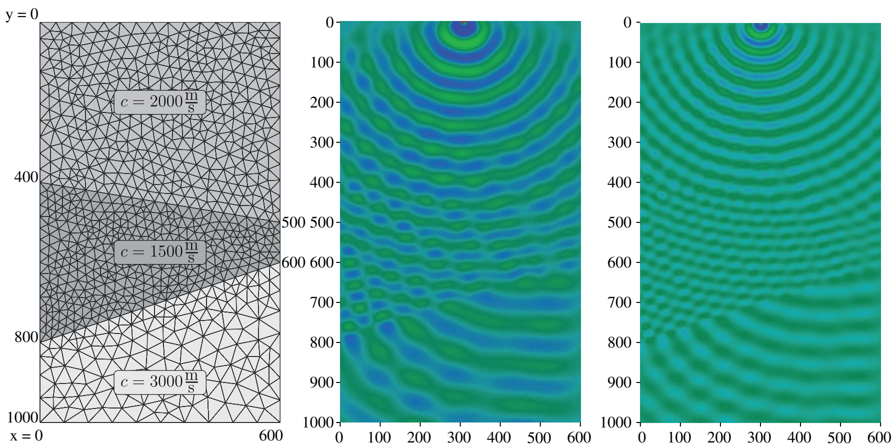

Fig. 8. The plot on the left shows the mesh for the frequency $f = 5$ Hz and the definition of the problem. On the middle and right the solutions for $f = 30$ Hz and $f = 50$ Hz, respectively, are shown.

Table 7
For the wedge problem the number of GMRES iterations required to reduce the norm of the residual by the factor 10^{-6} as a function of the frequency

Element type	$f = 5$ Hz	$f = 30$ Hz	$f = 50$ Hz
Linear, $\beta_2 = 1.0$	24	97	148
Linear, $\beta_2 = 0.5$	17	83	124
Cubic, $\beta_2 = 1.0$	24	105	171
Cubic, $\beta_2 = 0.5$	19	62	97

solver for three problems discretized using quadratic elements; linear and cubic elements lead to similar results. The computations were performed on a PC with an 1.2 GHz Intel Core Duo U2500 processor.

5.2. Wedge problem with inhomogenous medium

The wedge problem is defined by three layers with different speed of sound c in the rectangle $600 \times 1000\ \mathrm{m}^2$, as shown in Fig. 8. This model problem was considered in [14,19]. Meshes for different frequencies were constructed with Comsol Multiphysics mesh generator in such a way that the mesh step size h was approximately one tenth of one wavelength, that is, $h \approx \lambda/10$. The wedge model has a point source at the middle of the top boundary. The absorbing boundary condition (5) is posed on all boundaries. A coarse mesh for the frequency $f = 5$ Hz and the solutions for the frequencies $f = 30$ Hz and $f = 50$ Hz are shown in Fig. 8.

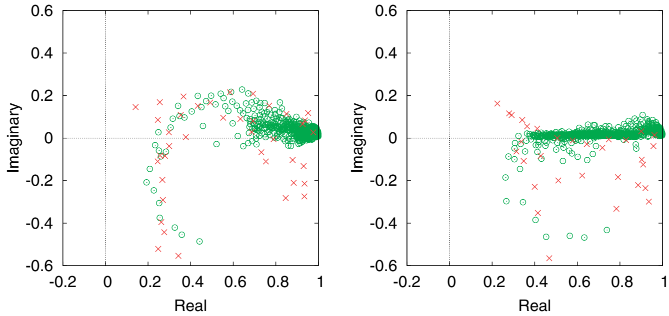

Fig. 9. The eigenvalues of $\mathbf{AB}_{\mathrm{MG}}^{-1}$ marked with ∘ and their Arnoldi approximations marked with × for the wedge problem with the frequency $f = 5$ Hz discretized using linear elements. The left and right plots are based on $\beta_2 = 1.0$ and $\beta_2 = 0.5$, respectively.

The performance results for different frequencies are presented in Table 7. According to these iteration counts, the convergence with $\beta_2 = 0.5$ is about 15% faster than with $\beta_2 = 1.0$ with linear elements and over 40% faster with cubic elements. We need again more iterations when compared to the results in [14], but our finite element discretizations have three advantages over the finite differences used in there: we can accurately model the interface between layers, we can use coarser meshes with higher-order elements, and we can use coarser mesh where the speed of sound is higher. Fig. 9 plots the eigenvalues of the preconditioned system for the low frequency $f = 5$ Hz with $\beta_2 = 1.0$ and $\beta_2 = 0.5$.

6. Conclusions

We have studied a preconditioner based on an algebraic multigrid (AMG) approximation of the inverse of a shifted-Laplacian for the Helmholtz equation. This is a generalization of the preconditioner proposed by Erlangga et al. in [14]. They used finite difference discretizations on rectangular domains and a geometrical multigrid. With our finite element discretizations and the AMG method we can solve problems in complicated domains and use higher-order finite elements. A big advantage of the AMG method is that the solver does not need hierarchical meshes nor operators discretized on different meshes. When the matrix for the zeroth-order term in a discretized Helmholtz equation or the mass matrix for a constant wave number problem is also available, the preconditioner can be constructed fully algebraically. Thus, in this case the preconditioned iteration can be seen as a ‘‘black box solver’’.

The numerical results demonstrated the capability to solve efficiently problems in complicated domains and varying wave numbers using the proposed preconditioner. Furthermore, the preconditioner was shown to be effective with linear, quadratic, and cubic finite elements. The proposed approach is especially well suited for low-frequency and mid-frequency problems while for high-frequency problems the number of iterations roughly doubles when the frequency is doubled. The same behavior was also observed in [14].

Acknowledgments

We thank Dr. Janne Martikainen for making his C++ FEM class library available to us and Prof. Tuomo Rossi for fruitful discussions. We also thank the referees for their comments which helped to improve the results and presentation. The research was supported by the Academy of Finland Grant #207089 and the US Office of Naval Research Grant N00014-06-1-0067.

References

[1] L.L. Thompson, A review of finite-element methods for time-harmonic acoustics, J. Acoust. Soc. Am. 119 (3) (2006) 1315–1330.
[2] F. Ihlenburg, Finite element analysis of acoustic scattering, Applied Mathematical Sciences, vol. 132, Springer-Verlag, New York, 1998.

[3] D.J. Nefske, J. Wolf, L. Howell, Structural-acoustic finite element analysis of the automobile passenger compartment: a review of current practice, J. Sound Vib. 80 (2) (1982) 247–266.

[4] B. Engquist, A. Majda, Absorbing boundary conditions for numerical simulation of waves, Math. Comput. 31 (1977) 629–651.

[5] Y. Saad, M.H. Schultz, GMRES: a generalized minimal residual algorithm for solving nonsymmetric linear systems, SIAM J. Sci. Statist. Comput. 7 (3) (1986) 856–869.

[6] H.A. van der Vorst, Bi-CGSTAB: a fast and smoothly converging variant of Bi-CG for the solution of nonsymmetric linear systems, SIAM J. Sci. Statist. Comput. 13 (2) (1992) 631–644.

[7] C. Farhat, A. Macedo, M. Lesoinne, F.-X. Roux, F. Magoulés, A. de La Bourdonnaie, Two-level domain decomposition methods with Lagrange multipliers for the fast iterative solution of acoustic scattering problems, Comput. Methods Appl. Mech. Eng. 184 (2–4) (2000) 213–239.

[8] C. Farhat, P. Avery, R. Tezaur, J. Li, FETI-DPH: a dual-primal domain decomposition method for acoustic scattering, J. Comput. Acoust. 13 (3) (2005) 499–524.

[9] M.J. Gander, F. Magoulès, F. Nataf, Optimized Schwarz methods without overlap for the Helmholtz equation, SIAM J. Sci. Comput. 24 (1) (2002) 38–60.

[10] K. Ito, J. Toivanen, A fast iterative solver for scattering by elastic objects in layered media, Appl. Numer. Math. 57 (5–7) (2007) 811–820.

[11] K. Otto, E. Larsson, Iterative solution of the Helmholtz equation by a second-order method, SIAM J. Matrix Anal. Appl. 21 (1) (1999) 209–229.

[12] A. Brandt, I. Livshits, Wave-ray multigrid method for standing wave equations, Electron. Trans. Numer. Anal. 6 (1997) 162–181.

[13] H.C. Elman, O.G. Ernst, D.P. O'Leary, A multigrid method enhanced by Krylov subspace iteration for discrete Helmholtz equations, SIAM J. Sci. Comput. 23 (4) (2001) 1291–1315.

[14] Y.A. Erlangga, C.W. Oosterlee, C. Vuik, A novel multigrid based preconditioner for heterogeneous Helmholtz problems, SIAM J. Sci. Comput. 27 (4) (2006) 1471–1492.

[15] O.G. Ernst, A finite-element capacitance matrix method for exterior Helmholtz problems, Numer. Math. 75 (2) (1996) 175–204.

[16] E. Heikkola, Y.A. Kuznetsov, P. Neittaanmäki, J. Toivanen, Fictitious domain methods for the numerical solution of two-dimensional scattering problems, J. Comput. Phys. 145 (1) (1998) 89–109.

[17] E. Heikkola, T. Rossi, J. Toivanen, A parallel fictitious domain method for the three-dimensional Helmholtz equation, SIAM J. Sci. Comput. 24 (5) (2003) 1567–1588.

[18] M.M. Monga Made, Incomplete factorization-based preconditionings for solving the Helmholtz equation, Int. J. Numer. Methods Eng. 50 (2001) 1077–1101.

[19] R.E. Plessix, W.A. Mulder, Separation-of-variables as a preconditioner for an iterative Helmholtz solver, Appl. Numer. Math. 44 (3) (2003) 385–400.

[20] M.O. Bristeau, R. Glowinski, J. Périaux, Controllability methods for the computation of time-periodic solutions; application to scattering, J. Comput. Phys. 147 (2) (1998) 265–292.

[21] E. Heikkola, S. Mönkölä, A. Pennanen, T. Rossi, Controllability method for acoustic scattering with spectral elements, J. Comput. Appl. Math. 204 (2) (2007) 344–355.

[22] E. Turkel, Numerical methods and nature, J. Sci. Comput. 28 (2–3) (2006) 549–570.

[23] A. Bayliss, C.I. Goldstein, E. Turkel, An iterative method for the Helmholtz equation, J. Comput. Phys. 49 (3) (1983) 443–457.

[24] A.L. Laird, M.B. Giles, Preconditioned iterative solution of the 2D Helmholtz equation, Tech. Rep. 02/12, Oxford Computer Laboratory, Oxford, UK, 2002.

[25] Y.A. Erlangga, C. Vuik, C.W. Oosterlee, On a class of preconditioners for solving the Helmholtz equation, Appl. Numer. Math. 50 (3–4) (2004) 409–425.

[26] E. Turkel, Y. Erlangga, Preconditioning a finite element solver of the exterior Helmholtz equation, in: P. Wesseling, E. Oñate, J. Périaux (Eds.), ECCOMAS CFD, ECCOMAS, 2006.

[27] Y. Erlangga, A preconditioner for the Helmholtz equation with perfectly matched layer, in: P. Wesseling, E. Oñate, J. Périaux (Eds.), ECCOMAS CFD, ECCOMAS, 2006.

[28] A. Bamberger, P. Joly, J.E. Roberts, Second-order absorbing boundary conditions for the wave equation: a solution for the corner problem, SIAM J. Numer. Anal. 27 (2) (1990) 323–352.

[29] A. Bayliss, M. Gunzburger, E. Turkel, Boundary conditions for the numerical solution of elliptic equations in exterior regions, SIAM J. Appl. Math. 42 (2) (1982) 430–451.

[30] I.M. Babuška, S.A. Sauter, Is the pollution effect of the FEM avoidable for the Helmholtz equation considering high wave numbers? SIAM J. Numer. Anal. 34 (6) (1997) 2392–2423.

[31] A. Bayliss, C.I. Goldstein, E. Turkel, On accuracy conditions for the numerical computation of waves, J. Comput. Phys. 59 (3) (1985) 396–404.

[32] Y. Saad, Iterative Methods for Sparse Linear Systems, second ed., Society for Industrial and Applied Mathematics (SIAM), Philadelphia, PA, 2003.

[33] W.L. Briggs, V.E. Henson, S.F. McCormick, A Multigrid Tutorial, second ed., Society for Industrial and Applied Mathematics (SIAM), Philadelphia, PA, 2000.

[34] F. Kickinger, Algebraic multi-grid for discrete elliptic second-order problems, in: Multigrid Methods V (Stuttgart, 1996), Springer, Berlin, 1998, pp. 157–172.

[35] J. Martikainen, A. Pennanen, T. Rossi, Application of an algebraic multigrid method to incompressible flow problems, Tech. Rep. B2/2006, Department of Mathematical Information Technology, University of Jyväskylä, Jyväskylä, Finland, 2006.

[36] J. Schöberl, NETGEN – an advancing front 2D/3D-mesh generator based on abstract rules, Comput. Visual. Sci. 1 (1997) 41–52.

II

A DAMPING PRECONDITIONER FOR TIME-HARMONIC WAVE EQUATIONS IN FLUID AND ELASTIC MATERIAL

by

Tuomas Airaksinen, Anssi Pennanen, Jari Toivanen

Journal of Computational Physics 228 (2009) 1466-1479

Journal of Computational Physics 228 (2009) 1466–1479

Contents lists available at ScienceDirect

Journal of Computational Physics

journal homepage: www.elsevier.com/locate/jcp

A damping preconditioner for time-harmonic wave equations in fluid and elastic material

Tuomas Airaksinen [a,*], Anssi Pennanen [a], Jari Toivanen [b]

[a] Department of Mathematical Information Technology, University of Jyväskylä, P.O. Box 35 (Agora), FI-40014, Finland
[b] Institute for Computational and Mathematical Engineering, Building 500, Stanford University, Stanford, CA 94305, USA

ARTICLE INFO

Article history:
Received 24 January 2008
Received in revised form 22 October 2008
Accepted 28 October 2008
Available online 12 November 2008

Keywords:
Helmholtz equation
Navier equation
Algebraic multigrid method
GMRES
Preconditioning
Finite element method

ABSTRACT

A physical damping is considered as a preconditioning technique for acoustic and elastic wave scattering. The earlier preconditioners for the Helmholtz equation are generalized for elastic materials and three-dimensional domains. An algebraic multigrid method is used in approximating the inverse of damped operators. Several numerical experiments demonstrate the behavior of the method in complicated two-dimensional and three-dimensional domains.

1. Introduction

Developing efficient methods to solve acoustic and elastic scattering problems has proved to be challenging by mathematical and computational means. These problems have a wide range of applications in different disciplines, and therefore there is a big interest to find efficient methods to solve these problems numerically. Modeling is done by acoustic or elastic wave equation, depending on the material, and it is often sufficient to consider only time-harmonic solutions. For incompressible fluids, the reduced wave equation is the Helmholtz equation. For linearly elastic material, the Navier equation can be applied. An approximate solution can be obtained by discretizing these equations using, for example, a finite difference or finite element method.

Finite element methods have become a popular technique to discretize partial differential equations in complex geometries. It has successfully been used for interior scattering problems like acoustic scattering in a car cabin [1] as well as for exterior problems. A review [2] gives an overview of recent research on finite element methods for acoustic problems. Since the paper [3] the research on the construction of absorbing boundary conditions and absorbing layers at the truncation boundary of the exterior domain has been active; see [2] and references therein. The size of the scattering problems is often limited in high-frequency problems because the methods become ineffective as the frequency grows. Particularly the finite element phase shift (pollution) error necessitates finer discretizations for high-frequency problems [4] and thus an increasing memory and computational requirements.

* Corresponding author. Tel.: +358 14 260 2743; fax: +358 14 260 2771.
E-mail address: tuomas.a.airaksinen@jyu.fi (T. Airaksinen).

0021-9991/$ - see front matter
doi:10.1016/j.jcp.2008.10.036

The resulting systems of linear equations from the discretization of the Helmholtz equation and the Navier equation are non-Hermitian and indefinite, and for mid-frequency and high-frequency problems, they can be extremely large. These properties make them a challenge for the current solvers. For two-dimensional problems, it is often feasible to use direct methods for solving these systems, but three-dimensional problems lead to systems that can not be solved by these methods with an affordable computing effort. Hence, it is necessary to use iterative methods such as the GMRES method [5] or the Bi-CGSTAB method [6]. However, these methods require a good preconditioner for the discretized equations in order to have reasonably fast convergence.

Several preconditioners and iterative solution techniques have been proposed for the discrete Helmholtz and Navier equations. Domain decomposition methods have been proposed for Helmholtz problems in [7–12], and for elastic problems in [13–16]. Controllability methods have been proposed for both Helmholtz and Navier problems in [17,18]. Multigrid methods have been considered for acoustic and elastic problems in [19–22]. With multigrid methods, it is difficult to define a stable and sufficiently accurate coarse grid problem and smoother for it. For acoustic and elastic problems in homogenous medium, domain imbedding/fictitious domain methods in [23–26] have been fairly effective, but these methods are pretty restrictive and not well-suited in general, complicated domains. An incomplete factorization preconditioner has been considered in [27], for example, and in [28] a tensor product preconditioner is used.

So called natural preconditioning techniques are applicable for many problems including time-harmonic wave equations [29]. The class of preconditioners based on damped operators that are considered here, is an example of this approach. A shifted-Laplacian preconditioner with a complex shift, which is called here a damped Helmholtz preconditioner, was first considered in [30] for the Helmholtz equation. This was a development over the shifted-Laplacian preconditioner with a real shift previously described in [31]. Already in [32,33] a complex shift was employed, but for a completely different way and purpose: it was used to transform a singular problem into a non singular one. Here the purpose to introduce a complex shift into a preconditioner for a non singular problem is to enable the effecient use of multigrid methods.

A damped Helmholtz preconditioner with geometric multigrid was considered in [21]. There, the scattering problems were posed in a rectangular domain and they were discretized using low-order finite differences. Our earlier study [34] extended this approach to general shaped two-dimensional domains using linear, quadratic, and cubic finite element discretizations by applying an algebraic multigrid (AMG) instead of the geometric multigrid to approximate the inversion of the damped Helmholtz operator. In [35], this method was compared with the previously mentioned controllability method.

In this paper, a generalization will be proposed to the preconditioner described in [34], an AMG-based damped preconditioner for time-harmonic wave propagation problems in elastic media, i.e. the Navier equation. This preconditioner will be called a damped Navier preconditioner. Results considering the eigenvalue spectrum of the shifted-Laplacian preconditioned discretized Helmholtz equation were given in [36] and some of these will be generalized to the Navier equation. Simulations are carried out in two-dimensional and three-dimensional computational domains including complicated geometries for both Helmholtz and Navier problems.

This paper is organized as follows. In Section 2 acoustic and elastic wave scattering models and their discretizations are described. The iterative solution and preconditioning are discussed in Section 3 and mathematical results on the eigenvalue spectrum are given in Section 4. The algebraic multigrid method employed in the preconditioning is described in Section 5. Then numerical results are presented in Section 6 and finally, conclusions are given in Section 7.

2. Mathematical formulation

2.1. Wave scattering in fluids

For a time-harmonic pressure of the form $p(\mathbf{x}, t) = \hat{p}(\mathbf{x})e^{-i\omega t}$ with an angular frequency ω and imaginary unit $i = \sqrt{-1}$, the wave scattering in a fluid domain Ω^f can be described by a Helmholtz equation

$$-\nabla \cdot \frac{1}{\rho}\nabla\hat{p} - \frac{k^2}{\rho}\hat{p} = f_f, \tag{1}$$

where $k(\mathbf{x}) = \omega/c(\mathbf{x})$ is the wave number, $f_f(\mathbf{x})$ is a time-harmonic sound source and $\rho(\mathbf{x})$ is fluid density. In inhomogeneous medium, the wave number k varies depending on location as the sound speed c varies. The boundary of the fluid domain Ω^f is decomposed into a Dirichlet boundary Γ^f_d and an impedance boundary Γ^f_i. The associated boundary conditions are given by

$$\hat{p} = g_f \quad \text{on } \Gamma^f_d \tag{2}$$

and

$$\frac{\partial\hat{p}}{\partial\mathbf{n}} = i\gamma k\hat{p} \quad \text{on } \Gamma^f_i, \tag{3}$$

where $g_f(\mathbf{x})$ describes a sound source and $\mathbf{n}(\mathbf{x})$ is the outer normal vector. Choosing the absorbency coefficient γ to be zero leads to the Neumann boundary condition and $\gamma = 1$ gives a low-order absorbing boundary condition.

2.2. Wave scattering in elastic materials

For time-harmonic displacements $\mathbf{u}(\mathbf{x},t) = e^{-i\omega t}\hat{\mathbf{u}}(\mathbf{x})$ in a domain Ω^s consisting of elastic materials, the scattering of time-harmonic waves can be described by a Navier equation

$$-\omega^2\rho_s\hat{\mathbf{u}} - \nabla\cdot\sigma(\hat{\mathbf{u}}) = \mathbf{f}_s, \tag{4}$$

where σ is the stress tensor, $\mathbf{f}_s$ is a force term, and $\rho_s(\mathbf{x})$ is the density of the material. Hooke's law gives a relation between displacements, and stress and strain forces, thus describing strain tensor ε and stress tensor σ:

$$\varepsilon(\mathbf{u}) = \frac{1}{2}(\nabla\mathbf{u} + (\nabla\mathbf{u})^T), \quad \sigma(\mathbf{u}) = \lambda(\nabla\cdot\mathbf{u}) + 2\mu\varepsilon(\mathbf{u}). \tag{5}$$

Here Lamè parameters λ and μ are defined as follows:

$$\lambda(\mathbf{x}) = \frac{E}{2(1+v)}, \quad \mu(\mathbf{x}) = \frac{Ev}{(1+v)(1-2v)}. \tag{6}$$

These depend on Young modulus $E(\mathbf{x})$ and the Poisson ratio $v(\mathbf{x})$ that characterize the elastic behavior of the material. The speed of pressure wave, c_p, and shear wave, c_s, can be expressed as functions of Lamé parameters:

$$c_p = \sqrt{\frac{\lambda+2\mu}{\rho_s}}, \quad c_s = \sqrt{\frac{\mu}{\rho_s}}. \tag{7}$$

Wavelengths and wave numbers for pressure and shear waves are

$$\lambda_{p,s} = c_{p,s}\frac{2\pi}{\omega}, \quad k_{p,s} = \frac{\omega}{c_{p,s}}. \tag{8}$$

For elastic material in the domain Ω^s, the following boundary conditions are applied: a Dirichlet boundary condition on Γ^s_d and an impedance boundary condition on Γ^s_i. As with the fluid domain, the boundary of elastic material $\Gamma^s = \partial\Omega^s$ is decomposed into two non-overlapping parts $\Gamma^s = \Gamma^s_d \cup \Gamma^s_i$ such that either boundary set can be empty. The Dirichlet boundary condition on Γ^s_d is described by

$$\hat{\mathbf{u}} = \mathbf{g}_s \quad \text{on } \Gamma^s_d, \tag{9}$$

where $\mathbf{g}_s(\mathbf{x})$ describes the vibration source. The impedance boundary condition on Γ^s_i is approximated by the equation

$$i\gamma\omega\rho_s\mathbf{B}\hat{\mathbf{u}} + \sigma(\hat{\mathbf{u}})\mathbf{n} = 0 \quad \text{on } \Gamma^s_i, \tag{10}$$

where γ is the absorbency coefficient, $i = \sqrt{-1}$, $\mathbf{B}$ is a 2×2 matrix for two-dimensional problems ($D = 2$) and a 3×3 matrix for three-dimensional problems ($D = 3$). Choosing the absorbency coefficient $\gamma = 0$ leads to natural boundary condition and $\gamma = 1$ gives an absorbing boundary condition. In component form $\mathbf{B}$ has expressions

$$\begin{aligned} &\mathbf{B}_{ij} = c_p n_i n_j + c_s t_i t_j, \quad \text{for } D = 2 \text{ and} \\ &\mathbf{B}_{ij} = c_p n_i n_j + c_s t_i t_j + c_s s_i s_j \quad \text{for } D = 3, \end{aligned} \tag{11}$$

where c_p and c_s are the speeds of pressure and shear waves given by (7) and $\mathbf{n} = (n_1, \ldots, n_D)^T$ is the normal vector pointing out of elastic domain, and $\mathbf{t} = (t_1, \ldots, t_D)^T$ and $\mathbf{s} = (s_1, \ldots, s_D)^T$ are tangential vectors on the boundary.

2.3. Weak formulation and finite element discretization

For the weak formulation of the Helmholtz equation, we define a test function space V^f_0 and a solution space V^f_g as

$$V^f_g = \{\hat{q} \in H^1(\Omega^f) : \hat{q} = g_f(\mathbf{x}) \text{ on } \Gamma^f_d\}. \tag{12}$$

The weak form of (1) reads: Find $\hat{p} \in V^f_g$ such that

$$\int_{\Omega^f} \frac{1}{\rho}(\nabla\hat{p}\cdot\nabla\bar{\hat{q}} - k^2\hat{p}\bar{\hat{q}})dx - \int_{\Gamma^f_i} \frac{1}{\rho}(i\gamma k\hat{p}\bar{\hat{q}})ds = \int_{\Omega^f} f_f\bar{\hat{q}}dx \tag{13}$$

for all $\hat{q} \in V^f_0$. Similarly, for the Navier equation, we define a test function space V^s_0 and a solution space V^s_g as

$$V^s_g = \{\hat{\mathbf{v}} \in [H^1(\Omega^s)]^D : \hat{\mathbf{v}} = \mathbf{g}_s(\mathbf{x}) \text{ on } \Gamma^s_d\}. \tag{14}$$

Now, the weak form of (4) reads: Find $\hat{\mathbf{u}} \in V^s_g$ such that

$$\int_{\Omega^s} (-\rho_s\omega^2\hat{\mathbf{u}}\cdot\bar{\hat{\mathbf{v}}} + \sigma(\hat{\mathbf{u}}) : \varepsilon(\bar{\hat{\mathbf{v}}}))dx - \int_{\Gamma^s_i} i\gamma\omega\rho_s\mathbf{B}\hat{\mathbf{u}}\cdot\bar{\hat{\mathbf{v}}}ds = \int_{\Omega^s} \mathbf{f}_s\cdot\bar{\hat{\mathbf{v}}}dx \tag{15}$$

for all $\hat{\mathbf{v}} \in V^s_0$.

For a finite element discretization, a mesh K_h is defined such that $\Omega_h = \bigcup_{\tau\in K_h}\tau$. The mesh consists of triangles τ in two-dimensional and of tetrahedra in three-dimensional problems. Here h denotes the diameter of the largest triangle or tetrahedron and $\Omega_h^{f,s}$ is an approximation of $\Omega^{f,s}$. For the finite elements of order m discrete test function spaces are

$$V_h^f = \{\hat{q} \in H^1(\Omega_h^f) : \hat{q}_h|_\tau \in P^m \forall \tau \in K_h : \hat{q} = 0 \text{ on } \Gamma_{d,h}^f\} \text{ and} \tag{16}$$

$$V_h^s = \{\hat{\mathbf{v}} \in [H^1(\Omega_h^s)]^D : \hat{\mathbf{v}}_h|_\tau \in [P^m]^D \forall \tau \in K_h : \hat{\mathbf{v}} = \mathbf{0} \text{ on } \Gamma_{d,h}^s\}, \tag{17}$$

where P^m denotes polynomials of order m. Discrete solution spaces $V_{g,h}^{f,s}$ are the same except the zero boundary value on $\Gamma_{d,h}^{f,s}$ is replaced by approximations of g_f and $\mathbf{g}_s$. In this paper, linear, quadratic, and cubic finite elements are employed, i.e. $m = 1, 2$, or 3. For the spaces V_h and $V_{g,h}$, Lagrangian polynomials are used as basis functions.

For the analytical study of eigenvalue spectra in Section 4, it is practical to define the following matrices based on the integrals in (13) and (15):

$$\begin{aligned}
&\mathbf{M}^f = \int_{\Omega_h^f} \frac{k^2}{\rho}\hat{p}_h\bar{\hat{q}}_h dx, \quad \mathbf{M}^s = \int_{\Omega_h^s} \rho_s\omega^2\hat{\mathbf{u}}_h\cdot\bar{\hat{\mathbf{v}}}_h dx,\\
&\mathbf{L}^f = \int_{\Omega_h^f} \frac{1}{\rho}\nabla\hat{p}_h\cdot\nabla\bar{\hat{q}}_h dx, \quad \mathbf{L}^s = \int_{\Omega_h^s} \sigma(\hat{\mathbf{u}}_h) : \varepsilon(\bar{\hat{\mathbf{v}}}_h) dx,\\
&\mathbf{C}^f = -\int_{\Gamma_{i,h}^f} \frac{1}{\rho}(\gamma k\hat{p}_h\bar{\hat{q}}_h) ds, \quad \mathbf{C}^s = -\int_{\Gamma_{i,h}^s} \gamma\omega\rho_s\mathbf{B}_s\hat{\mathbf{u}}_h\cdot\bar{\hat{\mathbf{v}}}_h ds,
\end{aligned} \tag{18}$$

where $\hat{p}_h \in V_{g,h}^f, \hat{\mathbf{u}}_h \in V_{g,h}^s, \hat{q}_h \in V_h^f$, and $\hat{\mathbf{v}}_h \in V_h^s$. Furthermore, let $z_1 = \alpha_1 + \beta_1 i$. Similarly to [36], the discretized Helmholtz and Navier operators have matrix forms

$$\mathbf{F} = \mathbf{L}^f + i\mathbf{C}^f - z_1\mathbf{M}^f \quad \text{and} \quad \mathbf{S} = z_1\mathbf{L}^s + \sqrt{z_1}i\mathbf{C}^s - \mathbf{M}^s, \tag{19}$$

respectively.

Now, let the vector $\mathbf{w}$ contain the nodal values of $\hat{p}$ or $\hat{\mathbf{u}}$, so that for the Helmholtz problem it has form $\mathbf{w} = [\hat{p}_1, \ldots, \hat{p}_n]^T$, and for the two-dimensional Navier problem it has form $\mathbf{w} = [\hat{u}_1^x, \hat{u}_1^y, \ldots, \hat{u}_m^x, \hat{u}_m^y]^T$.

By replacing the spaces, domains, and boundaries in (13) or (15) by their discrete counterparts, the system of linear equations

$$\mathbf{A}\mathbf{w} = \mathbf{f} \tag{20}$$

is obtained. The complex-value sparse matrix $\mathbf{A}$ is given by $\mathbf{F}$ or $\mathbf{S}$ in (18) and $\mathbf{f}$ is a vector resulting from an inhomogeneous Dirichlet boundary value and/or a non-zero f_f in (13) or $\mathbf{f}_s$ in (15).

The approximation properties of such finite element discretizations for the Helmholtz equation have been studied in [4]. Due to the pollution (phase shift) error, a non-optimal L^2 error estimate

$$e_h = \|u_h - u\| \leqslant C_1 k(kh)^{2m} + C_2(kh)^m \tag{21}$$

is obtained, where C_1 and C_2 are constants. Based on this estimate, larger mesh step sizes can be used when higher order finite elements are being used, in order to reach the same accuracy level.

3. Iterative solution and damped preconditioner

The matrix $\mathbf{A}$ in (20) is indefinite and symmetric, but not Hermitian. For example, the generalized minimal residual (GMRES) method [5] and the Bi-CGSTAB method [6] are suitable iterative methods for these equations. These and other applicable iterative methods are described in [37]. The GMRES method minimizes the 2-norm of the residual on Krylov subspaces. This is a desirable property leading to a monotonic reduction of the norm of the residual over iterations, but a disadvantage is that all basis vectors for the Krylov subspace needs to be stored. This makes the computational cost of the GMRES methods grow quadratically with iterations and also causes linear growth in memory requirement. The computational cost of the Bi-CGSTAB method grows linearly with the iterations and the memory requirement is constant, but the convergence can be erratic and slower than with the GMRES method. In the numerical experiments, the full GMRES method is used without restarts.

The convergence of Krylov subspace methods for the system (20) is very slow for medium- and large-scale scattering problems due to the ill conditioning of $\mathbf{A}$. To improve the conditioning and the speed of convergence, a right preconditioner denoted by $\mathbf{B}$ is introduced. This leads to a preconditioned system

$$\mathbf{A}\mathbf{B}^{-1}\tilde{\mathbf{u}} = \mathbf{f}. \tag{22}$$

Once $\tilde{\mathbf{u}}$ is solved from this system, the solution $\mathbf{u}$ is obtained as $\mathbf{u} = \mathbf{B}^{-1}\tilde{\mathbf{u}}$. The goal is to find such a preconditioner $\mathbf{B}$ that the matrix $\mathbf{A}\mathbf{B}^{-1}$ is well conditioned and that vectors can be multiplied by $\mathbf{B}^{-1}$, i.e. solve systems with $\mathbf{B}$ with a small computational effort. These properties would lead to a fast convergence of the iterative method and to a small overall computational cost.

A shifted-Laplacian

$$\mathscr{F}_d = -\nabla \cdot \frac{1}{\rho}\nabla - z_2\frac{k^2}{\rho}, \tag{23}$$

with a complex shift $z_2 = \alpha_2 + \beta_2 i$ was suggested in [30] as a preconditioner for the Helmholtz equation. By choosing $\alpha_2 = 1$ and β_2 to be negative, $\mathscr{F}_d$ is the Helmholtz operator in (1) with some additional damping. Using the matrices defined in (18), the discretization of $\mathscr{F}_d$ leads to a matrix

$$\mathbf{F}_d = \mathbf{L}^f + i\mathbf{C}^f - z_2\mathbf{M}^f. \tag{24}$$

With sufficient damping, systems with $\mathbf{F}_d$ can be solved much more easily than with $\mathbf{F}$ and the conditioning of $\mathbf{F}\mathbf{F}_d^{-1}$ can still be good. The use of different approximations for $\mathbf{F}_d^{-1}$ have been studied in [30,21,38,34]. Here an algebraic multigrid approximation described in Section 5 is considered.

Our hypothesis is that a similar physical damping can be employed to construct an efficient preconditioner for the Navier equations. Damping in elastic materials can be modelled by using a complex Young modulus. Multiplying the original Young modulus $E(x)$ by a complex z_2 leads to a preconditioning operator

$$\mathscr{S}_d = -\omega^2\rho_s\hat{\mathbf{u}} - z_2\nabla \cdot \sigma(\hat{\mathbf{u}}). \tag{25}$$

The coefficient z_2 appears also in the impedance boundary condition (10) as follows

$$i\gamma\omega\rho_s\sqrt{z_2}\mathbf{B}\hat{\mathbf{u}} + z_2\sigma(\hat{\mathbf{u}})\mathbf{n}_s = 0 \quad \text{on } \Gamma_i^s. \tag{26}$$

Using the matrices in (18), the discretization of $\mathscr{S}_d$ leads to the damped Navier preconditioner

$$\mathbf{S}_d = z_2\mathbf{L}^s + \sqrt{z_2}i\mathbf{C}^s - \mathbf{M}^s. \tag{27}$$

4. Spectral analysis for the preconditioned Navier equation

Studying the eigenvalue spectrum of the preconditioned matrix $\mathbf{AB}^{-1}$ is an usual way to estimate the convergence of an iterative method like GMRES. In [36], Theorems 3.1–3.6 give useful information of the eigenvalue spectrum of the preconditioned Helmholtz operator. Some of these results can be generalized to the Navier equation, as will be shown in the following.

As defined in (19), the matrix of the discretized Navier equation is

$$\mathbf{S} = z_1\mathbf{L}^s + \sqrt{z_1}i\mathbf{C}^s - \mathbf{M}^s. \tag{28}$$

Here matrices $\mathbf{L}^s$ and $\mathbf{C}^s$ are symmetric positive semi-definite and $\mathbf{M}^s$ is symmetric positive definite, and z_1 is a complex number. The case that there are only natural and/or Dirichlet boundary conditions, i.e. $\mathbf{C}^s = 0$, and the material is not absorbing, is analyzed first. Thus, the matrix $\mathbf{S}$ simplifies to

$$\mathbf{S} = z_1\mathbf{L}^s - \mathbf{M}^s. \tag{29}$$

The eigenvalue problem $\mathbf{AB}^{-1}\tilde{\boldsymbol{y}} = \tau\tilde{\boldsymbol{y}}$ is equivalent to

$$\mathbf{A}\boldsymbol{y} = (z_1\mathbf{L}^s - \mathbf{M}^s)\boldsymbol{y} = \tau(z_2\mathbf{L}^s - \mathbf{M}^s)\boldsymbol{y} = \tau\mathbf{B}\boldsymbol{y}, \tag{30}$$

where $\boldsymbol{y} = \mathbf{B}^{-1}\tilde{\boldsymbol{y}}$. From this, the eigenvalue problem

$$\mathbf{L}^s\boldsymbol{y} = \lambda\mathbf{M}^s\boldsymbol{y}, \quad \lambda = \frac{1-\tau}{z_1 - \tau z_2} \tag{31}$$

can be derived.

As the matrix $\mathbf{L}^s$ is positive semi-definite and $\mathbf{M}^s$ is symmetric positive definite, the eigenvalues λ are real. The eigenvalue τ is a function of λ given by

$$\tau = \frac{z_1}{z_2}\frac{\lambda - z_1^{-1}}{\lambda - z_2^{-1}}. \tag{32}$$

By the change of variable $\lambda' = \lambda^{-1}$, the form

$$\tau = \frac{z_1 - \lambda'}{z_2 - \lambda'} \tag{33}$$

is obtained. This is the same equation of a circle in the complex plane that was found in [36] for the eigenvalue spectrum of the preconditioned Helmholtz equation. Due to this, the following corollary of Theorems 3.1–3.3 in [36] can be formulated.

Corollary 1. *For the eigenvalues $\tau = \tau^r + i\tau^i$ of the generalized eigenvalue problem $\mathbf{S}\boldsymbol{y} = \tau\mathbf{S}_d\boldsymbol{y}$, the following statements hold:*

- If $\beta_2 = 0$, the eigenvalues are located on straight line in the complex plane given by the equation

$$-\beta_1\tau^r + (\alpha_1 - \alpha_2)\tau^i + \beta_1 = 0. \tag{34}$$

- If $\beta_2 \neq 0$, the eigenvalues are located in complex plane on the circle given by

$$\left(\tau^r - \frac{\beta_2 + \beta_1}{2\beta_2}\right)^2 + \left(\tau^i - \frac{\alpha_2 - \alpha_1}{2\beta_2}\right)^2 = \frac{(\beta_2 - \beta_1)^2 + (\alpha_2 - \alpha_1)^2}{(2\beta_2)^2}. \tag{35}$$

The center of the circle is at $c = \frac{z_1 - \overline{z_2}}{z_2 - \overline{z_2}}$ and the radius is $R = |\frac{z_2 - z_1}{z_2 - \overline{z_2}}|$, where $z_{1,2} = \alpha_{1,2} + \beta_{1,2}i$.

- If $\beta_1\beta_2 > 0$, the origin is not enclosed by the circle defined by (35).

The case of impedance boundary conditions with $\gamma \neq 0$ in (10), i.e. $\mathbf{C}^s \neq 0$, is considered next. It is not evident that the results presented in [36] for the Helmholtz equation with $\mathbf{C}^f \neq 0$ are applicable for the Navier equation. However, numerical experiments in Section 6 suggest that similar behavior to the one described by Theorems 3.4–3.6 in [36] holds also here. The following states this as a conjecture.

Conjecture 2. *For the eigenvalues $\tau = \tau^r + i\tau^i$ of the generalized eigenvalue problem $\mathbf{S}\boldsymbol{y} = \tau\mathbf{S}_d\boldsymbol{y}$, the following statements hold:*

- If $\beta_2 = 0$, the eigenvalues are located in the half-plane

$$-\beta_1\tau^r + (\alpha_1 - \alpha_2)\tau^i + \beta_1 \geqslant 0. \tag{36}$$

- If $\beta_2 > 0$ the eigenvalues are inside or on the circle with the center at $c = \frac{z_1 - \overline{z_2}}{z_2 - \overline{z_2}}$ and the radius $R = \left|\frac{z_2 - z_1}{z_2 - \overline{z_2}}\right|$. If $\beta_2 < 0$, the eigenvalues are outside or on the same circle.

5. Algebraic multigrid based damped preconditioners

The approximation of the inverse of the damped operator $\mathbf{B}^{-1}$ given by a multigrid method is denoted by $\mathbf{B}_{MG}^{-1}$. In [21], Erlangga, Oosterlee, and Vuik used one cycle of a geometric multigrid method for this. For low-frequency problems the conditioning of $\mathbf{AB}_{MG}^{-1}$ is good. For high-frequency problems the conditioning deteriorates so that the number of Bi-CGSTAB iterations appeares to grow linearly with frequency in [21]. They also showed that this preconditioner is well-suited for problems with a varying speed of sound. In [34], the geometric multigrid method was replaced by a more generic and more flexible algebraic multigrid method (AMG). In this paper, an AMG-based on [39] is utilized, using the implementation that is described in [34], with modifications that make it suitable for vector valued problems, like the Navier equation.

The employed AMG method uses a graph to construct coarse spaces. Here the graph is based on the discretization mesh. Alternative approach would be to build the graph based on the matrix $\mathbf{B}$. When using linear elements in a scalar problem, both approaches result in the same graph. For an elastic solid modelled by the Navier equation, the graph is formed without connections (edges) between displacement components. This choice is made for two reasons: Adding these connections would cause too rapid coarsening process. Secondly, the error behaves smoothly for each component separately and the AMG method is especially efficient at reducing smooth error components. The graph therefore consists of separate disconnected graphs, one for each displacement component.

For linear finite elements, the initial graph G_0 is the graph defined by the triangulation. For quadratic and cubic elements, the graph is defined by a refined mesh. In two-dimensional domains, quadratic triangle elements are divided into four triangles by connecting the midpoints of the edges, and cubic triangle elements are divided into nine triangles. In three-dimensional domains, quadratic tetrahedron elements are divided into eight and cubic tetrahedra into 26 tetrahedra. If the graph defined by $\mathbf{B}$ was used directly with high-order elements, the coarsening procedure would coarsen the graph too rapidly, leading to an impaired conditioning of $\mathbf{AB}_{MG}^{-1}$ and a slower convergence of the GMRES method.

The nodes onto a coarser graph G_{k+1} are chosen from the nodes of G_k as follows. Find the node in G_k which has the smallest degree, i.e. the smallest number of edges associated to it. If there are several such nodes, choose the first one according to the node numbering. This node is included onto the graph G_{k+1}. Eliminate this node and all its neighbors from the graph G_k. Repeat this procedure until there are no nodes left in G_k. After choosing the nodes on G_{k+1}, they are numbered following their order in the numbering of the nodes on G_k.

On coarse levels, different displacement components are chosen to be disconnected. Thus, the restriction matrix is defined blockwise as

$$\mathbf{R}_k = \begin{bmatrix} \mathbf{R}_k^1 & & 0 \\ & \ddots & \\ 0 & & \mathbf{R}_k^p \end{bmatrix}. \tag{37}$$

The elements of the diagonal blocks of the restriction matrix are defined by the rule

$$(\mathbf{R}_k^l)_{ij} = \begin{cases} 1 & \text{for a fine node } j \text{ which is a coarse node } i, \\ \frac{1}{n} & \text{for a fine node } j \text{ which is a neighbor of coarse node } i \text{ and has } n \text{ neighboring coarse nodes}, \\ 0 & \text{otherwise}, \end{cases}$$

where fine and coarse refers to the graphs G_k and G_{k+1}, respectively. The edges of the coarse graph G_{k+1} are formed using the restriction matrix $\mathbf{R}_k$. Each coarse graph node corresponds to a row in the restriction matrix. There is an edge between two nodes if and only if the corresponding rows of the restriction matrix have a non-zero element in the same column.

The coarse level matrices are now defined as follows

$$\mathbf{B}_{k+1} = \mathbf{R}_k\mathbf{B}_k(\mathbf{R}_k)^T, \text{ where } \mathbf{B}_k = \begin{bmatrix} \mathbf{B}_k^{11} & \cdots & \mathbf{B}_k^{1D} \\ \vdots & \ddots & \vdots \\ \mathbf{B}_k^{D1} & \cdots & \mathbf{B}_k^{DD} \end{bmatrix}. \tag{38}$$

The usual multigrid W-cycle is used with the AMG method. For preconditioning, the initial approximate solution is zero in the multigrid algorithm.

At each level, presmoothing and postsmoothing is performed by one underrelaxed Jacobi iteration. At the coarsest level, a direct solver is used instead of an iterative method.

6. Numerical results

Numerical simulations were carried out on selected example problems. In Subsection 6.1, the eigenvalues of two-dimensional Navier problems are studied and compared with the results presented in Section 4. In Subsection 6.2, the performance of the method is considered for two-dimensional and three-dimensional Helmholtz and Navier problems by measuring iteration counts required to satisfy a convergence criterion.

The following material parameters are used in tests unless specified otherwise. The Helmholtz problems have domain Ω^f consisting of air, with the density $\rho_f = 1.2$ kg/m^3 and the speed of sound $c = 344$ m/s. The Navier problems are posed in a domain Ω^s consisting of aluminum with the density $\rho_s = 2700$ kg/m^3, Young modulus $E = 7.00 \times 10^{10}$ Pa, and Poisson ratio $\nu = 0.33$. Meshes were generated using Comsol Multiphysics 3.3 in such a way that the maximum element size is $h = \lambda/10$,

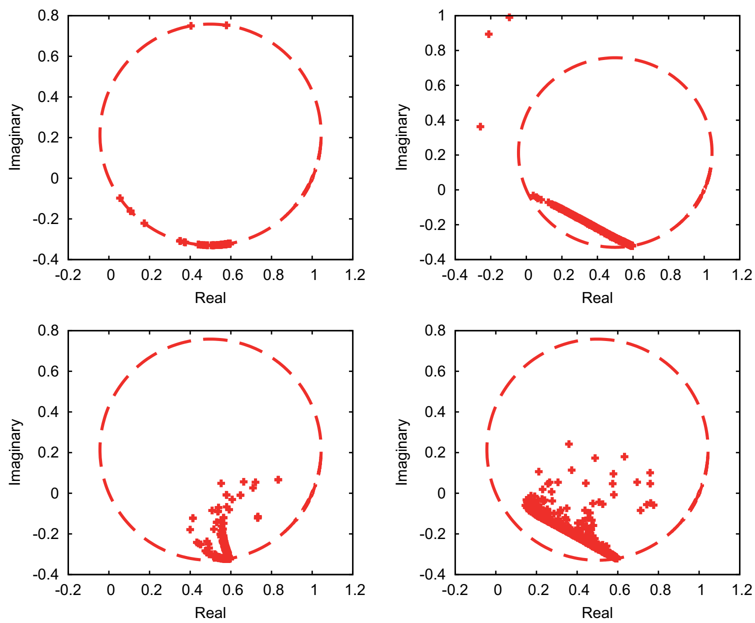

Fig. 1. Eigenvalue plots for the Navier problem in the unit square. The upper plots are for Dirichlet boundary value problems and on the lower plots, the absorbing boundary conditions are posed. On the left plots, the eigenvalues of $\mathbf{AB}^{-1}$ are shown. On the right plots, the eigenvalues of $\mathbf{AB}_{MG}^{-1}$ are shown. The circle is defined by (35). The damping parameters are $z_1 = 1.0$ and $z_2 = 1.3 + 0.7i$.

where λ is the wavelength of slowest wave mode. In the Helmholtz problems, λ is the length of acoustic waves, and in the Navier problems, it is the length of shear waves.

6.1. Eigenvalues

In [34], the eigenvalue spectra of the preconditioned system matrices were examined for several two-dimensional Helmholtz example problems. Here the eigenvalue spectra will be studied, when the system is preconditioned by a damped preconditioner for two-dimensional and three-dimensional Helmholtz and Navier problems. Two-dimensional problems are studied in the unit square domain like in [21,34] for the Helmholtz problem. A three-dimensional cube domain will also be considered for both Helmholtz and Navier problems. Estimates for the eigenvalue spectra of the preconditioned Navier equation, when Dirichlet or absorbing boundary conditions are posed on boundaries were presented in Section 4. These estimates will be compared to the numerically obtained eigenvalues.

First, the unit square problem will be considered for the Navier equation. The frequency 2.2 kHz is used in the eigenvalue study. The eigenvalues of $\mathbf{AB}^{-1}$ for the unit square problem with the Dirichlet and absorbing boundary conditions are presented in Fig. 1. Also the eigenvalues of $\mathbf{AB}_{MG}^{-1}$ are plotted for the same problem, where $\mathbf{B}_{MG}^{-1}$ is the algebraic multigrid approximation of $\mathbf{B}^{-1}$. The eigenvalue spectrum for the Navier problem with Dirichlet boundary conditions is distributed exactly on the circle as (35) describes. It is also seen that the algebraic multigrid does not spread the spectrum much. Most of eigenvalues seem to move slightly closer to the center of the circle.

For the eigenvalue spectra of the problems with the absorbing boundary conditions, it will be shown that the inequality (36) holds in numerical examples. Similar inequality was proven in [36] to hold for Helmholtz problems. According to the inequality (36), the eigenvalues should lie inside or outside of the circle depending on the sign of β_2. For better conditioning, β_2 is always chosen positive. Thus, according to (36), the eigenvalues should lie inside the circle. For the unit square problem with the absorbing boundary conditions, the conjecture seems to be valid, as can be seen in Fig. 1. The algebraic multigrid approximation changes the spectrum, but the eigenvalues seem to still lie inside the circle.

For three-dimensional experiments, the cube $(0.3\ \mathrm{m})^3$ is discretized by using linear finite elements for both Helmholtz and Navier problems. For the Navier problem, the frequency f is 5 kHz and for the Helmholtz problem, the frequency f is 500 Hz. In Fig. 2, the eigenvalues of $\mathbf{AB}^{-1}$ are plotted and in Fig. 3, the eigenvalues of the system with the AMG approximation of the inverse of the damped operator, $\mathbf{AB}_{MG}^{-1}$, are plotted. Also the circle (35) is drawn in these figures. It is clearly seen in Fig. 2, that both Corollary 1 and Conjecture 2 holds for this problem.

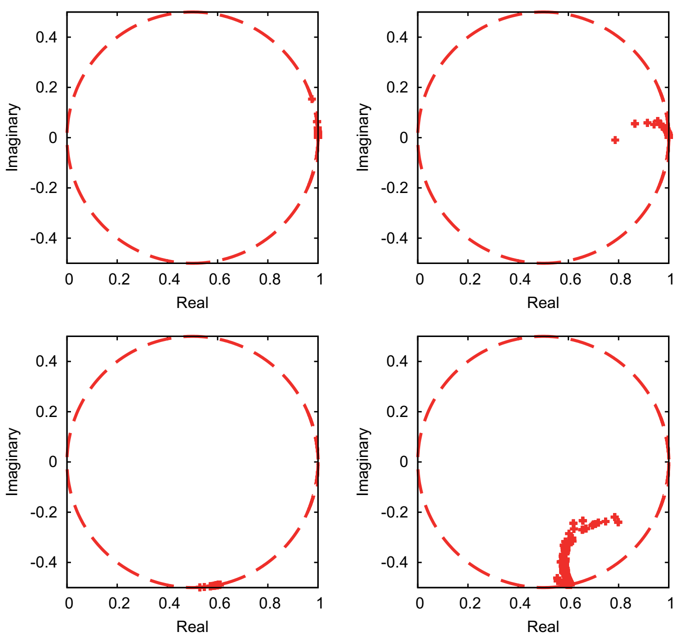

Fig. 2. The eigenvalues of $\mathbf{AB}^{-1}$. The upper plots are for the Helmholtz problems and the lower ones are for the Navier problems. The left plots are for the Dirichlet boundary value problems and the right ones are for problems with absorbing boundary conditions. The damping parameters are $z_1 = 1.0$ and $z_2 = 1.0 + 0.5i$ for the Helmholtz problems, and they are $z_1 = 1.0$ and $z_2 = 1.0 + 0.8i$ for the Navier problems.

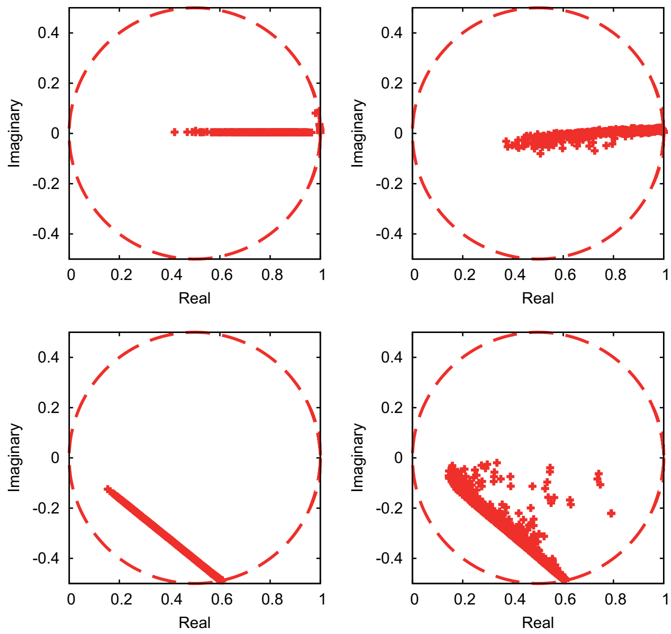

Fig. 3. The eigenvalues of $\mathbf{AB}_{MG}^{-1}$. The upper plots are for the Helmholtz problems and the lower ones are for the Navier problems. The left plots are for the Dirichlet boundary value problems and the right ones are for problems with absorbing boundary conditions. The damping parameters are $z_1 = 1.0$ and $z_2 = 1.0 + 0.5i$ for the Helmholtz problems, and they are $z_1 = 1.0$ and $z_2 = 1.0 + 0.8i$ for the Navier problems.

6.2. Performance of the preconditioner

The performance of the damped preconditioner with the algebraic multigrid will be reported for several different test problems. First, a two-dimensional Navier problem is studied in the unit square and three-dimensional Helmholtz and Navier problems are studied in a cube domain. Then, the method is tested on complicated three-dimensional problems: For the Helmholtz equation, a three-dimensional car cabin domain and a layered wedge domain with a varying speed of sound are considered. For the Navier equation, a crankshaft geometry defined by a Comsol Multiphysics 3.3 example problem is considered. The iteration counts give the number of iterations needed to reduce the relative residual to 10^{-6}.

In all performance studies with the unit square problems, the absorbing boundary condition given by (10) with $\gamma = 1$ was posed on the boundaries. For the Navier equation, the best value for β_2 was determined as follows. With several different frequencies and test problems, solutions were computed using the values $0.1, 0.2, \ldots, 1.0$. The value $\beta_2 = 0.8$ was selected as it gave the best convergence among the values which lead to a reliable preconditioner. The value appeared to be rather problem independent within the selected test problems and frequencies. The Jacobi relaxation parameter $\omega = 0.5$ was determined similarly. For the Helmholtz equation, the parameter values $\beta_2 = 0.5$ and $\omega = 0.5$ given in [34] were used, unless specified otherwise. The same parameter values were used for all element types.

6.2.1. Unit square

The first benchmark for the Navier equation is performed in the unit square domain with a point source in the middle. The solution was obtained at five different frequencies given in Table 1. The Navier equation was solved with linear and quadratic finite element discretizations. In Fig. 4, the solution is shown for the four lowest frequencies.

6.2.2. Cube problem

The Helmholtz and Navier problems were solved in the cube $(0.3\ \ \mathrm{m})^3$ with a point source in the middle. The performance of the damped preconditioner was compared to a modified incomplete Cholesky factorization (MIC) preconditioner [27]. The algorithm presented in [40] is used for the MIC(l) approximation of A^{-1}, where the parameter l describes the level of fill-in in the factorization. The values $l = 0$ and 1 have been used as bigger ls were uncompetitive as forming incomplete factorization required much more computation. The performance was measured by the number of GMRES iterations and the total number of floating point operations (FLOPs) required by the preconditioning. The number of FLOPs is a good measure, as it includes the initialization process in addition to GMRES iteration. The results are presented in Tables 2 and 3.

Table 1
The results for the unit square elasticity problem. Iteration counts are given for linear and quadratic finite elements.

f (kHz)	Element order	
	1	2
4.9	26	21
9.8	40	30
19.6	92	60
39.2	213	141
78.4	417	415

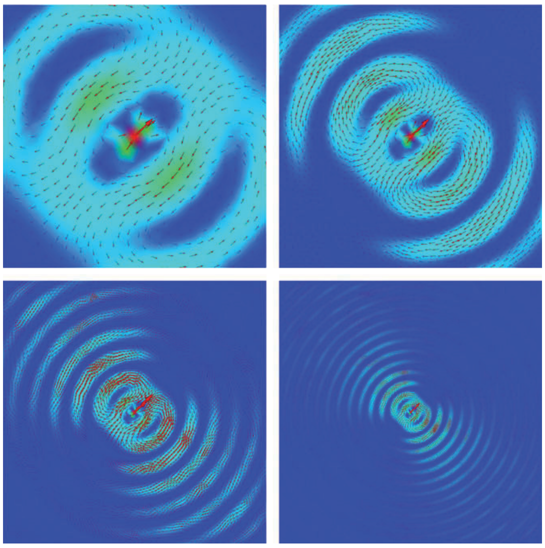

Fig. 4. The solution of the unit square elasticity problem at frequencies 4.9 kHz, 9.8 kHz, 19.6 kHz, and 39.2 kHz. The absorbing boundary conditions are posed on the boundaries.

Table 2
The iteration counts for the cube problem for the Helmholtz and Navier equations. Some counts are missing as the computations were too demanding.

Helmholtz

f (kHz)↓	AMG			MIC(0)		MIC(1)	
Order→	1	2	3	1	2	1	2
0.5	10	13	16	13	17	8	11
1.0	12	15	18	18	41	11	17
2.0	19	21	24	31	126	16	28
4.0	35	42	55	50		29	

Navier

f (kHz)↓	AMG		MIC(0)		MIC(1)	
Order→	1	2	1	2	1	2
5	20	5	24	70	11	16
10	22	10	38	196	15	25
20	33	20	67		24	48
40	66		107		40	

MIC(1) seems to require fewer iterations than AMG, whereas MIC(0) requires more iterations. Especially with linear finite elements, the convergence with MIC(1) is faster than with AMG and MIC(0), as can be seen in Table 2. However, Table 3 shows that the number of FLOPs with the MIC(1) preconditioner is about twice the number with AMG. This is mainly due

Table 3
The number of millions of floating point operations (MFLOPs) for the Helmholtz and Navier equations. Some numbers are missing as the computations were too demanding.

Helmholtz

f (kHz)↓	AMG			MIC(0)		MIC(1)	
Order→	1	2	3	1	2	1	2
0.5	0.5	7.4	43	0.4	13	0.5	35
1.0	2.1	31	170	2.2	110	2.9	270
2.0	17	210	1100	24	1800	32	3600
4.0	170	2000	12,000	260		390	

Navier

f (kHz)↓	AMG		MIC(0)		MIC(1)	
Order→	1	2	1	2	1	2
5	6.8	130	7.1	390	8.9	870
10	29	490	47	3700	63	7000
20	230	3500	530	88,000	760	93,000
40	2400		5900		9400	

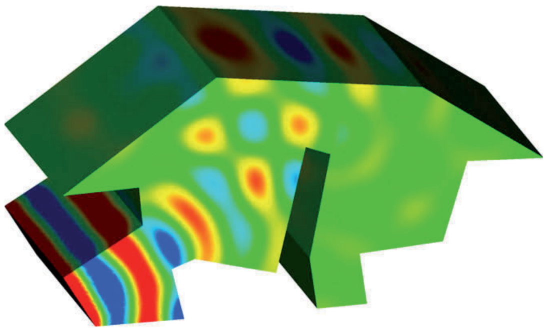

Fig. 5. The solution of the Helmholtz equation at the frequency $f = 880$ Hz in the three-dimensional car cabin.

Table 4
The number of iterations for the three-dimensional car cabin problem for the Helmholtz equation.

f (Hz)	Element order		
	1	2	3
110	14	17	22
220	17	23	29
440	26	34	46
880	51	72	97

to expensive factorization process before the iteration. With quadratic elements the MIC preconditioner seems to perform much worse than AMG, both in iteration counts as well as FLOPs. This is true for both Navier and Helmholtz problems. MIC(1) is also using more memory than AMG, although the difference is not substantial.

6.2.3. Three-dimensional car cabin problem

The car cabin problem is a three-dimensional generalization of the two-dimensional car cabin problem in [34]. The sound source is modelled as the Dirichlet boundary condition $p = 1$ posed on the wall behind pedals. The impedance boundary condition (3) with $\gamma = 0.2$ is posed on the other boundaries. The height of the car cabin is 1.5 m, the width is 1.5 m, and the length is 3 m. An example solution is plotted in Fig. 5. Iteration counts are reported in Table 4. For this problem also, the number of iterations grow roughly linearly with respect to the frequency.

6.2.4. Three-dimensional wedge problem for the Helmholtz equation

The three-dimensional wedge problem [41] in the unit cube $[0, 1]^3$ is a generalization of a two-dimensional problem studied in [28,21,34]. In this acoustic scattering problem, the material is inhomogeneous leading to a piece-wise constant speed

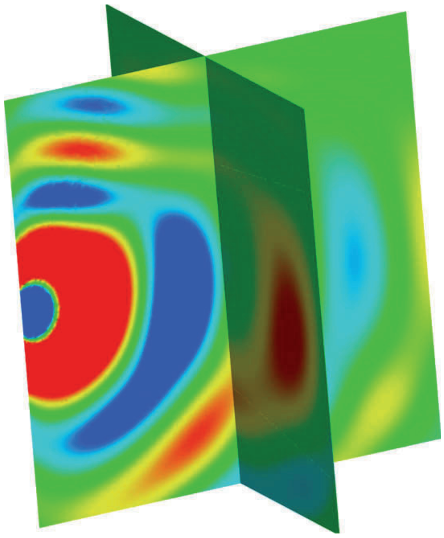

Fig. 6. The solution of the Helmholtz equation at $f = 2.5$ Hz for the three-dimensional wedge problem.

Table 5
The iteration counts for the three-dimensional wedge acoustic scattering problem.

f (kHz)	Element order		
	1	2	3
1.25	23	26	30
2.5	40	53	88

Table 6
The GMRES iteration counts for the crank shaft vibration problem.

f (kHz)	3	6	9	12	15
Iterations	231	263	223	187	347

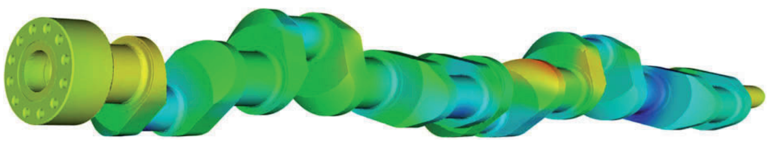

Fig. 7. The propagation of elastic waves in a crankshaft at $f = 3$ kHz. The color scale indicates the amplitude of the displacement, with blue corresponding to small displacement and red corresponding to large displacement.

of sound. The domain has three layers separated by two planes defined by the equations $z = 0.1x + 0.2y + 0.6$ and $z = -0.2x - 0.15y + 0.4$. The speeds of sound from the top layer to the bottom layer are $c_1 = 1, c_2 = \frac{1}{2}$, and $c_3 = \frac{5}{6}$. A point source is placed at (0.5,0,0.5) and the absorbing boundary conditions are posed on the boundaries. In the AMG method, the Jacobi relaxation parameter is $\omega = 0.3$.

The solution of the Helmholtz equation at $f = 2.5$ Hz is shown in Fig. 6. The iteration counts are reported in Table 5. The same linear growth can be observed as in the previous problems.

6.2.5. Crankshaft vibration problem

The Navier equation is solved in a complicated three-dimensional domain defined by the crank shaft model from Comsol Multiphysics 3.3. The length of the crankshaft is 1.0 m and it is made of structural steel defined by: the density

$\rho = 7850\ \mathrm{kg/m^3}$, Young modulus $E = 2 \cdot 10^{11}$ Pa, and Poisson ratio $\nu = 0.33$. A tangential vibration source on the left end is given by the Dirichlet boundary condition $u = (1, 0, 1)$. The right end is rigid, i.e. the Dirichlet boundary condition $u = (0, 0, 0)$ is posed on there. Other boundaries have natural boundary conditions, i.e. the impedance boundary condition (10) with $\gamma = 0$. The mesh is made of quadratic finite elements and 300,000 nodes.

The GMRES iteration counts on a range of frequencies are given in Table 6. As there is no absorption, the problem is singular at some frequencies. Due to this the iteration counts do not behave linearly with respect to the frequency. The solution at $f = 3$ kHz is illustrated in Fig. 7.

7. Conclusions

A damped Navier preconditioner based on an algebraic multigrid method was introduced for time-harmonic elasticity problems. This is a generalization of a shifted-Laplacian preconditioner for the Helmholtz equation. These preconditioners are efficient for Helmholtz and Navier problems in complicated two-dimensional and three-dimensional domains. Higher-order finite elements can be used for the discretization and Helmholtz problems can have variable coefficients. The proposed approach is especially well-suited for low-frequency and mid-frequency problems. For high frequencies, iteration counts grow roughly linearly with respect to the frequency. The same behavior was also observed in [34,21].

The performance was compared to a modified incomplete Cholesky (MIC) preconditioner. The AMG-based damped preconditioner was more efficient as its initialization requires much less computations than the expensive incomplete factorization procedure. Especially with quadratic finite elements, the AMG preconditioner was clearly faster.

The eigenvalues of the preconditioned system were also studied. The earlier results for the Helmholtz equation in [36] were generalized for the Navier equation. It was shown that the eigenvalues of the preconditioned system with the damped Navier preconditioner are on a circle in the complex plane for Dirichlet and Neumann boundary value problems. When one algebraic multigrid cycle is used instead of the exact inverse of the damped Navier operator, the eigenvalues are spread to some extent, but the conditioning is still fairly good.

Acknowledgements

We thank Dr. Janne Martikainen for making his C++ FEM class library available to us and Dr. Erkki Heikkola for his comments on the manuscript. The research was supported by the Academy of Finland Grants #121271 and #207089, the US Office of Naval Research Grant N00014-06-1-0067, and the US National Science Foundation Grant DMS-0610661.

References

[1] D.J. Nefske, J. Wolf, L. Howell, Structural-acoustic finite element analysis of the automobile passenger compartment: a review of current practice, J. Sound Vib. 80 (2) (1982) 247–266.
[2] L.L. Thompson, A review of finite-element methods for time-harmonic acoustics, J. Acoust. Soc. Am. 119 (3) (2006) 1315–1330.
[3] B. Engquist, A. Majda, Absorbing boundary conditions for numerical simulation of waves, Math. Comput. 31 (1977) 629–651.
[4] F. Ihlenburg, Finite element analysis of acoustic scattering, Applied Mathematical Sciences, vol. 132, Springer-Verlag, New York, 1998.
[5] Y. Saad, M.H. Schultz, GMRES: a generalized minimal residual algorithm for solving nonsymmetric linear systems, SIAM J. Sci. Statist. Comput. 7 (3) (1986) 856–869.
[6] H.A. van der Vorst, Bi-CGSTAB: a fast and smoothly converging variant of Bi-CG for the solution of nonsymmetric linear systems, SIAM J. Sci. Statist. Comput. 13 (2) (1992) 631–644.
[7] C. Farhat, A. Macedo, M. Lesoinne, F.-X. Roux, F. Magoulés, A. de La Bourdonnaie, Two-level domain decomposition methods with Lagrange multipliers for the fast iterative solution of acoustic scattering problems, Comput. Meth. Appl. Mech. Eng. 184 (2–4) (2000) 213–239.
[8] C. Farhat, P. Avery, R. Tezaur, J. Li, FETI-DPH: a dual-primal domain decomposition method for acoustic scattering, J. Comput. Acoust. 13 (3) (2005) 499–524.
[9] M.J. Gander, F. Magoulès, F. Nataf, Optimized Schwarz methods without overlap for the Helmholtz equation, SIAM J. Sci. Comput. 24 (1) (2002) 38–60.
[10] K. Ito, J. Toivanen, A fast iterative solver for scattering by elastic objects in layered media, Appl. Numer. Math. 57 (5–7) (2007) 811–820.
[11] K. Ito, Z. Qiao, J. Toivanen, A domain decomposition solver for acoustic scattering by elastic objects in layered media, J. Comput. Phys. 227 (19) (2008) 8685–8698.
[12] K. Otto, E. Larsson, Iterative solution of the Helmholtz equation by a second-order method, SIAM J. Matrix Anal. Appl. 21 (1) (1999) 209–229.
[13] L.S. Bennethum, X. Feng, A domain decomposition method for solving a Helmholtz-like problem in elasticity based on the Wilson nonconforming element, RAIRO Model. Math. Anal. Numer. 31 (1) (1997) 1–25.
[14] C. Farhat, J. Li, An iterative domain decomposition method for the solution of a class of indefinite problems in computational structural dynamics, Appl. Numer. Math. 54 (2) (2005) 150–166.
[15] F. Collino, S. Ghanemi, P. Joly, Domain decomposition method for harmonic wave propagation: a general presentation, Comput. Meth. Appl. Mech. Eng. 184 (2–4) (2000) 171–211. vistas in domain decomposition and parallel processing in computational mechanics.
[16] E. Faccioli, F. Maggio, A. Quarteroni, A. Tagliani, Spectral-domain decomposition methods for the solution of acoustic and elastic wave equations, Geophysics 61 (4) (1996) 1160–1174.
[17] E. Heikkola, S. Mönkölä, A. Pennanen, T. Rossi, Controllability method for the Helmholtz equation with higher-order discretizations, J. Comput. Phys. 225 (2) (2007) 1553–1576.
[18] S. Mönkölä, E. Heikkola, A. Pennanen, T. Rossi, Time-harmonic elasticity with controllability and higher-order discretization methods, J. Comput. Phys. 227 (11) (2008) 5513–5534.
[19] A. Brandt, I. Livshits, Wave-ray multigrid method for standing wave equations, Electron. Trans. Numer. Anal. 6 (1997) 162–181.
[20] H.C. Elman, O.G. Ernst, D.P. O'Leary, A multigrid method enhanced by Krylov subspace iteration for discrete Helmholtz equations, SIAM J. Sci. Comput. 23 (4) (2001) 1291–1315.
[21] Y.A. Erlangga, C.W. Oosterlee, C. Vuik, A novel multigrid based preconditioner for heterogeneous Helmholtz problems, SIAM J. Sci. Comput. 27 (4) (2006) 1471–1492.
[22] M. Griebel, D. Oeltz, M.A. Schweitzer, An algebraic multigrid method for linear elasticity, SIAM J. Sci. Comput. 25 (2) (2003) 385–407.

[23] O.G. Ernst, A finite-element capacitance matrix method for exterior Helmholtz problems, Numer. Math. 75 (2) (1996) 175–204.
[24] E. Heikkola, Y.A. Kuznetsov, P. Neittaanmäki, J. Toivanen, Fictitious domain methods for the numerical solution of two-dimensional scattering problems, J. Comput. Phys. 145 (1) (1998) 89–109.
[25] E. Heikkola, T. Rossi, J. Toivanen, A parallel fictitious domain method for the three-dimensional Helmholtz equation, SIAM J. Sci. Comput. 24 (5) (2003) 1567–1588.
[26] E. Bécache, P. Joly, C. Tsogka, Fictitious domains, mixed finite elements and perfectly matched layers for 2D elastic wave propagation, J. Comput. Acoust. 9 (3) (2001) 1175–1201. ultrasonic field synthesis and modeling (Trieste, 1999.
[27] M. Magolu monga Made, Incomplete factorization-based preconditionings for solving the Helmholtz equation, Int. J. Numer. Meth. Eng. 50 (2001) 1077–1101.
[28] R.E. Plessix, W.A. Mulder, Separation-of-variables as a preconditioner for an iterative Helmholtz solver, Appl. Numer. Math. 44 (3) (2003) 385–400.
[29] E. Turkel, Numerical methods and nature, J. Sci. Comput. 28 (2–3) (2006) 549–570.
[30] Y.A. Erlangga, C. Vuik, C.W. Oosterlee, On a class of preconditioners for solving the Helmholtz equation, Appl. Numer. Math. 50 (3–4) (2004) 409–425.
[31] A.L. Laird, M.B. Giles, Preconditioned iterative solution of the 2D Helmholtz equation, Technical Report 02/12, Oxford Computer Laboratory, Oxford, UK, 2002.
[32] J.D. Collins, J.M. Jin, J.L. Volakis, Eliminating interior resonances in finite element – boundary integral methods for scattering, IEEE Trans. Antennas Propag. 40 (12) (1992) 1583–1585.
[33] W.D. Murphy, V. Rokhlin, M.S. Vassiliou, Solving electromagnetic scattering problems at resonance frequencies, J. Appl. Phys. 67 (10) (1990) 6061–6065.
[34] T. Airaksinen, E. Heikkola, A. Pennanen, J. Toivanen, An algebraic multigrid based shifted-Laplacian preconditioner for the Helmholtz equation, J. Comput. Phys. 226 (1) (2007) 1196–1210.
[35] T. Airaksinen, S. Mönkölä, Comparison between shifted-laplacian preconditioning and controllability method for computational acoustics, J. Comput. Appl. Math. (2008), accepted for publication.
[36] M. van Gijzen, Y. Erlangga, C. Vuik, Spectral analysis of the discrete Helmholtz operator preconditioned with a shifted Laplacian, SIAM J. Sci. Comput. 29 (5) (2007) 1942–1958.
[37] Y. Saad, Iterative Methods for Sparse Linear Systems, second ed., Society for Industrial and Applied Mathematics (SIAM), Philadelphia, PA, 2003.
[38] E. Turkel, Y. Erlangga, Preconditioning a finite element solver of the exterior Helmholtz equation, in: P. Wesseling, E. Oñate, J. Périaux (Eds.), ECCOMAS CFD, ECCOMAS, 2006.
[39] F. Kickinger, Algebraic multi-grid for discrete elliptic second-order problems, in: Multigrid Methods V (Stuttgart, 1996), Springer, Berlin, 1998, pp. 157–172.
[40] I. Gustafsson, Modified incomplete Cholesky (MIC) methods, Preconditioning methods: analysis and applications, Top. Comput. Math., vol. 1, Gordon & Breach, New York, 1983, pp. 265–293.
[41] C. Vuik, Y. Erlangga, C. Oosterlee, M. van Gijzen, Complex shifted-Laplace preconditioners for the Helmholtz equation, in: C. Vuik (Ed.), Proceedings of the Ninth Copper Mountain Conference on Iterative Methods, April 2–7, Copper Mountain, CO, USA, 2006.

III

COMPARISON BETWEEN SHIFTED-LAPLACIAN PRECONDITIONING AND CONTROLLABILITY METHOD FOR COMPUTATIONAL ACOUSTICS

by

Tuomas Airaksinen, Sanna Mönkölä

Journal of Computational and Applied Mathematics 234 (2010) 1796-1802

Journal of Computational and Applied Mathematics 234 (2010) 1796–1802

Contents lists available at ScienceDirect

Journal of Computational and Applied Mathematics

journal homepage: www.elsevier.com/locate/cam

Comparison between the shifted-Laplacian preconditioning and the controllability methods for computational acoustics

Tuomas Airaksinen *, Sanna Mönkölä

Department of Mathematical Information Technology, University of Jyväskylä, P.O. Box 35 (Agora), FI-40014 University of Jyväskylä, Finland

ARTICLE INFO

Article history:
Received 30 November 2007
Received in revised form 9 April 2008

MSC:
93B05
35J05
65N30
65N35

Keywords:
Helmholtz equation
Computational acoustics
Algebraic multigrid method
Preconditioner
Exact controllability
Finite element method
Spectral element method

ABSTRACT

Processes that can be modelled with numerical calculations of acoustic pressure fields include medical and industrial ultrasound, echo sounding, and environmental noise. We present two methods for making these calculations based on Helmholtz equation. The first method is based directly on the complex-valued Helmholtz equation and an algebraic multigrid approximation of the discretized shifted-Laplacian operator; i.e. the damped Helmholtz operator as a preconditioner. The second approach returns to a transient wave equation, and finds the time-periodic solution using a controllability technique. We concentrate on acoustic problems, but our methods can be used for other types of Helmholtz problems as well. Numerical experiments show that the control method takes more CPU time, whereas the shifted-Laplacian method has larger memory requirement.

1. Introduction

The many applications of computational acoustics in industry range from medical measurement to machinery design. Computational acoustics enables the simulation of situations that would be difficult to explore experimentally. Compared to experiments, computer simulations provide a safe, fast, and cost-efficient way of providing guidelines for acoustical applications. Nevertheless, solving problems arising from real life acoustic applications by computer demands a considerable amount of time and memory. In particular, high-frequency phenomena are computationally demanding. This is because the resolution of the spatial discretization needs to be adjusted to the frequency to achieve accurate results. Furthermore, solutions with high frequency suffer from numerical dispersion. This the so-called pollution effect [1] cannot be avoided in two- and three-dimensional problems [2], but it can be reduced by using higher-order polynomial basis [3,4], among other methods. However, the pollution error in discretizations necessitates finer meshes for high-frequency problems.

Our aim is to develop efficient iterative solution methods for acoustic problems, which are modelled by the Helmholtz equation presented in Section 2. Element methods, such as the finite element method (FEM) and the spectral element method (SEM), have emerged as generic tools for discretizing the Helmholtz equation. The review [5] describes research efforts on this field (see also [6,7]). Finite element discretizations of the Helmholtz equation are non-Hermitian and indefinite. For mid-frequency and high-frequency problems, the resultant matrix can be extremely large, which often limits the feasible size of the scattering problem under consideration. As a result, the finite element discretizations of the Helmholtz

* Corresponding author.
E-mail address: tuomas.airaksinen@jyu.fi (T. Airaksinen).

0377-0427/$ – see front matter
doi:10.1016/j.cam.2009.08.030

equation are a challenge for the current solvers, and require the use of iterative methods such as the GMRES method or the BICGSTAB method [8]. These methods, in turn, require a good preconditioner for the discretized Helmholtz equations in order to have reasonably fast convergence.

In Section 3, we consider a shifted-Laplacian preconditioner that is obtained from the discretized damped Helmholtz operator. A preconditioner based on approximating a damped Helmholtz operator by a geometric multigrid cycle was considered in [9]. There, the scattering problems were posed on a rectangular domain and they were discretized using low-order finite differences, and a geometric multigrid method was used. Quadratic and cubic finite elements in particular helped to reduce the number of unknowns in order to reach prescribed accuracy, as they have much smaller interpolation and pollution errors than linear basis functions [1]. The preconditioner used in this paper, employs an algebraic multigrid (AMG) method in the approximation of the damped Helmholtz operator. In particular, the preconditioner can be constructed purely algebraically when the matrix for the 0th-order terms is also available.

An alternative iterative approach suitable for solving the Helmholtz equation via the time-dependent wave equation is presented in Section 4. The basic idea is to find a time-periodic solution to wave equations by using a controllability method. This leads to preconditioned conjugate gradient iterations for initial data. This technique was introduced for the Helmholtz equation in [10,11]. They used low-order finite elements for space discretization and second-order central finite differences for time discretization. Since low-order discretizations lead to poor accuracy, we have made improvements to the method. In [12], we used higher-order spectral elements for space discretization. We noticed that second-order time discretization limits the accuracy with elements of order $r = 3$ or higher, unless very fine time steps are used. That is why the fourth-order Runge–Kutta time discretization was applied to the method in [13]. Higher-order discretizations in both space and time domain provide high accuracy. However, with higher-order discretizations the computational cost is larger than with lower-order discretizations.

Comparison between the shifted-Laplacian and the controllability methods is presented in Section 5 with respect to CPU time and memory usage. Although the computational grids are not the same for both methods, the same number of discretization points is used for both methods to make comparisons reasonable. The accuracy of the discretizations is compared as well.

The methods that we use are not restricted to a certain application but can be suited to simulate several real life problems. Hence, our examples do not focus on a specific application. However, geometrical shapes similar to those used in our scattering examples can be used in several applications in audio technology and echo sounding. For example, noise barriers with cross sections as presented in our scattering examples can be used in environmental noise attenuation. In this setting, simulation results show where the noise is reduced to a certain level. In echo sounding, one can determine the location of the highest echo signal.

2. The Helmholtz equation and boundary conditions

Acoustic scattering can be described by the Helmholtz equation

$$-\nabla \cdot \frac{1}{\rho(\mathbf{x})}\nabla u - \frac{k(\mathbf{x})^2}{\rho(\mathbf{x})}u = 0, \tag{1}$$

where u denotes the complex-valued time-harmonic acoustic pressure field, $k(\mathbf{x}) = \omega/c(\mathbf{x})$ is the wave number, $\rho(\mathbf{x})$ is the density of the material, ω is the angular frequency of the sound, $c(\mathbf{x})$ is the speed of sound, and $\mathbf{x} = (x_1, x_2) \in \mathbb{R}^2$ is the space variable. The wave number k varies depending on location as materials change.

We consider two different boundary conditions: the Dirichlet boundary condition and the absorbing boundary condition. We decompose the boundary $\Gamma = \partial\Omega$ into two parts, Γ_d and Γ_a such that $\Gamma = \Gamma_d \cup \Gamma_a$. The Dirichlet boundary Γ_d is sound-soft and is described by the Dirichlet boundary condition

$$u = g_d \quad \text{on } \Gamma_d, \tag{2}$$

where function g_d gives the sound source.

The absorbing boundary condition should let outgoing waves propagate out of the domain without reflections, as the Sommerfeld radiation condition requires. Considering a perfect absorbing boundary condition as a non-local operator is computationally difficult, but it can be approximated by a local operator [14]. We use here the absorbing boundary condition

$$-\mathrm{i}k(\mathbf{x})u + \frac{\partial u}{\partial \mathbf{n}} = g_a \quad \text{on } \Gamma_a, \tag{3}$$

with the imaginary unit $\mathrm{i} = \sqrt{-1}$, outer normal vector $\mathbf{n}$, and source term g_a.

3. The finite element method and preconditioning with the shifted-Laplacian

In the finite element method, the weak formulation of the Helmholtz equation is used to form the discretized version of the equation. The weak form and corresponding spaces that are used here are identical to the ones described in [15]. The finite element discretization is made on a triangulation given by a set of non-overlapping triangles K_h such that

$\Omega_h = \bigcup_{\tau\in K_h} \tau$. Here h corresponds to the largest distance between discretization nodes and Ω_h is an approximation of the computational domain Ω. In this paper, linear and cubic finite elements are employed. They correspond to the first- and third-order Lagrangian polynomials as basis functions of elements, respectively. Ultimately, a system of linear equations

$$\mathbf{Au} = \mathbf{f}, \tag{4}$$

is obtained, where **A** is a sparse matrix, **u** is the vector that contains the values of u on triangulation nodes and **f** is a non-zero vector arising from the sound source.

In this case, **A** is indefinite and symmetric but non-Hermitian. Hence, the generalized minimal residual (GMRES) method [8] is a suitable iterative method for the sparse matrix equation (4). In the numerical experiments we use the full GMRES method without restarts.

Except for very small-scale problems, the system (4) is generally badly conditioned, and it leads to very slow convergence of Krylov subspace methods when applied directly to the system (4). To improve the conditioning and the speed of convergence, we right-precondition (4) by $\mathbf{B}^{-1}$ and solve the preconditioned system

$$\mathbf{AB}^{-1}\tilde{\mathbf{u}} = \mathbf{f}, \quad \mathbf{u} = \mathbf{B}^{-1}\tilde{\mathbf{u}}. \tag{5}$$

The goal is to find a preconditioner **B** such that the matrix $\mathbf{AB}^{-1}$ is well conditioned and multiplication of vectors by $\mathbf{B}^{-1}$, i.e. solving systems with the matrix **B**, can be done with a small computational effort. These ideal properties would lead to a fast convergence of the iterative method at a small overall computational cost.

In this paper, the preconditioner is based on a discretized form of the shifted-Laplacian operator $\mathcal{B}_{SL} = -\nabla \cdot \frac{1}{\rho(\mathbf{x})}\nabla - (\beta_1 + \beta_2 \mathrm{i})\,\frac{k(\mathbf{x})^2}{\rho(\mathbf{x})}$, as originally presented in [16]. By choosing $\beta_1 = 1$ and β_2 to be positive, $\mathcal{B}_{SL}$ corresponds to damped Helmholtz operator. In [15], the algebraic multigrid method (AMG) was used to approximate inversion of $\mathcal{B}_{SL}$. We use this preconditioner here and denote it by $\mathbf{B}_{MG}$. When evaluating $\mathbf{B}_{MG}^{-1}$ with the AMG method, we use one W-cycle with under relaxed Jacobi method with relaxation parameter $\omega_{\mathrm{jac}} = 0.4$ as the smoothener. One iteration of the Jacobi is used as a pre- and post-smoothener. The damping parameter β_2 is chosen to be 0.5, which was found to be a good choice in [15].

4. A control based approach with spectral elements

An alternative approach to solving the Helmholtz equation is based on finding a time-periodic solution of the associated transient wave equation via an exact controllability technique. To obtain the time-harmonic solution, we minimize the difference between initial conditions and the corresponding variables after one time period $T = 2\pi/\omega$. Proceeding this way, the problem of time-harmonic wave scattering can then be cast as a least squares problem

$$\min \left(\frac{1}{2} \int_{\Omega} \left| \frac{\partial U(T)}{\partial t} - e_1 \right|^2 \mathrm{d}x + \frac{1}{2} \int_{\Omega} |\nabla (U(T) - e_0)|^2 \, \mathrm{d}x \right), \tag{6}$$

where the initial conditions are contained in a vector $(e_0, e_1)^{\mathrm{T}} = (U(0), \frac{\partial U}{\partial t}(0))^{\mathrm{T}}$, and $U(t) = \mathrm{Re}(\mathrm{e}^{-\mathrm{i}kt}u)$ satisfies the time-dependent equations associated with the system (1)–(3).

The time-dependent wave equation and the function to be minimized in (6) are discretized in space domain with the spectral element method [3]. We use higher-order Lagrange interpolation polynomials as basis functions, and the nodes of these functions are placed at the Gauss–Lobatto discretization points. The integrals in the weak form of the equation are evaluated with the corresponding Gauss–Lobatto quadrature formulas. This leads to semi-discretized state equation

$$\mathbf{M}\frac{\partial^2 \mathbf{U}}{\partial t^2} + \mathbf{S}\frac{\partial \mathbf{U}}{\partial t} + \mathbf{KU} = \mathbf{F}, \tag{7}$$

where **U** is the global vector containing the values of the pressure $U(t)$ at the Gauss–Lobatto points of the quadrilateral mesh, **M** is the mass matrix, **S** is the matrix arising from the absorbing boundary condition, **K** is the stiffness matrix, and **F** is the vector due to the source functions $\mathrm{Re}\left(\mathrm{e}^{-\mathrm{i}kt} g_d\right)$ and $\mathrm{Re}\left(\mathrm{e}^{-\mathrm{i}kt} g_a\right)$. The least squares problem, where the function to be minimized is semi-discrete form, is

$$\min \left(\frac{1}{2} \left(\mathbf{U}(T) - e_0\right)^{\mathrm{T}} \mathbf{K} \left(\mathbf{U}(T) - e_0\right) + \frac{1}{2} \left(\frac{\partial \mathbf{U}(T)}{\partial t} - e_1 \right)^{\mathrm{T}} \mathbf{M} \left(\frac{\partial \mathbf{U}(T)}{\partial t} - e_1 \right) \right).$$

For time discretization we use the fourth-order Runge–Kutta method. The discretized minimization problem is solved by a preconditioned conjugate gradient (CG) algorithm. We use a block-diagonal preconditioner diag $(\mathbf{K}, \mathbf{M})$. The linear systems with the stiffness matrix **K** are solved by the algebraic multigrid method [17,15,13]. As a smoother for the AMG, we apply the successive over relaxation (SOR) method with relaxation factor equal to 1.2. One iteration of the SOR is used for a pre- and post-smoothener. Additionally, at the beginning of every multigrid iteration, four iterations of the SOR are used to smooth the solution initially. The so-called W-cycle [18] is utilized as a multigrid iteration until the residual norm of the solution is smaller than 10^{-6}.

Table 1
Number of nodes and number of space discretization points for different element orders in the coarsest meshes.

	SL method		Control method			
Element order	1	3	1	2	3	4
Mesh step size h	0.025–0.084	0.097–0.252	0.050	0.100	0.143	0.200
Number of nodes in mesh	5075	610	5040	1320	672	360
Number of space discretization points	5075	5142	5040	5040	5544	5040

5. Numerical experiments

We compared the efficiency of the methods, presented in Sections 3 and 4, by performing tests considering accuracy, computational cost and memory requirement. In both methods, the overall accuracy of the discrete solution depends on spatial discretization (performed by higher-order element methods with mesh step size h and element order r), the stopping criterion ε of the iterative method (GMRES or CG), approximation of the geometrical boundaries, and approximation of the radiation condition.

In the shifted-Laplacian method, we used an unstructured triangular mesh generated with Comsol Multiphysics 3.3. For the control method, a mesh consisting of polygonal elements was created by a mesh generator from Numerola Ltd. The meshes are built such that approximate number of discretization points is same for both methods. Since good efficiency can be achieved with higher-order elements by using sufficiently large mesh step size, we have used constant spatial discretization between different element orders (i.e., r/h is constant).

In [15,12,13], it is shown that the number of iterations needed to achieve a given stopping criterion is independent of the element order. Since with lower-order elements we can save CPU time by using rougher stopping criterion without loss of accuracy, we have used stopping criterion $\varepsilon = 10^{-(r+2)}$ with both methods for element order r, unless otherwise mentioned. In accuracy tests, we have used polygonal boundaries to avoid the error from approximating the geometry, in connection with a test problem that satisfies the absorbing boundary condition. Errors between the real parts of the analytical solution and the computational result are reported as L^∞-norms.

Time discretization, performed by the fourth-order Runge–Kutta scheme, affects the accuracy of the control method. To eliminate the temporal error, for elements of order r we use a timestep of length $\Delta t = \alpha_r h_{\min}/c_{\max}$, where $\alpha_1 = 2/3$, $\alpha_2 = 1/5$, $\alpha_3 = 7/80$, and $\alpha_4 = 5/90$. Here, $h_{\min}$ denotes the minimum mesh step size and $c_{\max}$ denotes the maximum sound speed.

Throughout the tests, we have chosen to use the propagation direction $(-1, 1)$, which is determined by wave vector $\mathbf{k} = \frac{1}{\sqrt{2}}(-1, 1)\,k$. The starting values $(e_0, e_1)^{\mathrm{T}}$ for the control method are set by the procedure presented in [13]. All computations have been carried out on an AMD Opteron 885 processor at 2.6 GHz. In the figures and tables, we use the abbreviation *SL method* for the shifted-Laplacian method.

5.1. Accuracy

The domain Ω, consisting of a fluid with density $\rho = 1$, is defined so that its outer boundary, Γ_a, coincides with the boundary of the rectangle $[0, 4]\times[0, 4]$. We have set a square obstacle, having a side length of 2 and boundary Γ_d in the center of the domain Ω. The error arising from the approximation of the absorbing boundary condition is eliminated by solving the Helmholtz problem with $g_d = e^{i\mathbf{k}\cdot\mathbf{x}}$ and $g_a = i\,(k_1 n_1 + k_2 n_2 - k)\,e^{i\mathbf{k}\cdot\mathbf{x}}$. The function $u = e^{i\mathbf{k}\cdot\mathbf{x}}$ satisfies this problem, and the solution of the corresponding time-dependent equation is $U = \cos(kt - \mathbf{k}\cdot\mathbf{x})$. The accuracy of the methods is compared with a series of tests where mesh step size is halved consecutively, starting from the meshes introduced in Table 1.

In the first accuracy experiment, we used angular frequency $\omega = 2\pi$ and wave speed $c(\mathbf{x}) = 1$ corresponding to the constant wave number $k = 2\pi$. As mesh refinement with a constant wave number leads to more accurate results, we also refine the stopping criterion in this particular test, as opposed to the usual stopping criterion $\varepsilon = 10^{-(r+2)}$ for r^{th}-order elements. Theoretically, the asymptotic maximum error between the analytical solution and the computed solution is divided by four for the element order $r = 1$ and by sixteen for $r = 3$, when the total number of elements in the mesh is multiplied by four (i.e., the mesh step size is divided by two). To guarantee that the stopping criterion does not limit the accuracy, we have used stopping criteria $\varepsilon = 10^{-3}, 5\times10^{-4}, 10^{-4}, 5\times10^{-5}, 10^{-5}$ for $r = 1$ with increasing mesh density. Respectively, within each mesh refinement for $r = 3$, we have divided the stopping criterion by ten. The results with element orders $r = 1$ and $r = 3$, plotted in Fig. 1, are in line with the theoretical consideration, and they show that using higher-order elements is better then refining the mesh when high efficiency is needed. With the control method in particular, the computations with fine grids are inefficient since small time steps need to be used to satisfy the stability and accuracy demands. Consequently, to obtain the prescribed level of the residual for the three smallest values of h and Δt with spectral elements and $r = 3$, more than 1000 iterations (our maximum number of iterations) are required.

Because solving acoustic problems with large frequencies is of special interest, we have performed another set of experiments by doubling the angular frequency with every mesh refinement. In these tests, we have set ωh constant for angular frequencies $\omega = 2\pi, 4\pi, 8\pi, 16\pi, 32\pi$, and the number of space discretization points has been approximately 20 per wavelength. The results presented in Fig. 2 for the shifted-Laplacian method with $r = 1, 3$ and the control method

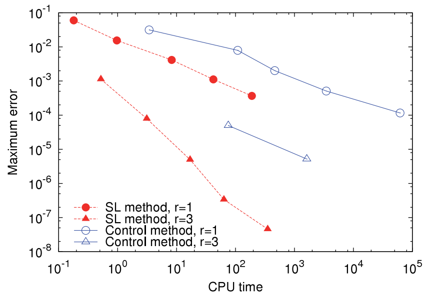

Fig. 1. Errors with respect to CPU time (in seconds). On each line, mesh step size is divided by two, consecutively, and angular frequency $\omega = 2\pi$ is kept constant.

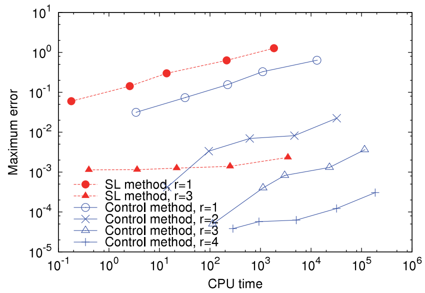

Fig. 2. Errors with respect to CPU time (in seconds). On each line, there are points for angular frequencies $\omega = 2\pi, 4\pi, 8\pi, 16\pi, 32\pi$ when ωh is a constant giving approximately 20 discretization points per wavelength.

with $r = 1, 2, 3, 4$ show how the pollution error deteriorates the accuracy as the frequency becomes larger. The lowest-order elements ($r = 1$) become useless with both methods as the angular frequency increases. The higher-order methods appear to be the most effective in both respects. We see that better accuracy is gained by the control method with spectral element discretization, but the shifted-Laplacian method with triangular finite elements appears to be faster. Due to the comparatively large discretization error in connection with our triangular space discretization, the pollution error is not clearly visible for the cubic elements ($r = 3$) within the frequency range used in this experiment. However, it is possible to improve the accuracy at the expense of computational time with triangular elements by using denser discretization mesh.

5.2. Scattering

We illustrate acoustic scattering by solving the Helmholtz problem with $g_d = 0$ and $g_a = \mathrm{i}\,(k_1 n_1 + k_2 n_2 - k)\,\mathrm{e}^{\mathrm{i}\mathbf{k}\cdot\mathbf{x}}$ in both homogeneous and heterogeneous domains. The outer boundary of the domain coincides with the boundary of the rectangle $[-3/4, 3/4] \times [-3/4, 3/4]$. Density is assumed to be constant $\rho(\mathbf{x}) = 1$. For tests in homogeneous domain we have used $c(\mathbf{x}) = 1$. In the heterogeneous test case, parameters are the same, except $c(\mathbf{x}) = 1.5$ for $x_1 \notin [-3/20, 3/20]$. Our methods can be applied to complex geometries as well, and as an example of such a geometry we have chosen a crescent-shaped scatterer. The scatterer can be described as the set of points inside the closed disk of radius $3\sqrt{2}/20$ centered at the origin but outside the open disk of radius $3\sqrt{2}/20$ centered at $(3/10, 0)$. See Fig. 4.

In these tests, we have used angular frequencies $\omega = 12\pi, 24\pi, 48\pi, 96\pi, 192\pi$ for element orders $r = 1, 3$. The scattering problems are solved by using constant ωh, implying approximately 10 space discretization points per wave length in the homogeneous domain and for $x_1 \in [-3/20, 3/20]$ in the heterogeneous domain. Respectively, the number of space discretization points per wave length is approximately 15 for $x_1 \notin [-3/20, 3/20]$ in the heterogeneous domain. The mesh is refined every time the angular frequency is doubled, as in the previous test measuring the influence of the pollution error. An example of a solution, computed by the shifted-Laplacian method with $r = 1$, at angular frequency $\omega = 48\pi$ is plotted in Fig. 5.

The CPU times and maximum memory usage for these scattering tests are shown in Fig. 3. It can be seen that memory requirement is almost equal between the methods when the frequency is low. As the frequency increases, the GMRES iterations increase in the shifted-Laplacian method. At the same time, the memory needed for storing the Krylov subspace grows as well. The memory requirement of the control method stays constant regardless of the growing number of iterations. Replacing GMRES method with another method, such as BICGSTAB, would remove this linearly growing memory requirement.

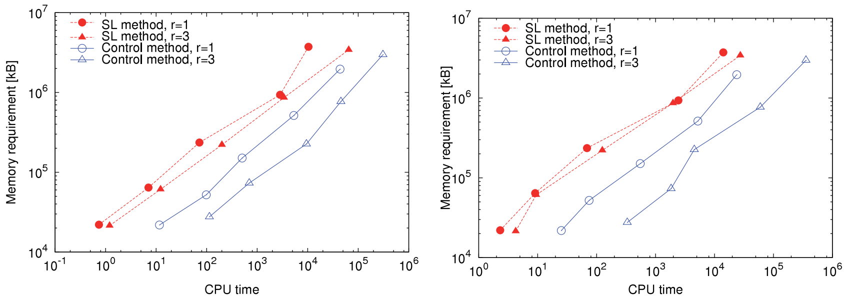

(a) Homogeneous.

(b) Heterogeneous.

Fig. 3. Memory usage with respect to CPU time (in seconds). On each line, there are points for angular frequencies $\omega = 12\pi, 24\pi, 48\pi, 96\pi, 192\pi$ when ωh is a constant giving approximately 10 discretization points per wavelength.

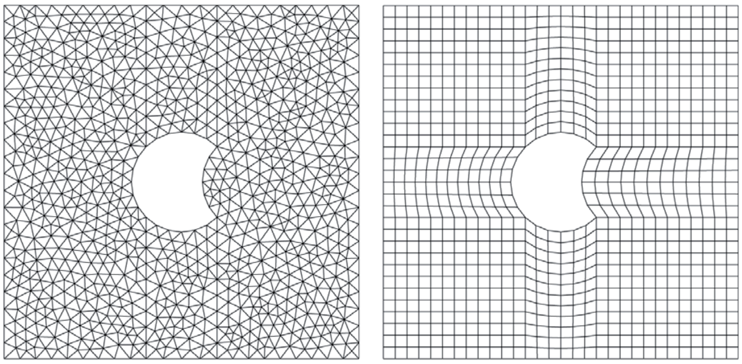

(a) Mesh for the method with shifted-Laplacian preconditioning.

(b) Mesh for the control method.

Fig. 4. Geometry and the coarsest meshes for both methods with $r = 3$ in scattering tests.

(a) Homogeneous.

(b) Heterogeneous.

Fig. 5. Solution of the scattering problem in homogeneous and heterogeneous domains at angular frequency $\omega = 48\pi$ with the method with shifted-Laplacian preconditioning and $r = 1$.

6. Conclusions

From the numerical tests we can conclude that the control method gave more accurate results but it took more CPU time than the shifted-Laplacian method. One reason for the lower accuracy with the shifted-Laplacian method is the unstructured mesh with changing step size h, as seen in Table 1. It is worth mentioning that the shifted-Laplacian method has quadratic CPU time and linear memory requirement due to the necessity to build Krylov subspace at each GMRES iteration. Choosing some other iterative method, such as BICGSTAB, to the outer iteration could lead to better performance as measured by CPU time. In addition, quadrilateral spectral elements require fewer discretization nodes than triangular finite elements to obtain the same accuracy level.

Acknowledgements

The first author was supported by the Academy of Finland grant #207089. Authors are thankful to Janne Martikainen for letting them use his finite element C++ library in the implementation of the shifted-Laplacian method, and Anssi Pennanen for letting them use his algebraic multigrid code. Jari Toivanen is acknowledged for his advantageous comments on the manuscript. The authors thank the referees for their comments which helped to improve the paper. Thanks are also due to their supervisors, Tuomo Rossi and Erkki Heikkola.

References

[1] F. Ihlenburg, Finite Element Analysis of Acoustic Scattering, Springer-Verlag, Berlin, 1998.
[2] I.M. Babuška, S.A. Sauter, Is the pollution effect of the FEM avoidable for the Helmholtz equation considering high wave numbers?, SIAM Journal on numerical analysis 34 (6) (1997) 2392–2423.
[3] G. Cohen, Higher-Order Numerical Methods for Transient Wave Equations, Springer-Verlag, Berlin, 2001.
[4] P. Šolín, K. Segeth, I. Doležel, Higher-Order Finite Element Methods, Chapman & Hall/ CRC Press, Boca Raton, 2004.
[5] L.L. Thompson, A review of finite-element methods for time-harmonic acoustics, Journal of the Acoustical Society of America 119 (3) (2006) 1315–1330.
[6] D. Pathria, G.E. Karniadakis, Spectral element methods for elliptic problems in nonsmooth domains, Journal of Computational Physics 122 (1) (1995) 83–95.
[7] O.Z. Mehdizadeh, M. Paraschivoiu, Investigation of a two-dimensional spectral element method for Helmholtz's equation, Journal of Computational Physics 189 (2003) 111–129.
[8] Y. Saad, Iterative Methods for Sparse Linear Systems, 2nd edition, SIAM, Philadelphia, 2003.
[9] Y.A. Erlangga, C.W. Oosterlee, C. Vuik, A novel multigrid based preconditioner for heterogeneous Helmholtz problems, SIAM Journal on Scientific Computing 27 (4) (2006) 1471–1492.
[10] M.O. Bristeau, R. Glowinski, J. Périaux, Using exact controllability to solve the Helmholtz equation at high wave numbers, in: R. Kleinman, T. Angell, D. Colton, F. Santosa, I. Stakgold (Eds.), Mathematical and Numerical Aspects of Wave Propagation, SIAM, Philadelphia, Pennsylvania, 1993, pp. 113–127.
[11] M.O. Bristeau, R. Glowinski, J. Périaux, Controllability methods for the computation of time-periodic solutions; application to scattering, Journal of Computational Physics 147 (2) (1998) 265–292.
[12] E. Heikkola, S. Mönkölä, A. Pennanen, T. Rossi, Controllability method for acoustic scattering with spectral elements, Journal of Computational and Applied Mathematics 204 (2) (2007) 344–355.
[13] E. Heikkola, S. Mönkölä, A. Pennanen, T. Rossi, Controllability method for the Helmholtz equation with higher-order discretizations, Journal of Computational Physics 225 (2) (2007) 1553–1576.
[14] B. Engquist, A. Majda, Absorbing boundary conditions for numerical simulation of waves, Mathematics of Computation 31 (1977) 629–651.
[15] T. Airaksinen, E. Heikkola, A. Pennanen, J. Toivanen, An algebraic multigrid based shifted-Laplacian preconditioner for the Helmholtz equation, Journal of Computational Physics 226 (2007) 1196–1210.
[16] Y.A. Erlangga, C. Vuik, C.W. Oosterlee, On a class of preconditioners for solving the Helmholtz equation, Applied Numerical Mathematics 50 (3–4) (2004) 409–425.
[17] J. Martikainen, A. Pennanen, T. Rossi, Application of an algebraic multigrid method to incompressible flow problems, Reports of the Department of Mathematical Information Technology, Series B. Scientific Computing, B 2/2006, University of Jyväskylä (2006).
[18] W. Hackbusch, Multigrid Methods and Applications, Springer-Verlag, Berlin, Germany, 1985.

IV

ACTIVE NOISE CONTROL IN A STOCHASTIC DOMAIN BASED ON A FINITE ELEMENT MODEL

by

Tuomas Airaksinen, Erkki Heikkola, Jari Toivanen

Reports of the Department of Mathematical Information Technology, Series B.
Scientific Computing, B 1 / 2009, Submitted to a journal

Active noise control in a stochastic domain based on a finite element model

Tuomas Airaksinen* Erkki Heikkola† Jari Toivanen‡

Abstract

The optimization of active noise control based on a finite element model for acoustic field is considered. Fixed number of actuators are located on the boundary of a three-dimensional enclosed acoustic space which could be vehicle interior, for example. Actuator signals are used to minimize known harmonic noise at specified locations. Noise control system needs to be robust with respect to many randomly varying parameters such as small variations in the acoustic space. In vehicle acoustics, these variations could be changes in the posture of vehicle driver. The treatment of this aspect is studied by using a stochastic computational domain in the finite element model. This leads to a quadratic optimization problem. Numerical results show significant noise reductions in drivers ears in a realistic car interior.

1 Introduction

Many machines generate disturbing noises to their users. Rotating and constantly moving parts such as wheels, engines and cooler fans are typical noise sources. Noise control applications are found especially in factory environment, engineering vehicles and passenger cars. It is possible to reduce noise significantly by different methods. Probably the most effective way to control noise is to remove or reduce important noise source mechanisms by suitable design choices. In many cases, however, this is not possible or the design is limited by other more important factors than noise. Then there are two basic approaches for noise attenuation: active and passive methods [1, 2].

Passive noise reduction by absorbing and insulating acoustic elements is effective for high frequency noise but typically less effective for low frequency noise, as long waves require large elements. On the other hand, active noise control (ANC) is most effective for low frequency noise. Active attenuation is based on generating

*Department of Mathematical Information Technology, University of Jyväskylä, PO Box 35 (Agora), FI-40014 University of Jyväskylä, Finland, tuomas.airaksinen@jyu.fi

†Numerola Oy, P.O. Box 126, FI-40101 Jyväskylä, Finland erkki.heikkola@numerola.fi

‡Institute for Computational and Mathematical Engineering, Building 500, Stanford University, Stanford, CA 94305, USA, tene@mit.jyu.fi

antisound with actuators, such that original noise is cancelled. The antisound must have the same amplitude as the noise to be cancelled, but the opposite phase so that destructive interference occurs. If the noise contains both high and low frequency components, the best noise attenuation is obtained by combining both active and passive methods together.

There are different ways to implement ANC system - some are applicable only to specific problems while others are more general. If the sound propagation is essentially one-dimensional, specific controller circuits can generate signal for an actuator minimizing sound at a sound sensor. These methods are reviewed in [3]; applications feature, for example, ANC modules integrated to air conditioning ducts [4] and exhaust pipes [5].

It is more difficult to implement ANC system that reduces the noise in a complicated three-dimensional domain. The noise control in passenger cars and other vehicles is a challenging future ANC application. In the passenger car, low frequency noise sources are mainly due to structural vibration from engine and tires [6]. Especially structure-borne noises are low frequency, whereas airborne noises often have higher frequencies. Tires cause high frequency noise due to aerodynamic phenomena. The mechanical vibratory noise from tires is mainly below 1 kHz. The most important noise components originating in the passenger car engine are below 500 Hz. The resonanse of car cabin is also an important low frequency noise source.

As there are low-frequency noise sources, ANC system could provide a significant noise reduction to the car cabin environment. There exists several approaches to implement a three-dimensional ANC system, but they are not very effective or general yet. More advanced methods employ numerical simulation and optimization. ANC methods that use finite element modeling, are presented in articles [7, 8]. In [7], resonance modes for mining vehicle are studied by modal coupling analysis and antinoise is optimized by using FEM model to obtain global noise control in the cabin. In [8], a local active noise control method based on the finite element method is described which minimizes noise locally in microphone locations. A method to determine the optimal locations for antinoise actuators are also presented. In [9], an optimal active noise control implementation based on quadratic programming and boundary element method (BEM) is presented.

Here, a novel approach on active noise control is considered. It is based on acoustic modeling in a stochastic domain. The antinoise is optimized by minimizing the expectation value of the noise. It is important that the ANC system tolerates random variations in the noice control environment. The stochasticity of the cavity domain implies that the ANC method presented here provides more reliable noise attenuation than earlier methods. The numerical example, ANC in a car cabin, shows the efficiency of the presented method.

This article is organized as follows. In Section 2, a mathematical model of sound propagation, the Helmholtz partial differential equation, and a numerical method to solve it are briefly presented. In Section 3, the local noise control in a stochastic domain is formulated as a quadratic optimization problem. In Section 4, an example of local noise control in car driver's ears is described. In Section 5, the numerical results of ANC performance in three-dimensional car cabin problem are studied and analyzed. In Section 6, conclusions are given.

2 Acoustic model

The time harmonic sound propagation can be modelled by the Helmholtz equation for the complex pressure amplitude $\hat{p}(\mathbf{x})$ which defines the amplitude and phase of the pressure. The sound pressure at time t is obtained as $e^{-i\omega t}p$, where ω is the angular frequency of sound and $i = \sqrt{-1}$. In a differential form, the Helmholtz equation reads

$$-\boldsymbol{\nabla} \cdot \frac{1}{\rho} \boldsymbol{\nabla} p - \frac{\omega^2}{c^2 \rho} p = f \quad \text{in}\, \Omega, \tag{1}$$

where $\rho(\mathbf{x})$ is the density of the material at location $\mathbf{x}$, $c(\mathbf{x})$ is the speed of sound in the material and $f(\mathbf{x})$ is the sound source term. A partially absorbing wall material is modelled by the impedance boundary condition

$$\frac{\partial p}{\partial \mathbf{n}} = \frac{i\eta\omega}{c} p \quad \text{on}\ \partial\Omega, \tag{2}$$

where $\eta(\mathbf{x})$ is the absorption coefficient depending on the properties of the surface material. The value $\eta = 1$ approximates a perfectly absorbing material and the value $\eta = 0$ approximates a sound-hard material (the Neumann boundary condition).

An approximate solution for the partial differential equation (PDE) Eq. (1) can be obtained using a finite element method [10]. The finite element discretization transforms Eq. (1) into a system of linear equations $\mathbf{Ax} = \mathbf{b}$, where the matrix $\mathbf{A}$ is generally symmetric, large, and sparse. Due to the large size and structure of $\mathbf{A}$, direct solution methods are computationally too expensive. Instead an iterative solution methods like GMRES [11] needs to be used. Solving the system with a reasonable number of iterations is, however, challenging as the matrix $\mathbf{A}$ is badly conditioned and especially so when the calculation domain is large and the frequency is high. In the numerical example in Section 5, the solutions are computed after the systems are preconditioned by a damped Helmholtz preconditioner described in [12, 13].

3 The noise control problem

An acoustic model in an enclosed stochastic domain $\Omega(\mathbf{r})$ is considered, where $\mathbf{r} = (r_1, r_2, \cdots, r_n)^T$ is a random variable that conforms to a known probability distribution $F(\mathbf{r})$. The pressure amplitude $p(\mathbf{x}, \mathbf{r}, \boldsymbol{\gamma})$ is the sum of the sound pressures caused by noise and n antinoise sources

$$p(\mathbf{x}, \mathbf{r}, \boldsymbol{\gamma}) = p_0(\mathbf{x}, \mathbf{r}) + \sum_{j=1}^{n} \gamma_j p_j(\mathbf{x}, \mathbf{r}), \tag{3}$$

where the pressure amplitude p_0 is due to the noise source, p_j is due to the jth antinoise source, and γ_j is a complex coefficient defining the amplitude and phase of the jth antinoise source. The noise and antinoise sources are located on the boundaries of Ω. The antinoise defined by the coefficients γ_j is optimized so that the noise is minimized in a subdomain denoted by $\Xi(\mathbf{r}) \subset \Omega(\mathbf{r})$. For this, a noise measure is defined as

$$
\begin{aligned}
N(\mathbf{r},\boldsymbol{\gamma}) &= \int\limits_{\Xi(\mathbf{r})} |p(\mathbf{x},\mathbf{r},\boldsymbol{\gamma})|^2 g(\mathbf{x})\,d\mathbf{x} \\
&= \int\limits_{\Xi(\mathbf{r})} p(\mathbf{x},\mathbf{r},\boldsymbol{\gamma})\,\bar{p}(\mathbf{x},\mathbf{r},\boldsymbol{\gamma})\,g(\mathbf{x})\,d\mathbf{x},
\end{aligned}
\tag{4}
$$

where $g(\mathbf{x})$ is a weighting function and $\bar{p}$ is the complex conjugate of p.

As the domain Ω is stochastic, the expectation value of the noise measure is given by

$$
E(N(\mathbf{r},\boldsymbol{\gamma})) = \int N(\mathbf{r},\boldsymbol{\gamma})\,F(\mathbf{r})\,d\mathbf{r}, \tag{5}
$$

where $F(\mathbf{r})$ is the probability distribution of $\mathbf{r}$. The objective function J for optimization is chosen to be an approximation of the integral (5) and it is given by the numerical quadrature

$$
J(\boldsymbol{\gamma}) = \sum_{j=1}^{m} w_j N(\mathbf{r}_j,\boldsymbol{\gamma})\,F(\mathbf{r}_j)\,, \tag{6}
$$

where the pairs $(\mathbf{r}_j, w_j)$ give the quadrature points and weights. The optimization problem is defined as

$$
\min_{\boldsymbol{\gamma}} J(\boldsymbol{\gamma})\,. \tag{7}
$$

In order to give the objective function in a compact form, the following notations are introduced:

$$
\begin{aligned}
\mathbf{p}(\mathbf{x},\mathbf{r}) &= \left(p_1(\mathbf{x},\mathbf{r})\,, p_2(\mathbf{x},\mathbf{r})\,, \cdots, p_n(\mathbf{x},\mathbf{r})\right)^T, \\
a &= \sum_{j=1}^{m} w_j F(\mathbf{r}_j) \int\limits_{\Xi(\mathbf{r}_j)} p_0(\mathbf{x},\mathbf{r}_j)^2\, g(\mathbf{x})\,d\mathbf{x}, \\
\mathbf{b} &= \sum_{j=1}^{m} w_j F(\mathbf{r}_j) \int\limits_{\Xi(\mathbf{r}_j)} p_0(\mathbf{x},\mathbf{r}_j)\,\bar{\mathbf{p}}(\mathbf{x},\mathbf{r}_j)\,g(\mathbf{x})\,d\mathbf{x}, \quad \text{and} \\
\mathbf{A} &= \sum_{j=1}^{m} w_j F(\mathbf{r}_j) \int\limits_{\Xi(\mathbf{r}_j)} \mathbf{p}^T(\mathbf{x},\mathbf{r}_j)\,\bar{\mathbf{p}}(\mathbf{x},\mathbf{r}_j)\,g(\mathbf{x})\,d\mathbf{x},
\end{aligned}
\tag{8}
$$

where $\bar{\mathbf{p}}$ is the elementwise complex conjugate of the vector $\mathbf{p}$ and the superscript ^{T} denotes the transpose. By expanding terms and by using the notations in Eq. (8), the objective function in Eq. (6) can be expressed in a compact form

$$J(\gamma) = \boldsymbol{\gamma}^H \mathbf{A} \boldsymbol{\gamma} + \boldsymbol{\gamma}^H \mathbf{b} + \mathbf{b}^H \boldsymbol{\gamma} + a, \tag{9}$$

where superscript ^{H} stands for the Hermitian conjugate. Optimal complex coefficients γ_i that give phases and amplitudes for antinoise actuators, are now given by the optimality condition $\boldsymbol{\nabla}_{\boldsymbol{\gamma}} J = \mathbf{0}$. This leads to a system of linear equations $\mathbf{A}\boldsymbol{\gamma} = -\mathbf{b}$, which has the solution

$$\boldsymbol{\gamma} = -\mathbf{A}^{-1}\mathbf{b}. \tag{10}$$

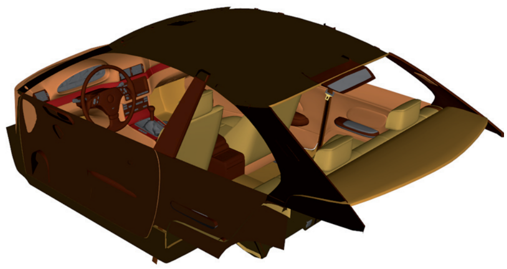

Figure 1: A three-dimensional model of BMW 330i car interior.

4 Car interior noise control

As an example application of the ANC method, the noise control in BMW 330i car interior is studied, see Fig. 1. The interior of the car excluding the driver is the domain $\Omega(\mathbf{r})$. The objective of the noise control is to minimize noise in driver's ears. Thus, Ξ is defined as a set

$$\Xi(\mathbf{r}) = \{\mathbf{e}_l, \mathbf{e}_r\} \subset \Omega(\mathbf{r}), \tag{11}$$

where $\mathbf{e}_l(\mathbf{r})$ and $\mathbf{e}_r(\mathbf{r})$ are the co-ordinates of the left and right ear, respectively. The noise measure in Eq. (4) has now the expression

$$N(\mathbf{r}, \boldsymbol{\gamma}) = |p(\mathbf{e}_l, \mathbf{r}, \boldsymbol{\gamma})|^2 + |p(\mathbf{e}_r, \mathbf{r}, \boldsymbol{\gamma})|^2.$$

It is assumed that there is only the driver and no other passengers or significant objects in the car that would influence the sound propagation. Driver's variable properties like shape and posture have an impact on reflections and propagation

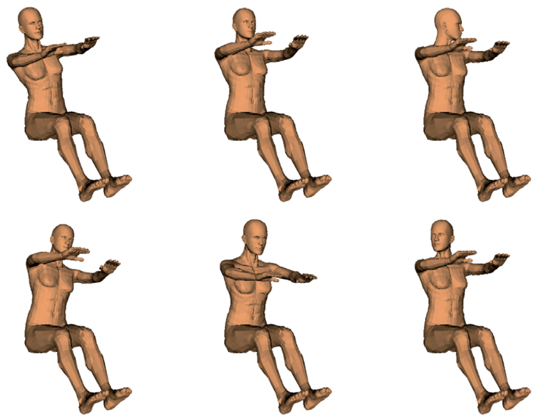

(a) r_1 (b) r_2 (c) r_3

Figure 2: Driver's posture parameters: (a) r_1 is driver's sideways bending angle, (b) r_2 is the forward bending angle, (c) r_3 is head rotation angle to left/right. Upper figures correspond to the lowest value of the parameter and lower figures correspond to the highest value of the parameter.

of sound, so they must be taken into account. Especially the posture and position of head affect the sound heard by ears. As the posture varies to some extent, it is better to minimize the expectation value of the sound level in ears. This leads to a stochastic domain in the computation.

The driver is modeled by using the freely available Animorph library, that is based on ideas and algorithms presented in [14]. With Animorph, it is possible to model driver's geometry with a rich set of parameters changing the posture and shape. Three parameters are considered here: r_1 is driver's sideways bending angle, r_2 is forward bending angle, and r_3 is head rotation angle to left/right. These parameters are illustrated in Fig. 2.

Now the random variable $\mathbf{r} = (r_1, r_2, r_3)^T$ determines the posture of the driver, where the value of each parameter is limited by condition $L_i < r_i < H_i$, $i \in \{1, 2, 3\}$. The expectation value in Eq. (5) reads now

$$E\left(N\left(\mathbf{r},\boldsymbol{\gamma}\right)\right) = \int\limits_{r_1=L_1}^{H_1} \int\limits_{r_2=L_2}^{H_2} \int\limits_{r_3=L_3}^{H_3} N\left(\mathbf{r},\boldsymbol{\gamma}\right) F\left(\mathbf{r}\right) dr_3 dr_2 dr_1. \tag{12}$$

The probability distribution function F is given by a piecewise trilinear function defined by the nodal values on the lattice $\{L_1, C_1, H_1\} \times \{L_2, C_2, H_2\} \times \{L_3, C_3, H_3\}$ and elsewhere by trilinear interpolation. The integral in Eq. (12) is estimated by the three-dimensional generalization of the trapedzoidal quadrature rule. The numerical integration of expression in Eq. (12) gives the objective function

$$J(\gamma) = E(N(\mathbf{r},\gamma)) = \sum_{i=1}^{m} w_i N(\mathbf{r}_j,\gamma) F(\mathbf{r}_j), \tag{13}$$

where w_i is a weight coefficient from the trapezoidal rule for the integral of the probability distribution function F and $\mathbf{r}_i$ is the co-ordinate triplet of the ith quadrature point.

To evaluate the objective function in Eq. (13), the pressure amplitude caused by each noise and antinoise source is needed in ears for each driver sample $\mathbf{r}_i$. The acoustic reciprocity principle allows here a significant computational saving, which is explained in the following. First, a finite element model which has a point noise source at the ear $\mathbf{e}_i$ is set up. Then, the pressure amplitude is studied in a noise or antinoise surface S. By the reciprocity the following holds: the sound emitted by the source S measured at the ear $\mathbf{e}_i$ has the same pressure amplitude as the sound emitted from the ear $\mathbf{e}_i$ measured over the surface S. Thus, the sound pressure amplitude caused by many different sound sources can be resolved by just performing one simulation. The pressure amplitude heard at the ear $\mathbf{e}_i$ is given by the integral

$$p_S(\mathbf{e}_i) = \int_S p_{\mathbf{e}_i}(\mathbf{x}) f_S(\mathbf{x})\, d\mathbf{x}, \tag{14}$$

where $p_S(\mathbf{e}_i)$ is the sound pressure propagated from the surface S that is heard at the ear $\mathbf{e}_i$, $f_S(\mathbf{x})$ is the force term for the sound source S, and $p_{\mathbf{e}_i}(\mathbf{x})$ is the sound pressure propagated from the ear $\mathbf{e}_i$ at the point $\mathbf{x}$ on the surface S. With a point antinoise source S, the integral in Eq. (14) is replaced by the point value at $\mathbf{x} = S$.

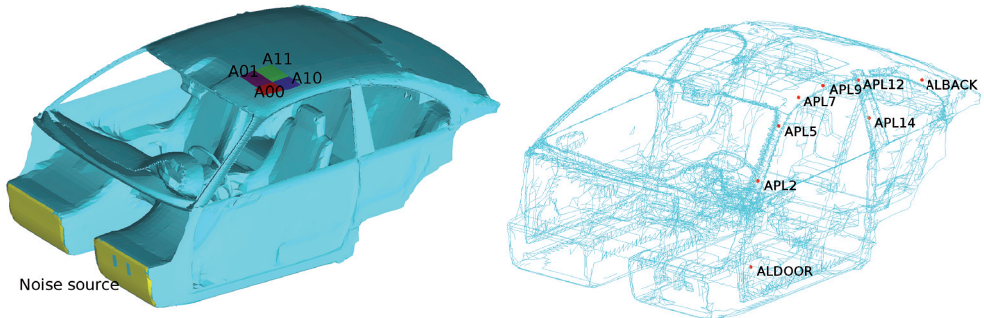

Figure 3: In the left figure, the noise source and planar antinoise sources are marked and labeled. In the right figure, there are point antinoise sources; only left side actuators are marked and labeled. The corresponding actuators on the right side are defined symmetrically on the right side of the cabin.

5 Numerical experiments

5.1 Definition of the model

In the numerical example model, the stochasticity of the domain $\Omega(\mathbf{r})$ implies that the Helmholtz equation Eq. (1) is solved many times with the driver in different postures. Table 1 lists the sampled values for the parameters r_1, r_2, and r_3. The center of the probability function F is at $\mathbf{C} = (0, 0, 0)$ and the corners are at $\mathbf{L} = (-25, -7.5, -62.5)$ and $\mathbf{H} = (25, 17.5, 62.5)$. On the boundaries of the rectangular prism $[L_1, H_1] \times [L_2, H_2] \times [L_3, H_3]$, the probability function is set to zero, $f(\mathbf{r}) = 0$.

Table 1: The parameter values for driver's stochastic variables r_i are given on the second column. The third column gives the identification of the parameter used in Animorph library.

Parameter	Values [°]	Animorph parameter
r_1, sideways bending	-20,-10,0,10,20	360_torso/ROT1
r_2, forward bending	-5,0,5,10,15	360_torso/ROT2
r_3, head rotation	-50,-25,0,25,50	300_head/ROT2

To solve the Helmholtz equation in Eq. (1) with the finite element method, a collection of meshes consisting of linear tetrahedra and triangles were generated with Ansys ICEM CFD. Each mesh corresponds to different driver posture and they were generated so that there are at least 10 nodes per wavelength at $f = 1000$ Hz. The total number of meshes is $5^3 = 125$ which is the number of parameter combinations (r_1, r_2, r_3).

The noise and antinoise sources are presented in Fig. 3. The noise source is modelled by a uniformly vibrating surface behind the leg room, which is a simplification of the real noise source. The antinoise sources are labeled as follows. Antinoise panels on the roof are labeled as Axx, where xx is 00, 01, 10, and 11. Point actuators are labeled as AxDOOR, AxBACK, APx2, APx5, APx7, APx9, APx12, APx14, where x is here L for the left side sources and R is for the right side sources. Actuators AxDOOR are located on front doors and actuators APxxx are located on front side window frames, see Fig. 3. On inner surfaces, the absorbing boundary condition in Eq. (2) is posed with the absorbency coefficient $\eta = 0.2$. The study was done in the frequency range 50–1000 Hz with 25 Hz steps.

5.2 Actuator quality evaluation

It is possible to enhance the noise control by choosing good locations for antinoise actuators and by increasing their number. However, increasing the number of actuators also increases the costs and complexity of the noise control system. Thus, it is worthwhile to remove the actuators that have only minor contribution to the noise reduction of the ANC system. The graphs in Figs 4–6 study the quality of noise control and evaluate how each actuator contribute to the noise control quality.

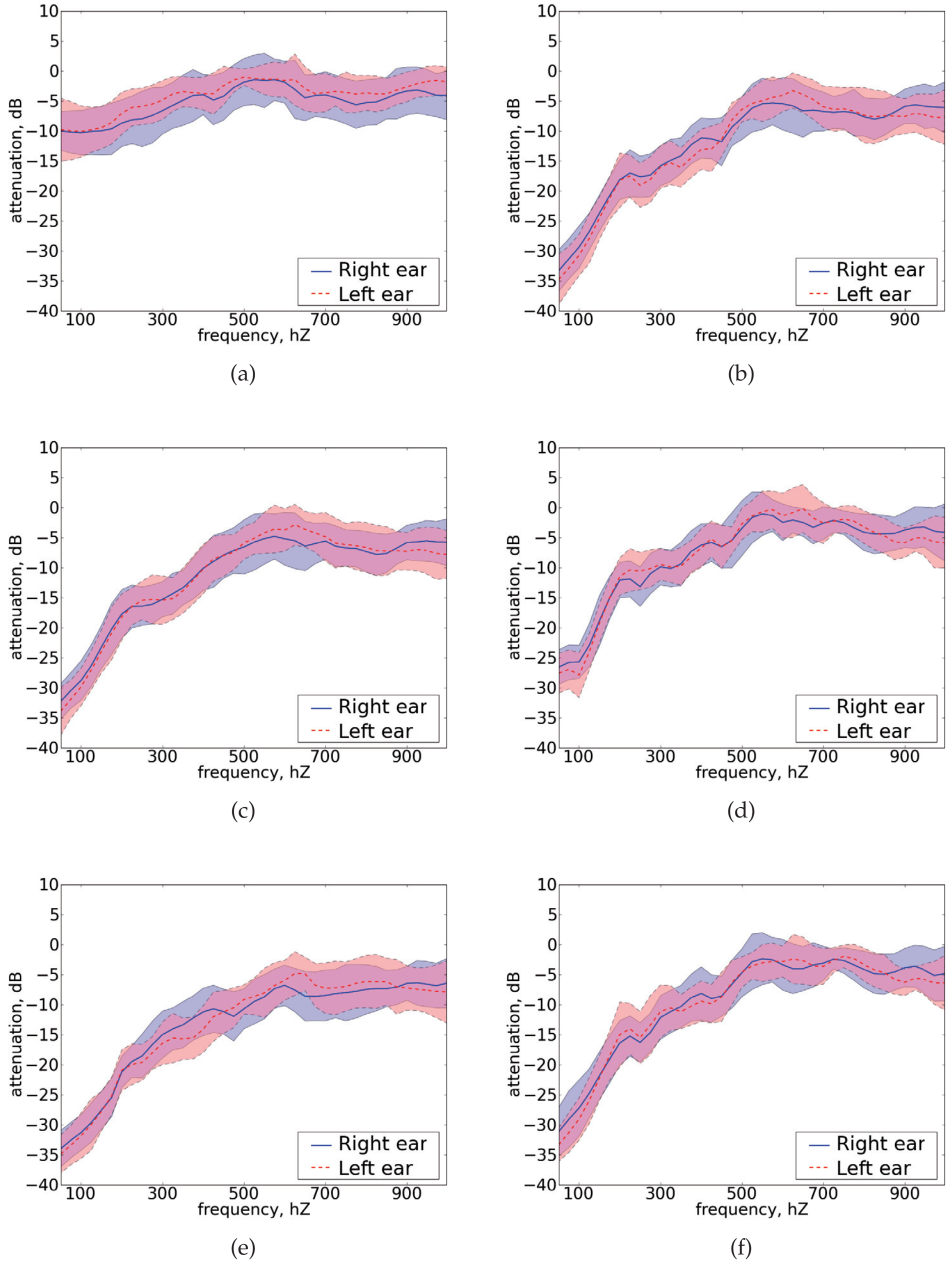

Figure 4: The expectation value of attenuation in left and right ear with standard deviation σ (shaded region). The antinoise actuators are used as follows: (a) Axx, (b) AxDOOR, AxBACK, Axx, (c) AxDOOR, Axx, (d) AxDOOR, (e) AxDOOR, APx2, APx5, APx7, APx9, APx12, APx14, (f) AxDOOR, AxBACK.

In Fig. 4, the expectation value of the noise attenuation and its weighted standard deviation have been plotted at each driver's ear with different actuator combinations. By using two door loudspeakers (AxDOOR) as antinoise actuators, a satisfactory noise control is obtained within the engine noise frequency range, below 500 Hz, as Fig. 4 d shows. By this choice, however, the noise reduction result is not good at higher frequencies, although the expectation value of the attenuation stays negative, i.e. noise is reduced. In Fig. 4 e, 12 additional point antinoise actuators have been placed on side window frames. By these additional actuators, a good attenuation of ca. 10 dB is obtained over the whole studied frequency range.

In Figs 4 a and c, it can be seen that by using only planar actuators on the roof (Axx), the attenuation at low frequencies is not good, but at higher frequencies (700–900 Hz) it is reasonable. When comparing Figs 4 c and d, it is clear that the planar roof actuator (Axx) together with the side door actuators (AxDOOR) is significantly better than the side door actuators (AxDOOR) alone. The attenuation profile is more flat, and even at high frequencies (600–1000 Hz) more than 5 dB expected attenuation is obtained.

If the antinoise itself is very loud, it may cause high sound pressure levels in some parts of the car cabin. By good placement, the amplitude of each actuator can be kept comfortable. In Fig. 5, the amplitude of each antinoise actuator is plotted to evaluate the actuator selections. Fig. 5 a shows that the amplitude of planar roof loudspeakers (Axx) is over 10 dB louder than the amplitude of front door loudspeakers (AxDOOR), especially at high frequencies. In Fig. 5 b, it is seen that the amplitude of back window loudspeakers (AxBACK) is significantly lower than the amplitude of front door loudspeakers (AxDOOR). However, when comparing Figs 4 d and f, it is seen that the contribution of back window loudspeakers (AxBACK) is insignificant for the noise control.

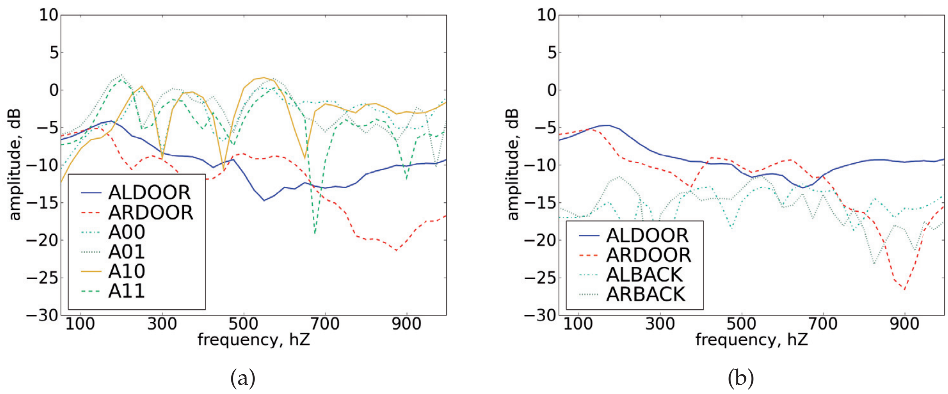

Figure 5: The amplitude of antinoise actuators is plotted in dB with the unit value $|\gamma_i| = 1$ being 0 dB. The antinoise actuators are used as follows: (a) AxDOOR, Axx, (b) AxDOOR, AxBACK.

In Fig. 6, the contribution of each actuator to the noise control is plotted in the following way. The noise levels are compared in both ears when the chosen actuator is enabled and when it is disabled, i.e. $\gamma_i = 0$. For each examined frequency, the worst attenuation result is selected from left or right ear. From Fig. 6, the benefit of each actuator can be evaluated. As already has been suggested, it is seen from Fig. 6 d that the contribution of back window actuators (AxBACK) is less significant than of other actuators, and at high frequencies it is negligible.

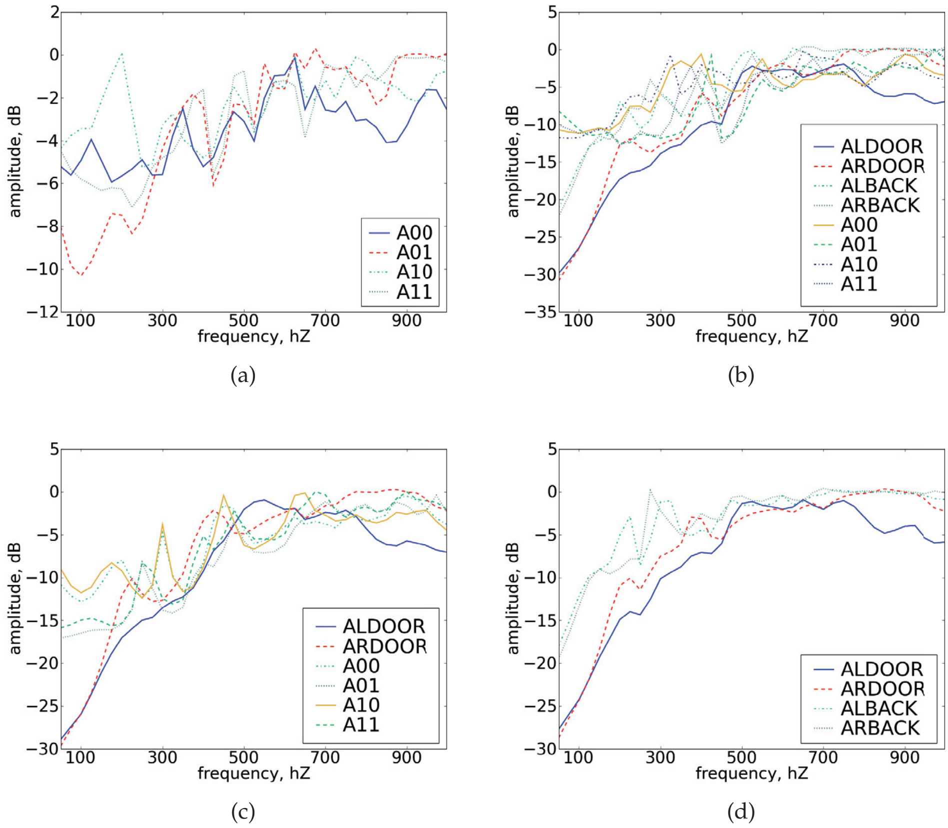

Figure 6: The contribution of each actuator to the noise control system. The noise level is compared between the case when the inspected actuator is enabled and when it is disabled, i.e. $\gamma_i = 0$. For each examined frequency, the worst attenuation is selected from left or right ear and it is plotted in the graph in dB. The antinoise actuators are used as follows: (a) Axx, (b) AxDOOR, AxBACK, Axx, (c) AxDOOR, Axx, (d) AxDOOR, AxBACK.

5.3 Error due to inaccurate actuator signals

The quality of noise control may suffer from inaccurate actuator signals. Such errors can be reduced by calibration. Figs 7 and 8 show attenuation results when there are small inaccuracies in the amplitude and phase of the actuator signals. The antinoise signals are first optimized for a specific noise. In the plotted attenuation graphs, the original noise amplitude is modified by scaling it and keeping the actuator signals unchanged, thus generating some error. By comparing Fig. 4 d to Fig. 7 a, it is noticed that a measurement error of +0.2 dB causes more than 10 dB deterioration at lowest frequencies. On higher frequencies, the influence of error reduces and at 1000 Hz error is insignificant. When the amplitude error is +0.4 dB, the attenuation at lowest frequency deteriorates 3 dB more.

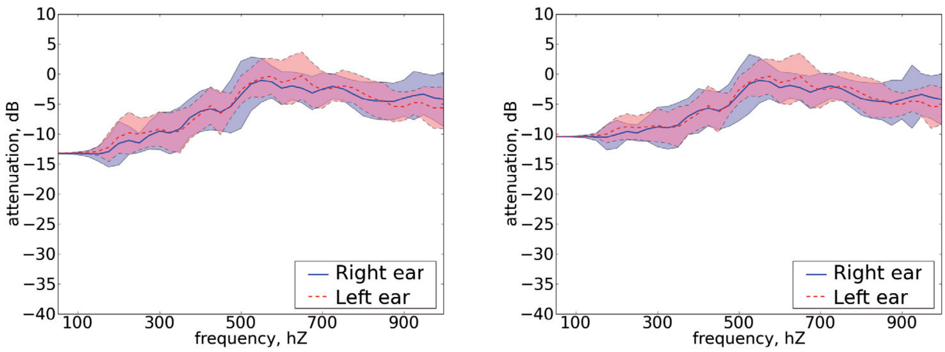

Figure 7: The influence of amplitude error in the actuator signals to the noise reduction. Actuator signals are first optimized for a specific noise. In the attenuation graphs, the original noise amplitude is modified by scaling it and keeping the actuator signals unchanged, thus generating some error. Two antinoise actuators (Ax-DOOR) are used. In the left plot, there is +0.2 dB error and in the right plot there is +0.4 dB error in the amplitude.

The phase error is caused by latency of the noise control device and it can be decreased by calibration and realtime computations. The study in Fig. 8 was carried out as follows. The antinoise was first optimized for a specific noise. In the attenuation graph, the phase of original noise was shifted and the antinoise was kept unchanged. In Fig. 8, there are attenuations with phase errors caused by latencies of 0.75 ms, 1.0 ms, 2.5 ms, and 5 ms. At low frequencies, the influence of phase error is smaller than at high frequencies. Below 500 Hz, the influence of phase error is rather small, if the latency is below 2.5 ms. With 5 ms latency, the noise control attenuation deteriorates significantly, especially at frequencies higher than 500 Hz.

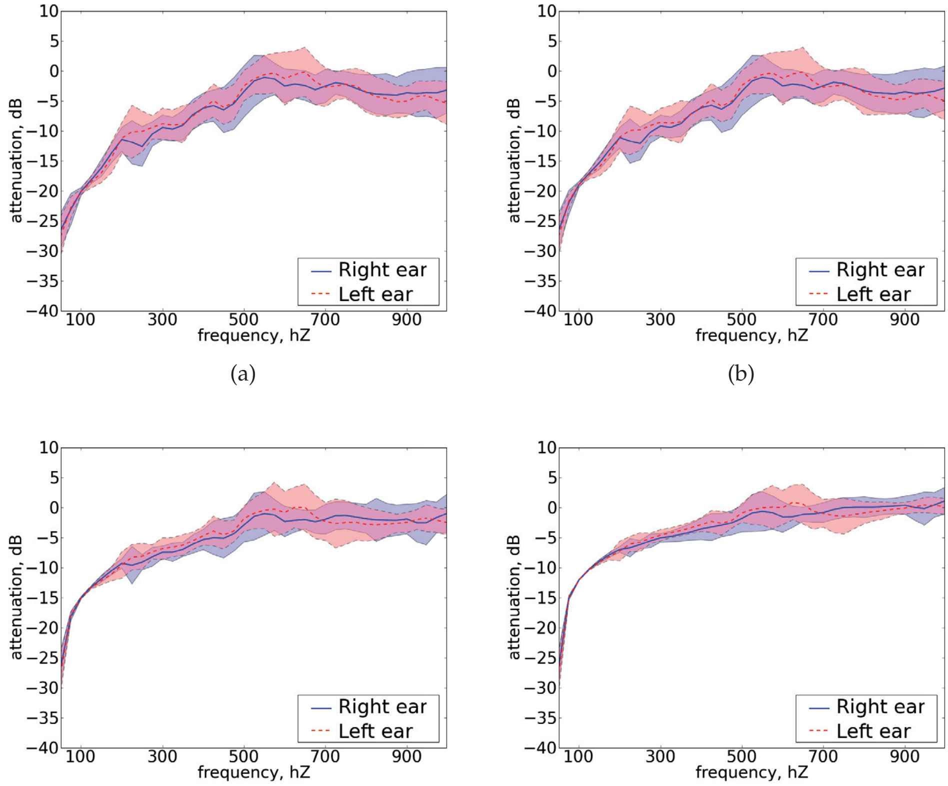

(a) (b) (c) (d)

Figure 8: The phase error influence to the quality of noise control. The antinoise was optimized for a specific noise. In the attenuation graph, the phase of original noise was shifted and the antinoise was kept unchanged. Two antinoise actuators (AxDOOR) are used. The phase error in each figure is as follows: (a) 0.75 ms, (b) 1.0 ms, (c) 2.5 ms, (d) 5 ms.

5.4 Attenuation plots

In Fig. 9, there are example plots of the attenuation when the driver is at different postures. The two front door loudspeakers (AxDOOR), the back window (AxBACK) and the planar roof (Axx) loudspeakers are used as the antinoise actuators. When the frequency is less than 400 Hz, there is more than 10 dB attenuation in almost every posture. The ANC method covers very extensively the lowest frequencies. At frequencies higher than 400 Hz, there is mostly significant, over 5 dB attenuation, but there are also occasional postures that lead to noise amplification, i.e. additive interference of sounds. However, strong noise peaks are unlikely and on average the noise is reduced significantly.

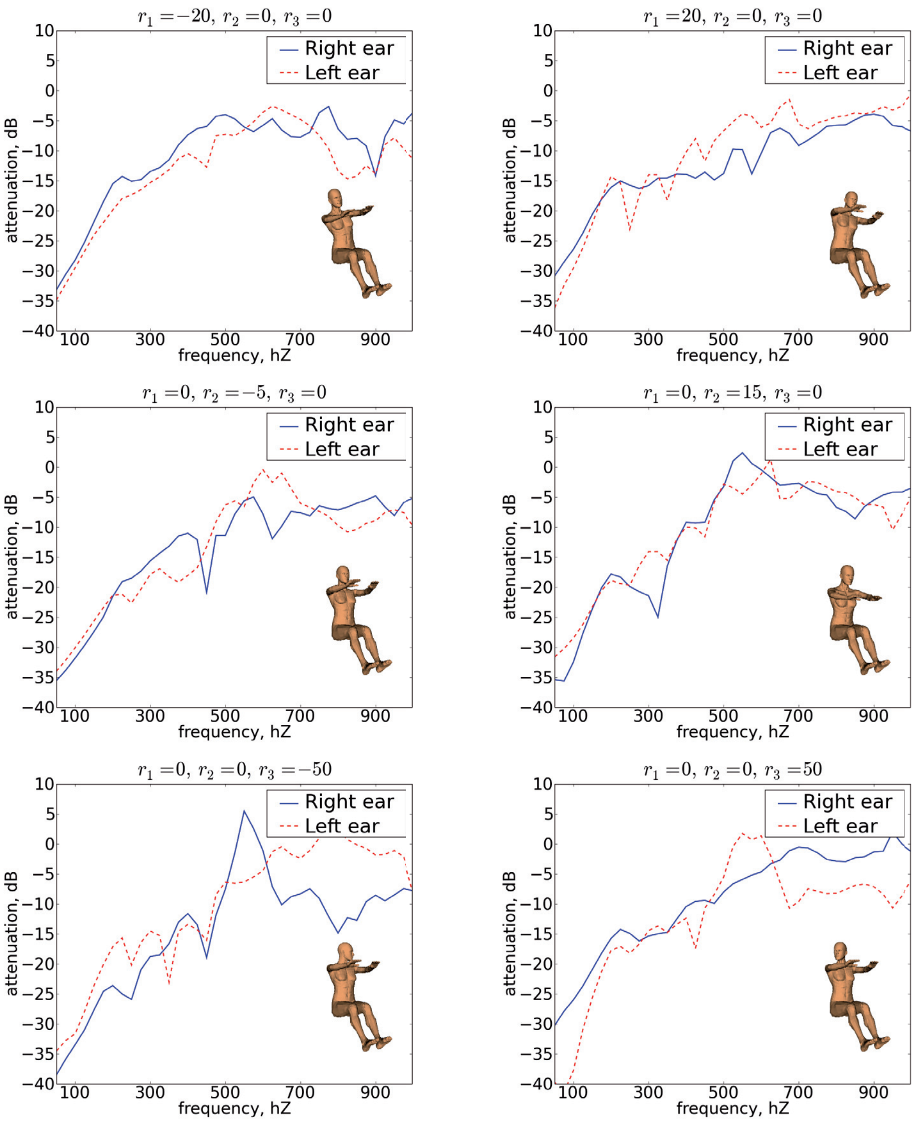

Figure 9: Examples of attenuation graphs at different postures as a function of frequency. The front door (AxDOOR), the back window (AxBACK), and the planar roof (Axx) antinoise actuators are used in the noise control.

Fig. 10 demonstrates the effect of active noise control with two actuators (AxDOOR) at single frequency $f = 300\,\mathrm{Hz}$. It is seen that the method reduces noise effectively near the ears and also in a wider region around the ears. At higher frequencies, the silent area is smaller and the noise is increased in other parts of the car.

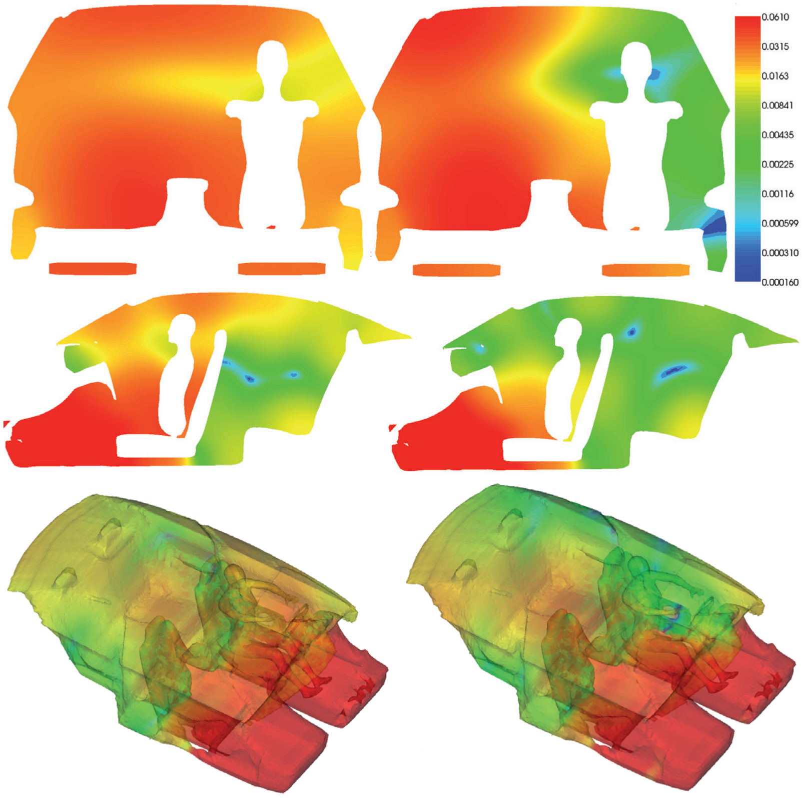

Figure 10: The noise control at frequency $f = 300\,\mathrm{Hz}$ for the basic driver's parameters $r_1 = r_2 = r_3 = 0$. The modulus of pressure amplitude $|p|$ is plotted on the logarithmic color scale. On left plots, the acoustic field is depicted without noise control. On right plots, the noise control is enabled. The attenuation at both ears in this case is ca. $-30\,\mathrm{dB}$. The front door (AxDOOR) loudspeakers are used in the noise control.

6 Conclusions

A method to determine the optimal antinoise for local active noise control (ANC) of sound have been presented by using finite element acoustic modeling. The optimization of antinoise is performed by minimizing the expectation value of the noise in a stochastic domain. The noise is assumed to be decomposed into time harmonic components and therefore the time harmonic wave equation, the Helmholtz partial differential equation, is used to model the sound propagation.

ANC in a car interior is considered as an example and numerical results are studied. The pressure amplitude is solved separately with 25 Hz steps on the frequency range 50–1000 Hz and the solutions are used to optimize the amplitude and phase of the antinoise.

The noise control is studied by considering the expectation value of attenuation as a function of frequency. The method gives good results for low frequency noise already with a few antinoise actuators: by using two front door loudspeakers as antinoise actuators, over 10 dB attenuation is obtained at frequencies below 300 Hz, over 5 dB attenuation is obtained at frequencies between 300–500 Hz, and at 500–1000 Hz, some attenuation still occurs. The results at higher frequencies are significantly better if more actuators are used: with 14 antinoise actuators there is about 10 dB attenuation even at highest studied frequencies (1000 Hz).

The minimization of expectation value in a stochastic domain is an effective approach in active noise control. In the example problem, very good attenuation is obtained for probable postures. In addition, the occurrence of uncomfortable noise peaks is unlikely at usual postures. At higher frequencies, the silent area is smaller and additive interference (noise peaks) also occur.

References

[1] L. L. Beranek, I. L. Ver, Noise and Vibration Control Engineering. Principles and Applications, John Wiley, New York, 1992.

[2] P. A. Nelson, S. J. Elliot, Active Control of Sound, Academic Press, London, 1999.

[3] S. M. Kuo, D. R. Morgan, Active noise control: A tutorial review, Proceedings of the IEEE 87 (6) (1999) 943–973.

[4] J. M. Egana, J. Diaz, J. Vinolas, Active control of low-frequency broadband air-conditioning duct noise, Noise Control Engineering Journal 51 (5) (2003) 292–299.

[5] H. J. Lee, Y. C. Park, C. Lee, D. H. Youn, Fast active noise control algorithm for car exhaust noise control, Electronics Letters 36 (14) (2000) 1250–1251.

[6] P. Shorter, Recent advances in automotive interior noise prediction, SAE BRASIL Noise and Vibration Conference (2008).

[7] D. A. Stanef, C. H. Hansen, R. C. Morgans, Active control analysis of mining vehicle cabin noise using finite element modelling, J. Sound Vib. 277 (1-2) (2004) 277–297.

[8] A. Bermudez, P. Gamallo, R. Rodriguez, Finite element methods in local active control of sound, SIAM J. Control Optim. 43 (2) (2004) 437–465.

[9] C. H. T. Tsang Chiang Yang, Effective optimization-based approach for designing active noise control systems in enclosures, Finite Elem. Anal. Des. 15 (4) (1994) 303–316.

[10] L. L. Thompson, A review of finite-element methods for time-harmonic acoustics, J. Acoust. Soc. Am. 119 (3) (2006) 1315–1330.

[11] Y. Saad, M. H. Schultz, GMRES: a generalized minimal residual algorithm for solving nonsymmetric linear systems, SIAM J. Sci. Statist. Comput. 7 (3) (1986) 856–869.

[12] T. Airaksinen, E. Heikkola, A. Pennanen, J. Toivanen, An algebraic multigrid based shifted-Laplacian preconditioner for the Helmholtz equation, J. Comput. Phys. 226 (1) (2007) 1196–1210.

[13] T. Airaksinen, A. Pennanen, J. Toivanen, A damping preconditioner for time-harmonic wave equations in fluid and elastic material, J. Comput. Phys. To appear (2008)

[14] M. Bastioni, S. Re, S. Misra, Ideas and methods for modeling 3d human figures, in: ACM Bangalore, 2008.

V

MULTIOBJECTIVE MUFFLER SHAPE OPTIMIZATION WITH HYBRID ACOUSTICS MODELLING

by

Tuomas Airaksinen, Erkki Heikkola

Reports of the Department of Mathematical Information Technology, Series B.
Scientific Computing, B 6 / 2010, Submitted to a journal

Multiobjective muffler shape optimization with hybrid acoustics modelling

Tuomas Airaksinen* Erkki Heikkola†

Abstract

Shape optimization of a duct system with respect to sound transmission loss is considered. The objective of optimization is to maximize the sound transmission loss at multiple frequency ranges simultaneously by adjusting the shape of a reactive muffler component. The noise reduction problem is formulated as a multiobjective optimization problem. The sound attenuation for each considered frequency is determined by a hybrid method, which requires solving Helmholtz equation numerically by finite element method. The optimization is performed using non-dominated sorting genetic algorithm, NSGA-II, which is a multi-objective genetic algorithm. The hybrid numerical method is flexible with respect to geometric shapes, material parameters and boundary conditions. Its combination with multiobjective optimization provides an efficient method to design muffler components.

1 Introduction

Physical phenomena encompass many forms of wave propagation and thus bring a great interest to understand wave propagation and its interaction with the environment. Acoustical applications reside in many disciplines, and often the goal is to reduce undesired acoustic noise. Sound propagation especially in waveguides is a fundamentally interesting topic. Ventilation ducts are an example of waveguide where noise reduction is of a special interest.

There are several methods to reduce noise in ducts. The noise reduction is achieved by mufflers, that are of either passive or active type. Passive mufflers fall into two categories: dissipative and reactive. Dissipative mufflers employ noise absorbing material and they are best suited for high frequency noise. Reactive mufflers exploit the shape of muffler component to obtain useful wave reflections and they are best suited at low frequencies. Active mufflers, for one, implement noise reduction by creating antinoise of the same amplitude but opposite phase to the original noise,

*Department of Mathematical Information Technology, University of Jyväskylä, PO Box 35 (Agora), FI-40014 University of Jyväskylä, Finland, tuomas.airaksinen@jyu.fi

†Numerola Oy, P.O. Box 126, FI-40101 Jyväskylä, Finland erkki.heikkola@numerola.fi

see for example Egena et al.[1] and Lee et al[2]. They are effective at low frequency noise cancellation.

The study of acoustical sound propagation in ducts is possible by several means. Experimental acoustical study is often not feasible, whereas analytical or numerical methods can often be considered. There is a introduction to one dimensional duct acoustic modeling in Munjal[3]. Four-pole transfer matrix method, that is based on plane wave theory, offers an approximative way to make a one-dimensional model of muffler acoustics. This approach has been used for transmission loss optimization in duct system in Yeh et al[4]. However, the method is limited to simple geometries and boundary conditions.

The finite element method (FEM) is a general approach to solve approximately partial differential equations. By FEM, it is possible to obtain approximate, yet accurate solution of Helmholtz equation with approparaite boundary conditions. It is also possible to consider problems with complex geometry and varying material properties. By using suitable preconditioner, such as one introduced in Airaksinen et al.[5], it is possible to solve effectively large Helmholtz problems.

In this article, the modelling of an acoustic reactive muffler is based on a hybrid numerical method[6]. This method provides realistic modelling of acoustics in a muffler component, which is located between uniform inlet and outlet ducts. In the uniform parts, acoustic solution can be obtained by modal analysis, where individual propagating modes are solved numerically or in special cases, analytically. For example in circular ducts, solution of the Helmholtz equation can be represented in terms of Bessel functions. Finite element method is used to solve the Helmholtz equation in the non-uniform muffler part of the ductwork. Mode matching[7] is used to couple the different solutions in the muffler and inlet/outlet ducts. The generality of finite element method is thus provided to the acoustics simulation and complicated shapes and configurations can be treated accurately.

The objective of optimization here is to maximize the sound transmission loss (STL) of the muffler by utilizing shape optimization at two frequency ranges simultaneously. In book by Haslinger and Mäkinen[8], an introduction to shape optimization has been given. In addition to shape optimization, material parameters, especially absorption of the boundary material could also be optimized by applying the method of this paper.

As an optimization method, a genetic algorithm (GA) is considered, which is a stochastic optimization algorithm that mimics genetic drift and the Darvinian strife for survival. Unlike traditional gradient-based optimizers that need the derivatives and a good starting point, GA has a good opportunity to locate the global optimum in a near optimal manner. In Mäkinen et al. [9], a genetic algorithm approach to multiobjective aircraft wing shape optimization has been proposed. Here, the optimization is made with the non-dominated sorting genetic algorithm, NSGA-II [10], which is an optimizer well suited for multi-objective problems.

The article is organized as follows. In Section 2, the mathematical formulation of the acoustics in the muffler component is given. Hybrid numerical method is described in Section 3. In Section 4, numerical experiments are performed and results are reported. In Section 5, the concluding remarks are given.

2 Mathematical formulation

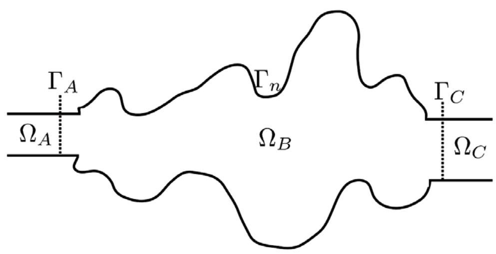

Figure 1: The crosscut illustration of a duct system in a general case: inlet pipe Ω_A, muffler component of arbitrary shape Ω_B and outlet pipe Ω_C.

Sound propagation is governed by the acoustic wave equation

$$c^2 \boldsymbol{\nabla} \cdot \frac{1}{\rho} \boldsymbol{\nabla} \tilde{p} - \frac{1}{\rho} \frac{\partial^2 \tilde{p}}{\partial t^2} \quad = \quad 0, \tag{1}$$

where $\tilde{p}\,(\mathbf{x}, t)$ is the pressure field at location $\mathbf{x}$ and time t, $\rho\,(\mathbf{x})$ is the density of the material, $c\,(\mathbf{x})$ is the speed of sound. Assuming time-harmonic pressure field $\tilde{p}\,(\mathbf{x}, t) = p\,(\mathbf{x})\, e^{-i\omega t}$, where ω is angular frequency and $i = \sqrt{-1}$, Eq. (1) leads to the Helmholtz equation

$$-\boldsymbol{\nabla} \cdot \frac{1}{\rho} \boldsymbol{\nabla} p - \frac{k^2}{\rho} p \quad = \quad 0, \tag{2}$$

where $k = \omega / c$ is the angular wavenumber.

The duct system is illustrated in Fig. 1. It consists of three parts: inlet duct domain Ω_A, muffler component domain Ω_B and outlet duct domain Ω_C. Inlet and outlet ducts must have uniform but arbitrary cross-section. Inlet and outlet ducts are connected to a general, arbitrarily shaped muffler component on interfaces Γ_A and Γ_C. The wall of the muffler is denoted by domain Γ_n, thus $\partial\Omega_B = \Gamma_A \cup \Gamma_n \cup \Gamma_C$. Non-absorbing sound-hard boundary is considered on Γ_n, and it is modelled by Neumann boundary condition

$$\mathbf{n} \cdot \boldsymbol{\nabla} p \quad = \quad 0 \quad \text{on } \Gamma_n, \tag{3}$$

where $\mathbf{n}$ is the outer normal vector on boundary Γ_n.

The solution of Helmholtz equation Eq. (2) in muffler component domain Ω_B is obtained by finite element method, which is described later in Section 3. In duct domains Ω_A and Ω_C, Helmholtz solution can be obtained by modal analysis. In certain special cases such as circular or rectangular duct, analytical form of the solution can be derived, whereas in general shaped duct, eigenfunctions have to be solved numerically. The expansion of the acoustic pressure in duct domains Ω_A and Ω_C is represented in cylindrical coordinates as a sum over the eigenmodes

$$\begin{aligned} p_A(r,\theta,z) &= \sum_{j=0}^{m_A} A_j \Phi_j(r,\theta) e^{-i\lambda_j z} + \sum_{j=0}^{m_A} F_j \Phi_j(r,\theta) e^{i\lambda_j z} \qquad \text{and} \\ p_C(r,\theta,z) &= \sum_{j=0}^{m_C} B_j \Psi_j(r,\theta) e^{-i\gamma_j z} + \sum_{j=0}^{m_C} C_j \Psi_j(r,\theta) e^{i\gamma_j z}, \end{aligned} \tag{4}$$

where $\Phi_j(r,\theta)$ and $\Psi_j(r,\theta)$ are transverse duct eigenfunctions corresponding to the cross-section of the pipe, F_j, A_j, B_j and C_j are the modal amplitudes corresponding to eigenfunctions Ψ_j, Φ_j, and λ_j, γ_j are axial wavenumbers along z-axis. As the evanescent modes can be truncated, sums in Eq. (4) have only finite number propagating modes, denoted by m_A, m_C. Coordinate systems in uniform ducts are chosen such that z-coordinate gives the axial direction of the duct with positive direction away from the nonuniform domain Ω_B. The origin of coordinate system in domain Ω_A is located on the interface Γ_A, and the origin of Ω_C is located on Γ_C.

Coefficients F_j determine the incoming sound from inlet pipe. The equal modal energy density (EMED) assumption, i.e. $|F_n|^2 I_n = |F_m|^2 I_m$ for all m, n, has been chosen for the inlet as incident sound source, as it is a good representation of the sound field emanating from a fan in a ventilation system; see Kirby and Lawrie[11]. For EMED, the incoming modal amplitudes can be calculated from the formula

$$|F_n|^2 = \frac{I_0}{I_n \sum_{m=0}^{n_F} \lambda_m}. \tag{5}$$

Modal amplitude coefficients A_j correspond to the sound that is reflected back from the muffler, B_j correspond to the sound propagating to the outlet pipe and C_j correspond to the sound that is reflected back from outlet pipe. By setting $C_j = 0$ for all j, a perfectly non-reflecting boundary is imposed on Γ_C.

The sound transmission loss function is defined as the ratio of the transmitted to incident sound powers

$$TL(\mathbf{x}, f) = -10 \log_{10} \frac{\rho_A \sum_{m=0}^{n_B} \gamma_m H_m |B_m|^2}{\rho_C \sum_{m=0}^{n_B} \lambda_m I_m |F_m|^2}, \tag{6}$$

where $I_n = \int_{\Gamma_A} |\Phi_n|^2 \, dx$ and $H_m = \int_{\Gamma_B} |\Psi_m|^2 \, dx$. By considering the EMED assumption Eq. (5), we can write the ratio the transmission loss in a simpler form

$$TL(\mathbf{x}, f) = -10 \log_{10} \frac{\rho_A \sum_{m=0}^{n_B} \gamma_m H_m |B_m|^2}{\rho_C I_0}. \tag{7}$$

Next, function $\tau(\mathbf{x}, f)$ is defined as

$$\tau(\mathbf{x}, f) = \min\left(TL(\mathbf{x}, f), TL_{max}\right). \tag{8}$$

Here, parameter TL_{max} is a limiting value for transmission loss, which is necessary due to possible narrow infinite peaks in transmission loss function that inhibit good convergence of the optimizer.

The multiobjective optimization problem is defined as a minimization of objective functions

$$f_1(\mathbf{x}) = -\frac{1}{n_1}\sum_{i=1}^{n_\omega}\tau(\mathbf{x},\omega_i) \qquad \text{and} \qquad f_2(\mathbf{x}) = -\frac{1}{n_2}\sum_{i=1}^{n_\iota}\tau(\mathbf{x},\iota_i), \tag{9}$$

where the shape vector $\mathbf{x} = [x_1, \ldots, x_{n_{vars}}]$ contains parameters that are used to alter the shape of the muffler component, $\boldsymbol{\omega} = [\omega_1, \ldots, \omega_{n_\omega}]$ and $\boldsymbol{\iota} = [\iota_1, \ldots, \iota_{n_\iota}]$ are vectors of frequencies where sound transmission loss is maximized.

2.1 Eigenfunctions in a circular duct

In circular duct, the eigenfunctions $\Phi_j(r,\theta)$ and $\Psi_j(r,\theta)$ are represented by modes

$$\Phi_j(r,\theta) = J_{m_j}(k_{rj}r)\, e^{im_j\theta}, \tag{10}$$

where $J_{m_j}(x)$ is order m_j Bessel function of the first kind and k_{rj} is the radial wavenumber. The radial wavenumber k_{rj} is obtained by considering sound-hard wall boundary condition $\mathbf{n}\cdot\boldsymbol{\nabla}p = 0$, which here implicates that at $r = a$, where a is the radius of the duct wall,

$$J'_{m_j}(k_{rj}a) = 0. \tag{11}$$

Axial wavenumber k_{zj} is evaluated from the effective wavenumber k and the radial wavenumber k_{rj} by

$$k_{zj} = \sqrt{k^2 - k_{rj}^2}. \tag{12}$$

The axial wave propagation is determined by term $e^{ik_{zj}z}$ (see Eq. (4)), which implicates that imaginary axial wavenumber k_{zj} leads to exponential decaying of the wave mode. Thus, the evanescent modes with $k_{rj} > k$ are neglected. Modes are denoted by index j that starts from zero and is ordered according to the radial wavenumbers k_{rj}. The radial wavenumbers are calculated from Bessel derivative roots $k_{rj} = b_j/a$ according to Eq. (11) (see Table 1), where b_j is the root of Bessel derivate of order m_j and a is the radius of the duct.

Table 1: First roots of Bessel derivative function, $J'_{m_j}(b_j) = 0$.

j	1	2	3	4	5
m_j	0	1	2	0	3
b_j	0.0	1.84	3.05	3.83	4.20

3 Hybrid numerical method with mode matching

In the hybrid numerical method, the modal representations in Ω_A and Ω_C are coupled to the finite element representation in Ω_B by mode matching. The weak formulation of the Helmholtz equation Eq. (2) is the following: find $p_B = p_r + p_i i$, where $p_r \in H^1(\Omega_B)$, $p_i \in H^1(\Omega_B)$, such that

$$\int_{\Omega_B} \frac{1}{\rho} \left(\boldsymbol{\nabla} p_B \cdot \boldsymbol{\nabla} v - k^2 p_B v \right) dx - \int_{\partial\Omega_B} \frac{1}{\rho} \mathbf{n} \cdot \boldsymbol{\nabla} p_B \, v \, dx = 0 \tag{13}$$

for any $v \in H^1(\Omega_B)$; $\mathbf{n}$ is outward normal vector. Solution p_A and p_C are coupled to p_B by the boundary conditions

$$\begin{aligned}
\mathbf{n} \cdot \nabla p_B &= \mathbf{n} \cdot \nabla p_A && \text{on } \Gamma_A, && (14)\\
\mathbf{n} \cdot \nabla p_B &= \mathbf{n} \cdot \nabla p_C && \text{on } \Gamma_C, && (15)\\
p_B &= p_A && \text{on } \Gamma_A, && (16)\\
p_B &= p_C && \text{on } \Gamma_C. && (17)
\end{aligned}$$

The first two conditions Eqs. (14) and (15) and Neumann condition Eq. (3) can be incorporated in the weak form Eq. (13), leading to the equation

$$\int_{\Omega_B} \frac{1}{\rho} \left(\boldsymbol{\nabla} p_B \cdot \boldsymbol{\nabla} v - k^2 p_B v \right) dx - \int_{\Gamma_A} \frac{1}{\rho} \mathbf{n} \cdot \boldsymbol{\nabla} p_A \, v \, dx - \int_{\Gamma_C} \frac{1}{\rho} \mathbf{n} \cdot \boldsymbol{\nabla} p_C \, v \, dx = 0. \tag{18}$$

In mode matching, the two other conditions Eqs. (16) and (17) are imposed in weak forms: find $p_A \in Z_A$, $p_B = p_r + p_i i$, where $p_r \in H^1(\Omega_B)$, $p_i \in H^1(\Omega_B)$ and $p_C \in Z_C$ such that

$$\begin{aligned}
\int_{\Gamma_A} (p_B - p_A) \, \bar{\Phi}_i dx &= 0 \text{ and}\\
\int_{\Gamma_C} (p_B - p_C) \, \bar{\Psi}_i dx &= 0
\end{aligned} \tag{19}$$

for any $\bar{\Phi}_i \in Z_A$ and $\bar{\Psi}_i \in Z_C$, where test function spaces are defined as $Z_A = \text{span}_{j=0,\ldots,m_A} \{\Phi_j(r,\theta)\}$ and $Z_C = \text{span}_{j=0,\ldots,m_C} \{\Psi_j(r,\theta)\}$. In summary, the hybrid formulation of the acoustic problem in the waveguide is given by the Eqs. (18) and (19).

Finite element discretization proceeds by approximating the acoustic pressure in Ω_B by

$$p_B(x) = \sum_{j=1}^{n} N_j(x) \, p_j = [N_1(x), \ldots, N_n(x)] \begin{bmatrix} p_1 \\ \vdots \\ p_n \end{bmatrix} = \mathbf{N}(x)^T \mathbf{p}, \tag{20}$$

where $N_j(x)$ are global trial functions for finite element mesh, p_j are the nodal values of the acoustic pressure at node j and n is the number of nodes in Ω_B. Galerkin method of weighted residuals proposes that $N_j(x)$ are used as test functions v. The approximation Eq. (20) is next replaced in Eq. (18) to form a matrix equation

$$\int_{\Omega_B} \frac{1}{\rho}\left(\boldsymbol{\nabla}\mathbf{N}\cdot\boldsymbol{\nabla}\mathbf{N}^T - k^2\mathbf{N}\mathbf{N}^T\right)dx\,\mathbf{p} - \int_{\Gamma_A}\frac{1}{\rho}\mathbf{N}\,\mathbf{n}\cdot\boldsymbol{\nabla}p_A\,dx - \int_{\Gamma_C}\frac{1}{\rho}\mathbf{N}\,\mathbf{n}\cdot\boldsymbol{\nabla}p_C\,dx = 0 \quad (21)$$

The modal representations of the solutions p_A and p_C in Eq. (4) are replaced into Eq. (21), where the normal derivatives of p_A and p_C are of the form

$$\begin{aligned}
\mathbf{n}\cdot\boldsymbol{\nabla}p_A(r,\theta,0) = \frac{\partial}{\partial z}p_A(r,\theta,0) &= -i\sum_{j=0}^{m_A}\lambda_j A_j\Phi_j + i\sum_{j=0}^{m_A}\lambda_j F_j\Phi_j,\\
\mathbf{n}\cdot\boldsymbol{\nabla}p_C(r,\theta,0) = \frac{\partial}{\partial z}p_C(r,\theta,0) &= -i\sum_{j=0}^{m_C}\gamma_j B_j\Psi_j.
\end{aligned} \quad (22)$$

These derivatives are substituted in Eq. (21):

$$\begin{aligned}
\int_{\Omega_B}\frac{1}{\rho}\left(\boldsymbol{\nabla}\mathbf{N}\cdot\boldsymbol{\nabla}\mathbf{N}^T - k^2\mathbf{N}\mathbf{N}^T\right)dx\,\mathbf{p} - \int_{\Gamma_A}\frac{1}{\rho}\mathbf{N}\left(-i\sum_{j=0}^{m_A}\lambda_j A_j\Phi_j + i\sum_{j=0}^{m_A}\lambda_j F_j\Phi_j\right)dx\\
-\int_{\Gamma_C}\frac{1}{\rho}\mathbf{N}\left(-i\sum_{j=0}^{m_C}\gamma_j B_j\Psi_j\right)dx = 0.
\end{aligned} \quad (23)$$

This is expanded in component form

$$\begin{aligned}
\sum_{j=0}^{n_A}\int_{\Omega_B}\frac{1}{\rho}\left(\boldsymbol{\nabla}N_i\cdot\boldsymbol{\nabla}N_j - k^2N_iN_j\right)dx\,p_j + i\sum_{j=0}^{m_A}\lambda_j\int_{\Gamma_A}\frac{1}{\rho}N_i\Phi_j\,dx\,A_j\\
-i\sum_{j=0}^{m_A}\lambda_j\int_{\Gamma_A}\frac{1}{\rho}N_i\Phi_j\,dx\,F_j + i\sum_{j=0}^{m_C}\gamma_j\int_{\Gamma_C}\frac{1}{\rho}N_i\Psi_j\,dx\,B_j &= 0.
\end{aligned} \quad (24)$$

If we use the matrix notations

$$\begin{aligned}
\hat{H}_{ij} &= i\lambda_j\int_{\Gamma_A}\tfrac{1}{\rho}N_i\Phi_j\,dx & \hat{K}_{ij} &= i\gamma_j\int_{\Gamma_C}\tfrac{1}{\rho}N_i\Psi_j\,dx\\
\tilde{f}_i &= i\sum_{j=0}^{m_A}\lambda_j\int_{\Gamma_A}\tfrac{1}{\rho}N_i\Phi_j\,dx\,F_j & G_{ij} &= \int_{\Omega_B}\tfrac{1}{\rho}\left(\boldsymbol{\nabla}N_i\cdot\boldsymbol{\nabla}N_j - k^2N_iN_j\right)dx,
\end{aligned} \quad (25)$$

we can write (24) in matrix form

$$\hat{\mathbf{H}}\mathbf{a} + \mathbf{G}\mathbf{p} + \hat{\mathbf{K}}\mathbf{b} = \tilde{\mathbf{f}}, \quad (26)$$

where $\mathbf{a}$ contains m_A complex modal amplitudes of interface Γ_A, $\mathbf{b}$ contains m_B complex modal amplitudes of interface Γ_B.

Eqs. (4) and (20) are next replaced in Eq. (19):

$$\begin{aligned}
\int_{\Gamma_A} \bar{\Phi}_i \mathbf{N}^T \, dx \, \mathbf{p} &= \sum_{j=0}^{m_A} \int_{\Gamma_A} \Phi_j \bar{\Phi}_i \, dx \, A_j + \sum_{j=0}^{m_A} \int_{\Gamma_A} \Phi_j \bar{\Phi}_i \, dx \, F_j, \\
\int_{\Gamma_B} \bar{\Psi}_i \mathbf{N}^T \, dx \, \mathbf{p} &= \sum_{j=0}^{m_C} \int_{\Gamma_A} \Psi_j \bar{\Psi}_i \, dx \, B_j.
\end{aligned} \tag{27}$$

Expanded to components, this reads

$$\begin{aligned}
\sum_{j=0}^{n} \int_{\Gamma_A} \bar{\Phi}_i N_j \, dx \, p_j &= \sum_{j=0}^{m_A} \int_{\Gamma_A} \Phi_j \bar{\Phi}_i \, dx \, A_j + \sum_{j=0}^{m_A} \int_{\Gamma_A} \Phi_j \bar{\Phi}_i \, dx \, F_j, \\
\sum_{j=0}^{n} \int_{\Gamma_B} \bar{\Psi}_i N_j \, dx \, p_j &= \sum_{j=0}^{m_C} \int_{\Gamma_A} \Psi_j \bar{\Psi}_i \, dx \, B_j.
\end{aligned} \tag{28}$$

By using matrix notations

$$\begin{aligned}
H_{ij} &= \textstyle\int_{\Gamma_A} \Phi_j \bar{\Phi}_i \, dx & K_{ij} &= \textstyle\int_{\Gamma_C} \Psi_j \bar{\Psi}_i \, dx \\
\tilde{H}_{ij} &= -\textstyle\int_{\Gamma_A} \bar{\Phi}_i N_j \, dx & \tilde{K}_{ij} &= -\textstyle\int_{\Gamma_C} \bar{\Psi}_i N_j \, dx \\
f_i &= -\textstyle\sum_{j=0}^{m_A} \int_{\Gamma_A} \Phi_j \bar{\Phi}_i \, dx \, F_i, & &
\end{aligned} \tag{29}$$

Eq. (28) can be written in matrix form

$$\begin{aligned}
\mathbf{H}\mathbf{a} + \tilde{\mathbf{H}}\mathbf{p} &= \mathbf{f} \\
\mathbf{K}\mathbf{b} + \tilde{\mathbf{K}}\mathbf{p} &= \mathbf{0}.
\end{aligned} \tag{30}$$

Now, the Eqs. (26) and (30) can be written as a single block matrix equation

$$\begin{bmatrix} \mathbf{H} & \tilde{\mathbf{H}} & 0 \\ \hat{\mathbf{H}} & \mathbf{G} & \hat{\mathbf{K}} \\ 0 & \tilde{\mathbf{K}} & \mathbf{K} \end{bmatrix} \begin{bmatrix} \mathbf{a} \\ \mathbf{p} \\ \mathbf{b} \end{bmatrix} = \begin{bmatrix} \mathbf{f} \\ \tilde{\mathbf{f}} \\ 0 \end{bmatrix}. \tag{31}$$

4 Numerical experiments

In this section, the multiobjective minimization of the functions f_1 and f_2 in Eq. (9) is tested in four different cases. In each case, the shape of the muffler is controlled with certain shape parameters $\mathbf{x}$ and the goal is to improve attenuation at given frequencies. The test problem #1 represents a non-symmetric three-dimensional muffler component optimization. The test problem #2 is chosen because similar optimization has been considered in Barbieri and Barbieri [12]. The test problem #3 has been chosen as an example of a problem that has many parameters defining the shape. The last test problem #4 is Helmholtz resonator that has been considered in Selamet et al[13]. It has been chosen as second example that represents non-symmetric three-dimensional geometry.

4.1 Technical details

The non-dominated sorting genetic algorithm[10] (NSGA-II) is used as a generic multi-objective optimizer. It is chosen as an optimizer due to local minima and non-linear nature of the problem. The following parameters are used in genetic algorithm. The population size $n_{pop} = 50$ is used in examples #1 and #2 and $n_{pop} = 100$ in examples #3 and #4. At the beginning of optimization, a random population of size $10\, n_{pop}$ is generated, and then the best candidates are chosen to initial population. The crossover probability is set to $p_c = 0.9$. The mutation probability is set to $p_m = 1/n_{vars}$, where n_{vars} is the number of optimization variables in the problem. Binary selection is used and simulated binary crossover (SBX) operator and polynomial mutation operator [14] are utilized with distribution indices $\eta_c = 20$, $\eta_m = 10$, respectively.

The three-dimensional tetrahedral meshes for test problems are generated by freely available Netgen mesh generator[15] and the finite element approximation of the pressure field in muffler component is evaluated by a code written in Numerrin language[16], which is a modelling language developed by Numerola Ltd. Quadratic tetrahedral elements are used in order to reduce the error from approximation of rounded surfaces and finite element pollution effect [17]. The shape of the muffler component is altered with respect to chosen variables in order to obtain optimal transmission loss for the muffler component at chosen frequency ranges. The problem is formulated as a multiobjective optimization problem, as described in Section 2. In numerical experiments, meshes are generated such that there are at least ten elements per wave length at the highest considered frequency. The number of elements in test problems are around 2000. The limiting value $TL_{max} = 50$ dB (see Eq. (8)) is used in all examples.

4.2 Test problem #1

The dimensions and a schematic illustration of the muffler component are presented in Fig. 2a. The length of the chamber is $L = 500$ mm. The radius of inlet and outlet ducts are $r = 30$ mm. The problem has three variables that are optimized: the location of inlet duct $x_1 \in [0.1, 0.5]$, the location of outlet duct $x_2 \in [0.25, 0.5]$ and the radius of muffler chamber $x_3 = [0.04, 0.08]$. Transmission loss is optimized in frequency ranges 800-900 Hz and 1700-1800 Hz. Two sets of frequencies are optimized according to the formulation in Eq. (9): $\boldsymbol{\omega} = [800, 825, 850, 875, 900]$ Hz and $\boldsymbol{\iota} = [1700, 1725, 1750, 1775, 1800]$ Hz. The objective function values in initial population are on average $f_1 = -14.6$ dB and $f_2 = -11.7$ dB.

In Fig. 2b, there are four non-dominated fronts (approximations of pareto optimal fronts) that are obtained by NSGA-II algorithm after 100 generations. The different fronts in the figure are obtained by using different random number generator seed numbers. It is seen, that different fronts are mostly converged to the same line. This implicates that the algorithm is behaving robustly. It is also seen that after optimization, the objectives are over 20 dB better than before optimization.

In Fig. 3b, the transmission loss as a function of frequency is plotted for an optimal solution that is chosen from the non-dominated front at point $f_1 = -38.3$ dB , $f_2 = -33.4$ dB which is given by shape parameter vector $\mathbf{x} = [0.16, 0.37, 0.08]$. It is seen that the transmission loss is significantly greater at optimized frequency ranges than elsewhere.

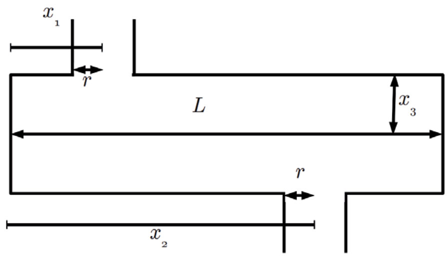

(a)

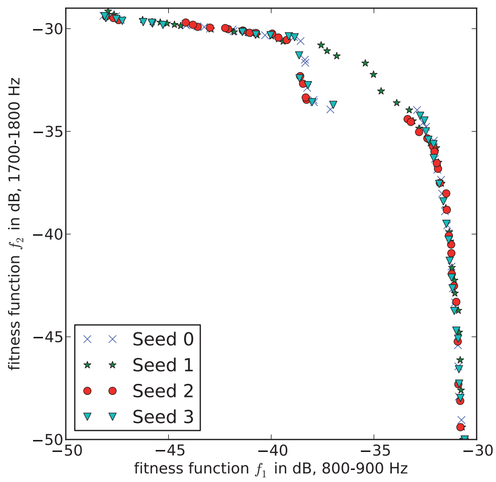

(b)

Figure 2: In the upper figure, there is a diagram of a muffler component cross section used in test case #1. In the lower figure, there are non-dominated solution fronts for test case #1, four different random seeds.

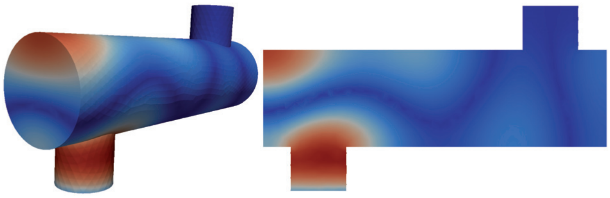

(a)

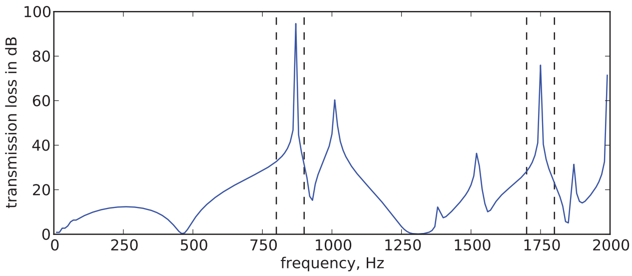

(b)

Figure 3: In the upper figures, there is the time average of pressure for optimal solution of test problem #1. The frequency is $f = 1800$ Hz and optimized parameters are $\mathbf{x} = [0.16, 0.37, 0.08]$ mm. The solution is chosen from non-dominated front at point $f_1 = -38.3$ dB , $f_2 = -33.4$ dB. In the lower figure there is the transmission loss as a function of frequency. Transmission loss is maximized in frequency ranges 800-900 Hz and 1700-1800 Hz.

4.3 Test problem #2

The second numerical example problem is illustrated in Fig. 4a. The geometry of the problem is the same as in Barbieri and Barbieri[12]. The diameter of the chamber is $D = 153.2$ mm and the length of the chamber $L = 282.3$ mm. Inlet and outlet duct diameters are $d = 48.6$ mm. The problem has two variables to be optimized: lengths of the inlet and outlet ducts inside the muffler chamber $x_1, x_2 \in [10, 250]$ mm, respectively.

In Barbieri and Barbieri[12], the tests were reduced to two dimensional domains using axisymmetry, whereas our similations are performed in three-dimensional domains. As an optimizer, the Zoutendijk's feasible direction method was used in Barbieri and Barbieri[12], whereas NSGA-II is considered here. The NSGA-II method brings two obvious advantages: the problem may be formulated as a multi-objective optimization problem and there is no need to choose a good starting point for the algorithm.

Transmission loss is optimized around frequency ranges 600-650 Hz and 1200-1250 Hz. Two sets of frequencies used in Eq. (9) are $\boldsymbol{\omega} = [600, 625, 650]$ Hz and $\boldsymbol{\iota} = [1200, 1225, 1250]$ Hz. The objective function values in initial population are on average $f_1 = f_2 = -10$ dB.

The Fig. 5 shows the non-dominated fronts of objective functions in Eq. (9) given by NSGA-II after 50 generations for the problem when using four different seed number for random number generator. It is seen that fronts have converged to same line and that significant improvement in transmission loss values have been gained at both frequency ranges. It is obvious that the best compromise of the optimal value is found at the edge at point $f_1 = -32.0$ dB, ,$f_2 = -35.4$ dB in Fig. 5. The optimal solution is obtained with parameters $x_1 = 125$ mm and $x_2 = 58$ mm. In Fig. 6, the transmission loss as a function of frequency is plotted. It is seen, that at optimized frequency ranges, there are improvement in transmission loss.

The results obtained in Barbieri and Barbieri[12] (Example 2 in Section 4.2) are very similar to the results obtained here. The optimization method finds a solution where a transmission loss peak in both optimized frequency ranges occur. The method described here is more general and easily used in general three-dimensional problems.

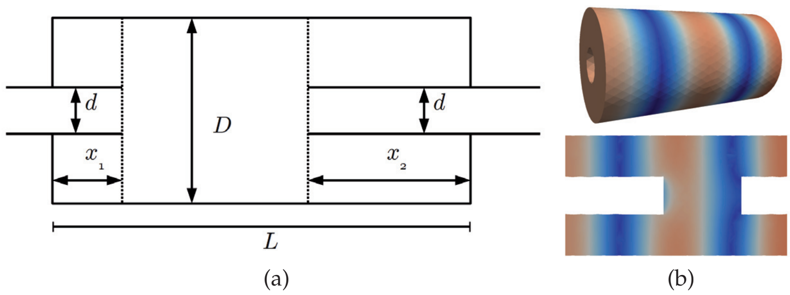

Figure 4: On the left figure, there is the diagram of a muffler component used in test case #2. On the right figure, the time average of pressure for optimal solution is plotted. The frequency is $f = 1225$ Hz and optimized parameters are $x_1 = 125.2$ mm, $x_2 = 58.1$ mm. The solution is chosen from non-dominated front at $f_1 = -32.0$, $f_2 = -35.4$.

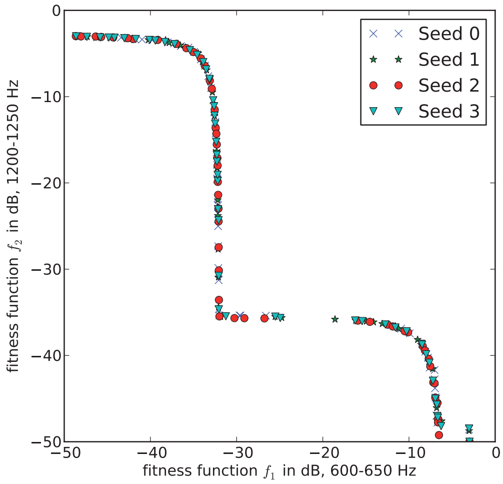

Figure 5: The non-dominated fronts for test case #2, four different random seeds.

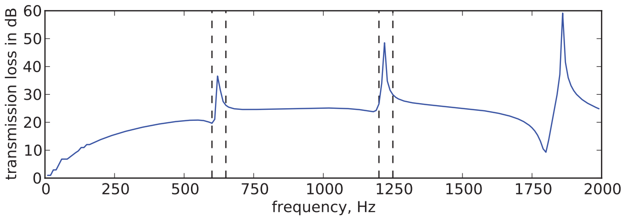

Figure 6: The transmission loss as a function of frequency is plotted. Transmission loss is maximized in frequency ranges 600-650 Hz and 1200-1250 Hz. The optimal parameters $x_1 = 125.2$ mm, $x_2 = 58.1$ mm that are chosen from non-dominated front at $f_1 = -32.0$ dB, $f_2 = -35.4$ dB are used.

4.4 Test problem #3

As an example of a problem that has more optimization variables, a muffler component that consists of five cylinders with variable radii is considered. In Fig. 7a, a schematic figure of the problem is presented. In addition to the radius of each cylinder, the length of inlet and outlet ducts are variable as well, similarly to the test problem #2. The length of muffler component is $L = 1000$ mm and the diameters of inlet and outlet ducts are $d = 100$ mm. The length of inlet and outlet ducts x_1, x_2 can vary between $[20, 900]$ mm and the diameter of each cylinder $x_{3...7}$ is between $[120, 240]$ mm. Transmission loss is optimized in two frequency ranges: between 200-300 Hz and 500-600 Hz, and the frequency sets (see Eq. (9)) are set to $\boldsymbol{\omega} = [200, 233, 266, 300]$ Hz and $\boldsymbol{\iota} = [500, 533, 566, 600]$ Hz. The population size was set to $n_{pop} = 100$ due to larger number of optimization variables.

In Fig. (8), there are four non-dominated fronts of objective functions in Eq. (9) that are obtained by NSGA-II after 120 generations. Also here it is seen that fronts are converged to the same line. Before optimization, the average values of the fitness function values of randomly generated initial population were $f_1 = -13$ dB and $f_2 = -15$ dB.

In Fig. 9, the transmission loss as a function of frequency is plotted for an optimal solution that is chosen from the non-dominated front at $f_1 = -43.16$ dB, $f_2 = -42.97$ dB. The optimal parameters for the chosen solution are x $=$ [35.6, 35.3, 21.0, 24.0, 12.0, 24.0, 14.8] mm. The same parameters are used also when plotting the example solution in Fig. 7b. It is seen in Fig. 9 that both frequency ranges significantly improved transmission loss level.

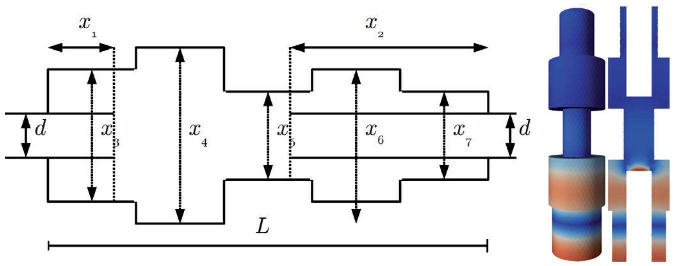

(a) (b)

Figure 7: On the left figure, there is a diagram of a muffler component used in test case #3. On the right figure, the pressure time average of optimal solution is plotted for test case #3 at $f = 600$ Hz. The figure is rotated 90°, such that inlet appears on the bottom of the figure.

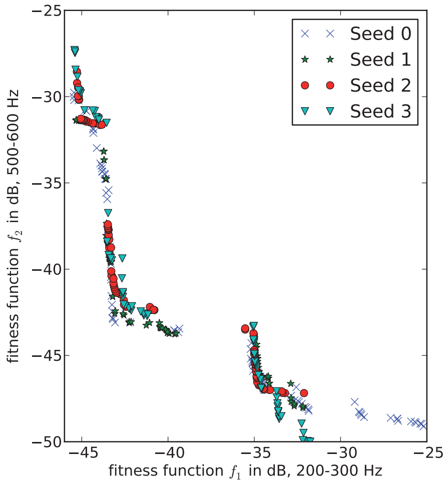

Figure 8: The non-dominated fronts for test case #3 are plotted, four different random seeds.

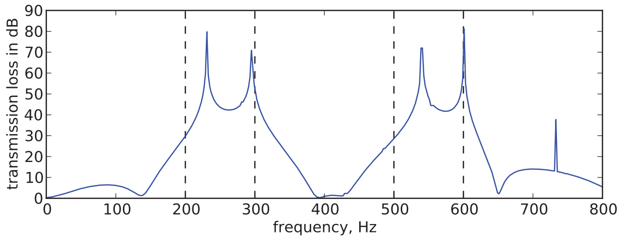

Figure 9: The transmission loss as a function of frequency. Transmission loss is maximized at frequency ranges 200-300 Hz and 500-600 Hz.

4.5 Test problem #4

Fourth example is a Helmholtz resonator component similar to the example used in Selamet et al.[13], that represents an example of true three-dimensional geometry. The dimension of the component are presented in a schematic figure in Fig. 10a. As in Selamet et al.[13], the diameter of the duct is $d_p = 4.859$ cm. The optimization variables are as follows. The diameter of the resonator chamber x_1 can vary between $[1, 15]$ cm, the diameter of connecting pipe x_2 can vary between $[1, 4]$ cm, the length of the connecting duct x_3 can vary between $[0.1, 8.5]$ cm and the length of the resonator chamber x_4 can vary between $[1, 15]$ cm. Transmission loss is optimized in two frequency ranges: between 80-100 Hz and 160-180 Hz, and the frequency sets (see Eq. (9)) are set to $\boldsymbol{\omega} = [160, 170, 180]$ Hz and $\boldsymbol{\iota} = [70, 80, 90]$ Hz. As in previous test problem, the population size is set to $n_{pop} = 100$.

In Fig. 11, there are four non-dominated fronts of objective functions in Eq. (9) that are obtained by NSGA-II after 30 generations. Also here it is seen that fronts are converged to the same line. Before optimization, the average values of the fitness function values of randomly generated initial population were $f_1 = -3.3$ dB and $f_2 = -1.4$ dB.

In Fig. 12, the transmission loss as a function of frequency is plotted for selected optimal solutions. The example solutions for these points are also plotted in Fig. 10b. It is seen in Fig. 12 that in this case, that within the chosen frequency range, it is not possible to obtain significant transmission loss at both frequency ranges simultaneously, as only one peak in transmission loss curve occur. A good solution, however, is obtained for both frequency ranges separately.

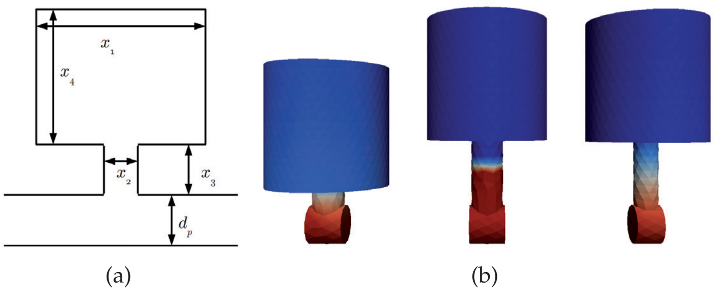

Figure 10: On the left figure, there is a diagram of a Helmholtz resonator component used in test case #4. On the right figure, the pressure time average of selected optimal solutions is plotted for test problem #4. The figures are plotted at 170, 170 and 90 Hz, correspondingly.

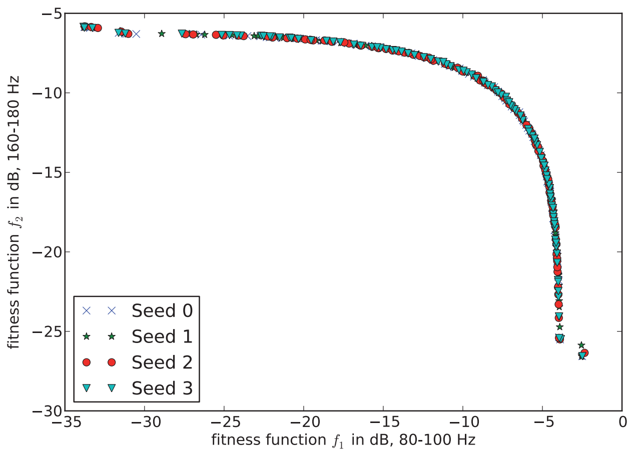

Figure 11: The non-dominated fronts for test case #4 are plotted, four different random seeds.

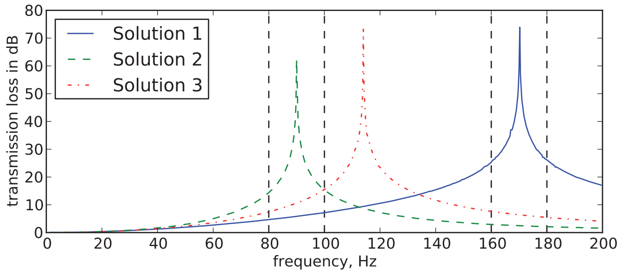

Figure 12: The transmission loss as a function of frequency. Transmission loss is maximized at frequency ranges 80-100 Hz and 160-180 Hz. The solution 1 has been chosen at point $f_1 = -33.8$ dB, $f_2 = -5.9$ dB, solution 2 at $f_1 = -6.5$ dB, $f_2 = -11.2$ dB and solution 3 at $f_1 = -2.5$, $f_2 = -26.6$ dB.

5 Conclusions

Multiobjective shape optimization in a muffler with respect to sound transmission loss has been considered. The shape of the muffler component in a duct system is optimized. NSGA-II has been used as an multiobjective optimization method and acoustics has been simulated by finite element method. A hybrid method has been considered to match the acoustical solution of the muffler with analytical multimodal solution in inlet and outlet ducts.

Two frequency ranges were optimized simultaneously. For each test problem, example solutions were chosen from the non-dominated front that was given by NSGA-II optimizer algorithm. The transmission loss as a function of frequency was plotted for them and the time average of pressure was plotted to a single frequency. A good sound transmission loss, from 30 dB to 50 dB, was obtained at chosen frequencies in each test problem. The optimization significantly improved the objective functions when compared to the initial random designs.

The robustness of the method was tested by considering test problems with four different random number generator seed numbers. It was found that similar results were found for all tested seed numbers, which implicates that the method converges to a near-optimal solution and that the solution does not depend on initial solutions with considered test problems.

Because of the mode matching that was considered on inlet and outlet boundaries, the hybrid method provides accurate and realistic modeling of acoustics in muffler component. The method can be used with any frequency that the computation time and memory allows. Finite element method allows almost arbitrary three-dimensional shape of the design and boundary conditions, which brings versatile possibilities to the formulation of muffler component optimization. Combined with the NSGA-II optimization algorithm, the method offers generic, robust and advanced approach to many three-dimensional muffler optimization problems.

Acknowledgment

Authors want to thank Jari Toivanen for valuable co-operation and comments during the manuscript preparation.

References

[1] J. M. Egana, J. Diaz, J. Vinolas, Active control of low-frequency broadband air-conditioning duct noise, Noise Control Eng. 51 (5) (2003) 292–299.

[2] H. J. Lee, Y. C. Park, C. Lee, D. H. Youn, Fast active noise control algorithm for car exhaust noise control, Electron. Lett. 36 (14) (2000) 1250–1251.

[3] M. L. Munjal, Acoustics of ducts and mufflers, Chichester: John Wiley, 1987.

[4] L.-J. Yeh, Y.-C. Chang, M.-C. Chiu, Shape optimal design on double-chamber mufflers using simulated annealing and a genetic algorithm, Turkish J. Eng. Env. Sci. 29 (2005) 207–224.

[5] T. Airaksinen, A. Pennanen, J. Toivanen, A damping preconditioner for time-harmonic wave equations in fluid and elastic material, J. Comput. Phys. 228 (5) (2009) 1466–1479.

[6] R. Kirby, Modeling sound propagation in acoustic waveguides using a hybrid numerical method, J. Acoust. Soc. Am. 124 (4) (2008) 1930–1940.

[7] R. J. Astley, Fe mode-matching schemes for the exterior helmholtz problem and their relationship to the fe-dtn approach, Commun. Numer. Meth. En. 12 (4) (1996) 257–267.

[8] J. Haslinger, R. A. E. Mäkinen, Introduction to Shape Optimization: Theory, Approximation, and Computation, Society for Industrial and Applied Mathematics, Philadelphia, PA, USA, 2003.

[9] R. A. E. Mäkinen, J. Periaux, J. Toivanen, Multidisciplinary shape optimization in aerodynamics and electromagnetics using genetic algorithms, Int. J. Numer. Meth. Fl. 30 (2) (1999) 149–159.

[10] K. Deb, A. Pratap, S. Agarwal, T. Meyarivan, A Fast Elitist Multi-Objective Genetic Algorithm: NSGA-II, IEEE T. Evolut. Comput. 6 (2000) 182–197.

[11] R. Kirby, J. Lawrie, A point collocation approach to modelling large dissipative silencers, J. Sound Vib. 286 (1-2) (2005) 313–339.

[12] R. Barbieri, N. Barbieri, Finite element acoustic simulation based shape optimization of a muffler, Appl. Acoust. 67 (4) (2006) 346–357.

[13] A. Selamet, P. Radavich, N. Dickey, J. Novak, Circular concentric Helmholtz resonators, J. Acoust. Soc. Am. 101 (1) (1997) 41–51.

[14] R. B. Agrawal, K. Deb, Simulated binary crossover for continuous search space, Complex Syst. 9 (1995) 115–148.

[15] J. Schöberl, NETGEN - an advancing front 2D/3D-mesh generator based on abstract rules, Comput. Visual. Sci 1 (1997) 41–52.

[16] Numerola Ltd, P.O.Box 126 Väinönkatu 7 C, 40101 Jyväskylä, `http://www.numerola.fi`.

[17] F. Ihlenburg, Finite element analysis of acoustic scattering, Vol. 132 of Applied Mathematical Sciences, Springer-Verlag, New York, 1998.

J Y V Ä S K Y L Ä   S T U D I E S   I N   C O M P U T I N G

1 Ropponen, Janne, Software risk management - foundations, principles and empirical findings. 273 p. Yhteenveto 1 p. 1999.
2 Kuzmin, Dmitri, Numerical simulation of reactive bubbly flows. 110 p. Yhteenveto 1 p. 1999.
3 Karsten, Helena, Weaving tapestry: collaborative information technology and organisational change. 266 p. Yhteenveto 3 p. 2000.
4 Koskinen, Jussi, Automated transient hypertext support for software maintenance. 98 p. (250 p.) Yhteenveto 1 p. 2000.
5 Ristaniemi, Tapani, Synchronization and blind signal processing in CDMA systems. - Synkronointi ja sokea signaalinkäsittely CDMA järjestelmässä. 112 p. Yhteenveto 1 p. 2000.
6 Laitinen, Mika, Mathematical modelling of conductive-radiative heat transfer. 20 p. (108 p.) Yhteenveto 1 p. 2000.
7 Koskinen, Minna, Process metamodelling. Conceptual foundations and application. 213 p. Yhteenveto 1 p. 2000.
8 Smolianski, Anton, Numerical modeling of two-fluid interfacial flows. 109 p. Yhteenveto 1 p. 2001.
9 Nahar, Nazmun, Information technology supported technology transfer process. A multi-site case study of high-tech enterprises. 377 p. Yhteenveto 3 p. 2001.
10 Fomin, Vladislav V., The process of standard making. The case of cellular mobile telephony. - Standardin kehittämisen prosessi. Tapaustutkimus solukkoverkkoon perustuvasta matkapuhelintekniikasta. 107 p. (208 p.) Yhteenveto 1 p. 2001.
11 Päivärinta, Tero, A genre-based approach to developing electronic document management in the organization. 190 p. Yhteenveto 1 p. 2001.
12 Häkkinen, Erkki, Design, implementation and evaluation of neural data analysis environment. 229 p. Yhteenveto 1 p. 2001.
13 Hirvonen, Kullervo, Towards better employment using adaptive control of labour costs of an enterprise. 118 p. Yhteenveto 4 p. 2001.
14 Majava, Kirsi, Optimization-based techniques for image restoration. 27 p. (142 p.) Yhteenveto 1 p. 2001.
15 Saarinen, Kari, Near infra-red measurement based control system for thermo-mechanical refiners. 84 p. (186 p.) Yhteenveto 1 p. 2001.
16 Forsell, Marko, Improving component reuse in software development. 169 p. Yhteenveto 1 p. 2002.
17 Virtanen, Pauli, Neuro-fuzzy expert systems in financial and control engineering. 245 p. Yhteenveto 1 p. 2002.
18 Kovalainen, Mikko, Computer mediated organizational memory for process control. Moving CSCW research from an idea to a product. 57 p. (146 p.) Yhteenveto 4 p. 2002.
19 Hämäläinen, Timo, Broadband network quality of service and pricing. 140 p. Yhteenveto 1 p. 2002.
20 Martikainen, Janne, Efficient solvers for discretized elliptic vector-valued problems. 25 p. (109 p.) Yhteenveto 1 p. 2002.
21 Mursu, Anja, Information systems development in developing countries. Risk management and sustainability analysis in Nigerian software companies. 296 p. Yhteenveto 3 p. 2002.
22 Seleznyov, Alexandr, An anomaly intrusion detection system based on intelligent user recognition. 186 p. Yhteenveto 3 p. 2002.
23 Lensu, Anssi, Computationally intelligent methods for qualitative data analysis. 57 p. (180 p.) Yhteenveto 1 p. 2002.
24 Ryabov, Vladimir, Handling imperfect temporal relations. 75 p. (145 p.) Yhteenveto 2 p. 2002.
25 Tsymbal, Alexey, Dynamic integration of data mining methods in knowledge discovery systems. 69 p. (170 p.) Yhteenveto 2 p. 2002.
26 Akimov, Vladimir, Domain decomposition methods for the problems with boundary layers. 30 p. (84 p.). Yhteenveto 1 p. 2002.
27 Seyukova-Rivkind, Ludmila, Mathematical and numerical analysis of boundary value problems for fluid flow. 30 p. (126 p.) Yhteenveto 1 p. 2002.
28 Hämäläinen, Seppo, WCDMA Radio network performance. 235 p. Yhteenveto 2 p. 2003.
29 Pekkola, Samuli, Multiple media in group work. Emphasising individual users in distributed and real-time CSCW systems. 210 p. Yhteenveto 2 p. 2003.
30 Markkula, Jouni, Geographic personal data, its privacy protection and prospects in a location-based service environment. 109 p. Yhteenveto 2 p. 2003.
31 Honkaranta, Anne, From genres to content analysis. Experiences from four case organizations. 90 p. (154 p.) Yhteenveto 1 p. 2003.
32 Raitamäki, Jouni, An approach to linguistic pattern recognition using fuzzy systems. 169 p. Yhteenveto 1 p. 2003.
33 Saalasti, Sami, Neural networks for heart rate time series analysis. 192 p. Yhteenveto 5 p. 2003.
34 Niemelä, Marketta, Visual search in graphical interfaces: a user psychological approach. 61 p. (148 p.) Yhteenveto 1 p. 2003.
35 You, Yu, Situation Awareness on the world wide web. 171 p. Yhteenveto 2 p. 2004.
36 Taatila, Vesa, The concept of organizational competence – A foundational analysis. - Perusteanalyysi organisaation kompetenssin käsitteestä. 111 p. Yhteenveto 2 p. 2004.

37 LYYTIKÄINEN, VIRPI, Contextual and structural metadata in enterprise document management. - Konteksti- ja rakennemetatieto organisaation dokumenttien hallinnassa. 73 p. (143 p.) Yhteenveto 1 p. 2004.
38 KAARIO, KIMMO, Resource allocation and load balancing mechanisms for providing quality of service in the Internet. 171 p. Yhteenveto 1 p. 2004.
39 ZHANG, ZHEYING, Model component reuse. Conceptual foundations and application in the metamodeling-based systems analysis and design environment. 76 p. (214 p.) Yhteenveto 1 p. 2004.
40 HAARALA, MARJO, Large-scale nonsmooth optimization variable metric bundle method with limited memory. 107 p. Yhteenveto 1 p. 2004.
41 KALVINE, VIKTOR, Scattering and point spectra for elliptic systems in domains with cylindrical ends. 82 p. 2004.
42 DEMENTIEVA, MARIA, Regularization in multistage cooperative games. 78 p. 2004.
43 MAARANEN, HEIKKI, On heuristic hybrid methods and structured point sets in global continuous optimization. 42 p. (168 p.) Yhteenveto 1 p. 2004.
44 FROLOV, MAXIM, Reliable control over approximation errors by functional type a posteriori estimates. 39 p. (112 p.) 2004.
45 ZHANG, JIAN, Qos- and revenue-aware resource allocation mechanisms in multiclass IP networks. 85 p. (224 p.) 2004.
46 KUJALA, JANNE, On computation in statistical models with a psychophysical application. 40 p. (104 p.) 2004.,
47 SOLBAKOV, VIATCHESLAV, Application of mathematical modeling for water environment problems. 66 p. (118 p.) 2004.
48 HIRVONEN, ARI P., Enterprise architecture planning in practice. The Perspectives of information and communication technology service provider and end-user. 44 p. (135 p.) Yhteenveto 2 p. 2005.
49 VARTIAINEN, TERO, Moral conflicts in a project course in information systems education. 320 p. Yhteenveto 1p. 2005.
50 HUOTARI, JOUNI, Integrating graphical information system models with visualization techniques. - Graafisten tietojärjestelmäkuvausten integrointi visualisointitekniikoilla. 56 p. (157 p.) Yhteenveto 1p. 2005.
51 WALLENIUS, EERO R., Control and management of multi-access wireless networks. 91 p. (192 p.) Yhteenveto 3 p. 2005.
52 LEPPÄNEN, MAURI, An ontological framework and a methodical skeleton for method engineering – A contextual approach. 702 p. Yhteenveto 2 p. 2005.
53 MATYUKEVICH, SERGEY, The nonstationary Maxwell system in domains with edges and conical points. 131 p. Yhteenveto 1 p. 2005.
54 SAYENKO, ALEXANDER, Adaptive scheduling for the QoS supported networks. 120 p. (217 p.) 2005.
55 KURJENNIEMI, JANNE, A study of TD-CDMA and WCDMA radio network enhancements. 144 p. (230 p.) Yhteenveto 1 p. 2005.
56 PECHENIZKIY, MYKOLA, Feature extraction for supervised learning in knowledge discovery systems. 86 p. (174 p.) Yhteenveto 2 p. 2005.
57 IKONEN, SAMULI, Efficient numerical methods for pricing American options. 43 p. (155 p.) Yhteenveto 1 p. 2005.
58 KÄRKKÄINEN, KARI, Shape sensitivity analysis for numerical solution of free boundary problems. 83 p. (119 p.) Yhteenveto 1 p. 2005.
59 HELFENSTEIN, SACHA, Transfer. Review, reconstruction, and resolution. 114 p. (206 p.) Yhteenveto 2 p. 2005.
60 NEVALA, KALEVI, Content-based design engineering thinking. In the search for approach. 64 p. (126 p.) Yhteenveto 1 p. 2005.
61 KATASONOV, ARTEM, Dependability aspects in the development and provision of location-based services. 157 p. Yhteenveto 1 p. 2006.
62 SARKKINEN, JARMO, Design as discourse: Representation, representational practice, and social practice. 86 p. (189 p.) Yhteenveto 1 p. 2006.
63 ÄYRÄMÖ, SAMI, Knowledge mining using robust clustering. 296 p. Yhteenveto 1 p. 2006.
64 IFINEDO, PRINCELY EMILI, Enterprise resource planning systems success assessment: An integrative framework. 133 p. (366 p.) Yhteenveto 3 p. 2006.
65 VIINIKAINEN, ARI, Quality of service and pricingin future multiple service class networks. 61 p. (196 p.) Yhteenveto 1 p. 2006.
66 WU, RUI, Methods for space-time parameter estimation in DS-CDMA arrays. 73 p. (121 p.) 2006.
67 PARKKOLA, HANNA, Designing ICT for mothers. User psychological approach. – Tieto- ja viestintätekniikoiden suunnittelu äideille. Käyttäjäpsykologinen näkökulma. 77 p. (173 p.) Yhteenveto 3 p. 2006.
68 HAKANEN, JUSSI, On potential of interactive multiobjective optimization in chemical process design. 75 p. (160 p.) Yhteenveto 2 p. 2006.
69 PUTTONEN, JANI, Mobility management in wireless networks. 112 p. (215 p.) Yhteenveto 1 p. 2006.
70 LUOSTARINEN, KARI, Resource , management methods for QoS supported networks. 60 p. (131 p.) 2006.
71 TURCHYN, PAVLO, Adaptive meshes in computer graphics and model-based simulation. 27 p. (79 p.) Yhteenveto 1 p.
72 ZHOVTOBRYUKH, DMYTRO, Context-aware web service composition. 290 p. Yhteenveto 2 p. 2006.

73 KOHVAKKO, NATALIYA, Context modeling and utilization in heterogeneous networks. 154 p. Yhteenveto 1 p. 2006.

74 MAZHELIS, OLEKSIY, Masquerader detection in mobile context based on behaviour and environment monitoring. 74 p. (179 p). Yhteenveto 1 p. 2007.

75 SILTANEN, JARMO, Quality of service and dynamic scheduling for traffic engineering in next generation networks. 88 p. (155 p.) 2007.

76 KUUVA, SARI, Content-based approach to experiencing visual art. - Sisältöperustainen lähestymistapa visuaalisen taiteen kokemiseen. 203 p. Yhteenveto 3 p. 2007.

77 RUOHONEN, TONI, Improving the operation of an emergency department by using a simulation model. 164 p. 2007.

78 NAUMENKO, ANTON, Semantics-based access control in business networks. 72 p. (215 p.) Yhteenveto 1 p. 2007.

79 WAHLSTEDT, ARI, Stakeholders' conceptions of learning in learning management systems development. - Osallistujien käsitykset oppimisesta oppimisympäristöjen kehittämisessä. 83 p. (130 p.) Yhteenveto 1 p. 2007.

80 ALANEN, OLLI, Quality of service for triple play services in heterogeneous networks. 88 p. (180 p.) Yhteenveto 1 p. 2007.

81 NERI, FERRANTE, Fitness diversity adaptation in memetic algorithms. 80 p. (185 p.) Yhteenveto 1 p. 2007.

82 KURHINEN, JANI, Information delivery in mobile peer-to-peer networks. 46 p. (106 p.) Yhteenveto 1 p. 2007.

83 KILPELÄINEN, TURO, Genre and ontology based business information architecture framework (GOBIAF). 74 p. (153 p.) Yhteenveto 1 p. 2007.

84 YEVSEYEVA, IRYNA, Solving classification problems with multicriteria decision aiding approaches. 182 p. Yhteenveto 1 p. 2007.

85 KANNISTO, ISTO, Optimized pricing, QoS and segmentation of managed ICT services. 45 p. (111 p.) Yhteenveto 1 p. 2007.

86 GORSHKOVA, ELENA, A posteriori error estimates and adaptive methods for incompressible viscous flow problems. 72 p. (129 p.) Yhteenveto 1 p. 2007.

87 LEGRAND, STEVE, Use of background real-world knowledge in ontologies for word sense disambiguation in the semantic web. 73 p. (144 p.) Yhteenveto 1 p. 2008.

88 HÄMÄLÄINEN, NIINA, Evaluation and measurement in enterprise and software architecture management. - Arviointi ja mittaaminen kokonais- ja ohjelmistoarkkitehtuurien hallinnassa. 91 p. (175 p.) Yhteenveto 1 p. 2008.

89 OJALA, ARTO, Internationalization of software firms: Finnish small and medium-sized software firms in Japan. 57 p. (180 p.) Yhteenveto 2 p. 2008.

90 LAITILA, ERKKI, Symbolic Analysis and Atomistic Model as a Basis for a Program Comprehension Methodology. 321 p. Yhteenveto 3 p. 2008.

91 NIHTILÄ, TIMO, Performance of Advanced Transmission and Reception Algorithms for High Speed Downlink Packet Access. 93 p. (186 p.) Yhteenveto 1 p. 2008.

92 SETÄMAA-KÄRKKÄINEN, ANNE, Network connection selection-solving a new multiobjective optimization problem. 52 p. (111p.) Yhteenveto 1 p. 2008.

93 PULKKINEN, MIRJA, Enterprise architecture as a collaboration tool. Discursive process for enterprise architecture management, planning and development. 130 p. (215 p.) Yhteenveto 2 p. 2008.

94 PAVLOVA, YULIA, Multistage coalition formation game of a self-enforcing international environmental agreement. 127 p. Yhteenveto 1 p. 2008.

95 NOUSIAINEN, TUULA, Children's involvement in the design of game-based learning environments. 297 p. Yhteenveto 2 p. 2008.

96 KUZNETSOV, NIKOLAY V., Stability and oscillations of dynamical systems. Theory and applications. 116 p. Yhteenveto 1 p. 2008.

97 KHRIYENKO, OLEKSIY, Adaptive semantic Web based environment for web resources. 193 p. Yhteenveto 1 p. 2008.

98 TIRRONEN, VILLE, Global optimization using memetic differential evolution with applications to low level machine vision. 98 p. (248 p.) Yhteenveto 1 p. 2008.

99 VALKONEN, TUOMO, Diff-convex combinations of Euclidean distances: A search for optima. 148 p. Yhteenveto 1 p. 2008.

100 SARAFANOV, OLEG, Asymptotic theory of resonant tunneling in quantum waveguides of variable cross-section. 69 p. Yhteenveto 1 p. 2008.

101 POZHARSKIY, ALEXEY, On the electron and phonon transport in locally periodical waveguides. 81 p. Yhteenveto 1 p. 2008.

102 AITTOKOSKI, TIMO, On challenges of simulation-based globaland multiobjective optimization. 80 p. (204 p.) Yhteenveto 1 p. 2009.

103 YALAHO, ANICET, Managing offshore outsourcing of software development using the ICT-supported unified process model: A cross-case analysis. 91 p. (307 p.) Yhteenveto 4 p. 2009.

104 K OLLANUS, SAMI, Tarkastuskäytänteiden kehittäminen ohjelmistoja tuottavissa organisaatioissa. - Improvement of inspection practices in software organizations. 179 p. Summary 4 p. 2009.

105 LEIKAS, JAANA, Life-Based Design. 'Form of life' as a foundation for ICT design for older adults. - Elämälähtöinen suunnittelu. Elämänmuoto ikääntyville tarkoitettujen ICT tuotteiden ja palvelujen suunnittelun lähtökohtana. 218 p. (318 p.) Yhteenveto 4 p. 2009.

J Y V Ä S K Y L Ä   S T U D I E S   I N   C O M P U T I N G

106 VASILYEVA, EKATERINA, Tailoring of feedback in web-based learning systems: Certitude-based assessment with online multiple choice questions. 124 p. (184 p.) Yhteenveto 2 p. 2009.
107 KUDRYASHOVA, ELENAV., Cycles in continuous and discrete dynamical systems. Computations, computer assisted proofs, and computer experiments. 79 p. (152 p.) Yhteenveto 1 p. 2009.
108 BLACKLEDGE, JONATHAN, Electromagnetic scattering and inverse scattering solutions for the analysis and processing of digital signals and images. 297 p. Yhteenveto 1 p. 2009.
109 IVANNIKOV, ANDRIY, Extraction of event-related potentials from electroencephalography data. - Herätepotentiaalien laskennallinen eristäminen EEG-havaintoaineistosta. 108 p. (150 p.) Yhteenveto 1 p. 2009.
110 KALYAKIN, IGOR, Extraction of mismatch negativity from electroencephalography data. - Poikkeavuusnegatiivisuuden erottaminen EEG-signaalista. 47 p. (156 p.) Yhteenveto 1 p. 2010.
111 HEIKKILÄ, MARIKKA, Coordination of complex operations over organisational boundaries. 265 p. Yhteenveto 3 p. 2010.
112 FEKETE, GÁBOR, Network interface management in mobile and multihomed nodes. 94 p. (175 p.) Yhteenveto 1 p. 2010.
113 KUJALA, TUOMO, Capacity, workload and mental contents - Exploring the foundations of driver distraction. 146 p. (253 p.) Yhteenveto 2 p. 2010.
114 LUGANO, GIUSEPPE, Digital community design - Exploring the role of mobile social software in the process of digital convergence. 253 p. (316 p.) Yhteenveto 4 p. 2010.
115 KAMPYLIS, PANAGIOTIS, Fostering creative thinking. The role of primary teachers. - Luovaa ajattelua kehittämässä. Alakoulun opettajien rooli. 136 p. (268 p.) Yhteenveto 2 p. 2010.
116 TOIVANEN, JUKKA, Shape optimization utilizing consistent sensitivities. - Muodon optimointi käyttäen konsistentteja herkkyyksiä. 55 p. (130p.) Yhteenveto 1 p. 2010.
117 MATTILA, KEIJO, Implementation techniques for the lattice Boltzmann method. - Virtausdynamiikan tietokonesimulaatioita Hila-Boltzmann -menetelmällä: implementointi ja reunaehdot. 177 p. (233 p.) Yhteenveto 1 p. 2010.
118 CONG, FENGYU, Evaluation and extraction of mismatch negativity through exploiting temporal, spectral, time-frequency, and spatial features. - Poikkeavuusnegatiivisuuden (MMN) erottaminen aivosähkönauhoituksista käyttäen ajallisia, spektraalisia, aikataajuus - ja tilapiirteitä. 57 p. (173 p.) Yhteenveto 1 p. 2010.
119 LIU, SHENGHUA, Interacting with intelligent agents. Key issues in agent-based decision support system design. 90 p. (143 p.) Yhteenveto 2 p. 2010.
120 AIRAKSINEN, TUOMAS, Numerical methods for acoustics and noise control. - Laskennallisia menetelmiä akustisiin ongelmiin ja melunvaimennukseen. 58 p. (133 p.) Yhteenveto 2 p. 2010.